Doctoral Dissertation

A study on the interactive phenomena in the hybrid keyhole plasma arc welding-gas metal arc welding process

WU DONGSHENG

January 2021

Graduate School of Engineering
Osaka University

Contents

Chapter 1 Introduction and literature review

1.1 Background

As one of the high energy density welding processes, keyhole plasma arc welding (KPAW) process has the advantages of low equipment cost and joint tolerance compared with laser beam welding (LBW) and electron beam welding (EBW), and thus is widely used in welding of automobile [1], airplane [2], rocket [3], structure steel [4]. During the KPAW process, as the plasma arc with high energy and high momentum impinges on the base metal surface, the metal is melted, and pushed to the edge of the weld pool [5]. A large keyhole is formed during the KPAW process [6], and middle thick steel and aluminum alloy plates [7] can be joined with only one pass.

It should be noted that the keyhole inside the weld pool in the KPAW process is very unstable [8], and the welding parameter window to obtain sound bead is very narrow. Welding defects [9,10], such as undercuts, are easy to form in the KPAW process, which decrease the static, fatigue and fracture strength of the weld joint

In order to suppress weld defects and improve the weld bead formation, paraxial hybrid keyhole plasma arc welding and gas metal arc welding (KPAW-GMAW) process was proposed by many researchers [11,12,13], in which the plasma torch was located at the leading direction, and the GMAW torch was located at the rearing direction. During the hybrid KPAW-GMAW process, a deep keyhole is formed under the plasma arc, and the bead formation can be effectively improved by GMAW. Besides, a direct current path is formed between the KPAW cathode (tungsten electrode) and GMAW anode (welding wire) through the arc plasma [14]. In summary, the hybrid KPAW-GMAW process is characterized by complex interactions of the arc, droplet, keyhole and weld pool. Deep understanding of the interactive phenomena in the hybrid KPAW-GMAW process can help provide guidance to the welding engineers in developing welding procedures to obtain high quality welds.

1.2 Interesting phenomena in keyhole plasma arc welding

1.2.1 High plasma arc temperature while low weld pool temperature

Under the constraint effects of water cooling nozzle, plasma gas and Lorenz force, the plasma arc energy density is increased, as well as the plasma arc temperature [15,16]. As shown in **Fig.1.1**, the maximum arc temperature in the KPAW process with a current

of 120 A is much higher than that in the gas tungsten arc welding (GTAW) process with a same welding current [17].

Based on Nguyen's study [18], the maximum temperature on the top and bottom surfaces of the weld pool in the KPAW process of 304 stainless steel was about 1800 K when the welding current was 120 A, which was similar to that in the moving GTAW process [19], and lower than that in the stationary GTAW process [20].

In summary, compared with GTAW process, even though the plasma arc temperature in the KPAW process is much higher, the weld pool temperature is relatively lower

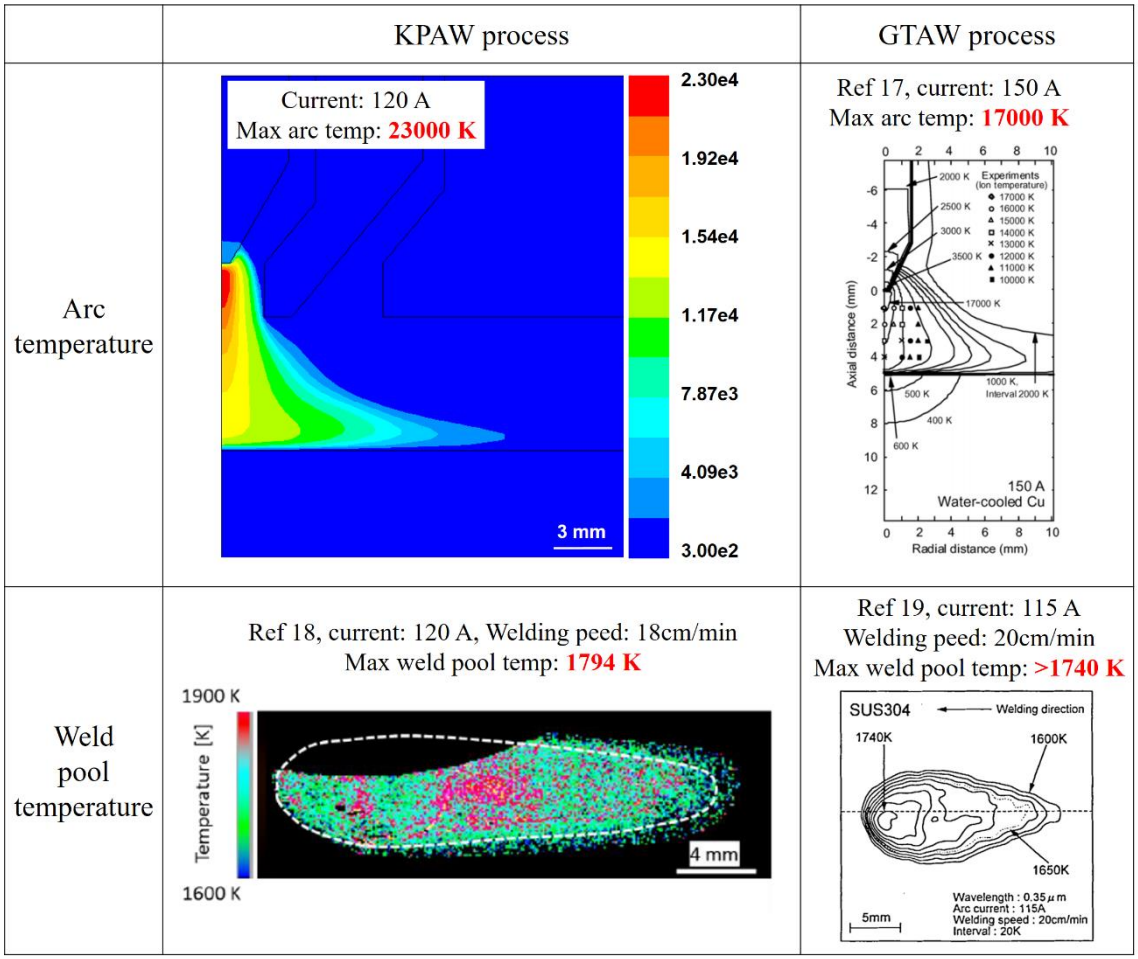

Fig. 1.1 Comparison of arc and weld pool temperatures between KPAW and GTAW processes

1.2.2 Arc pressure is not the only driven force for penetrated keyhole formation

The keyhole formation in the KPAW process is much different from that in the laser beam welding (LBW) process. In the LBW process, due to the much high recoil pressure caused by the metal evaporation, a keyhole with large depth to width ratio is formed in several milliseconds [21]. The keyhole formation is considered as a periodical laser

drilling process on the front keyhole wall [22], and the keyhole depth is determined by the drilling behavior induced by the first absorption of laser energy on the front keyhole wall [23]. The keyhole is more easily formed in the LBW of aluminum alloy, and the keyhole depth is deeper than that in the LBW of steel [24]. Besides, the keyhole in the LBW process is much unstable, causing the generation of keyhole induced porosity [25], spatter [26] and other welding defects [27].

In the KPAW process, the maximum temperature of the weld pool is very low, so the metal evaporation can be ignored [18]. Generally, the keyhole with large width is formed in several seconds, and it is more easily formed in the KPAW of steel than that in the KPAW of aluminum alloy [28]. Usually, the high arc pressure is proposed to be the dominant driven force for the penetrated keyhole formation in the KPAW process [29, 30,31]. As shown in **Fig. 1.2**, Wu et.al proposed that the plasma arc pressure determined the keyholing capability in the KPAW processes; The ultrasonic vibration increased the plasma arc pressure, and thus improved the keyholing capability [29]. Mendez et.al proposed that the high arc pressure contributed to the crater formation below the TIG arc with a high current [32].

It should be noted that the arc pressure in the KPAW process is only several kPa [29], which is similar to that in the high current gas tungsten arc welding (GTAW) process [33] or gas metal arc welding (GMAW) process [34]. Even though the arc pressure is high, a penetrated keyhole is difficult to form in the high current GTAW process or GMAW process.

Many studies also showed that the arc shear stress influenced the penetrated formation or weld pool surface deformation. As shown in **Fig.2**, a simulation without arc shear stress showed that a blind keyhole rather than penetrated keyhole formed inside the weld pool in the KPAW process [35]. Meng et.al [36,37,38] suggested that the effect of the arc pressure on the weld pool deformation was over-estimated in the high current GTAW process, and the arc shear stress was the dominant driven force to facilitate the weld pool deformation. However, the arc shear stress and arc pressure in his studies were calculated based on the empirical equations.

It can be concluded from previous studies that the penetrated keyhole formation mechanism has not been revealed in detail, and the material properties has great influence on the penetrated keyhole formation in the KPAW process.

	KPAW process	GTAW process
Arc pressure	Wu et.al proposed that the plasma arc pressure determined the keyholing capability 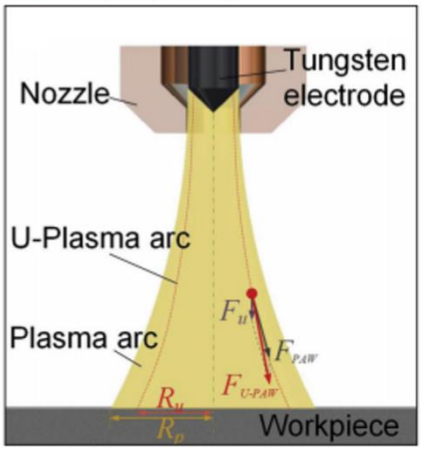	Mendez et.al proposed that the high arc pressure contributed to the crater formation below the TIG arc 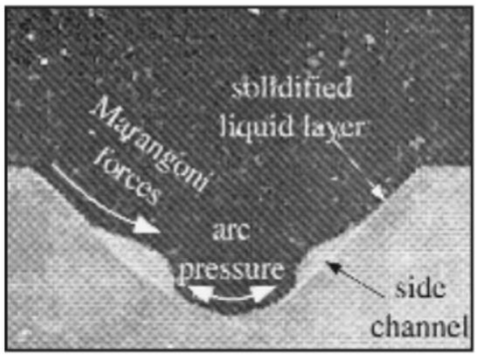
Arc shear stress	A simulation without arc shear stress showed that only blind keyhole formed inside the weld pool. 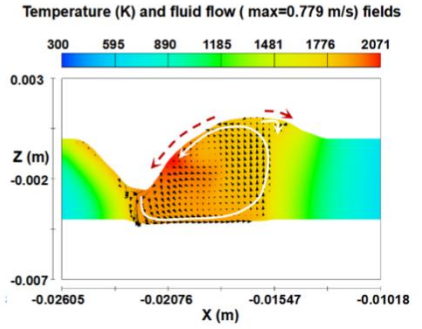	Meng et.al proposed that the arc shear stress was the dominant force for free surface deformation 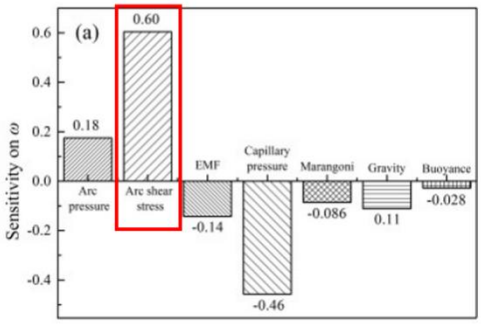

Fig. 1.2 The influences of arc pressure and arc shear stress on the penetrated keyhole or weld pool surface deformation in the KPAW and TIG processes

1.2.3 Low arc energy efficiency

Owing to the strong interaction of the plasma arc, keyhole and weld pool, the energy propagation in the KPAW process is very complex. In the laser welding, due to the multiple reflections and Fresnel absorption by the keyhole [39], the laser energy absorbed by the weld pool is increased. Kawahito et.al measured the absorption of a 10 kW fiber laser beam, and found that the maximum absorptions of the steel and aluminum were 89 and 93% [40]. However, in the KPAW process, the energy efficiency is relatively lower than the gas tungsten arc welding (GTAW) or gas metal arc welding (GMAW) processes.

Tanaka et.al showed that the arc energy efficiency of the GTAW process was 82% [17]. Stenbacka et.al proposed that the average arc energy efficiency value for the GTAW process was about 77% [41]. Joseph et.al measured the arc energy efficiency in the pulsed GMAW process by a liquid nitrogen calorimetry, and suggested that the arc energy efficiency was 68%~72% [42]. Metcalfe et.al [43] proposed that in a 10 kW plasma welding arc, the efficiency of energy to the anode was only 60%~66%. As shown in **Fig. 1.3**, DuPont et.al [44] measured the arc energy efficiency by a Seebeck arc welding calorimeter, and suggested that the consumable electrode processes exhibited the highest arc energy efficiency (84%), followed by GTAW process (67%), and KPAW process (47%). Jiang et.al [45] measured the arc energy efficiency in the variable polarity plasma arc welding (VPPAW) process by a thermal measurement system, and found that the VPPA arc energy efficiency was 46.71% to 61.63%.

It can be concluded that the penetrated keyhole formation can't increase the energy absorption in the KPAW process.

	KPAW process	VPPAW process
Arc energy efficiency	GMAW (84%) > GTAW (67%) > KPAW (47%)	46.71% ~ 61.63%

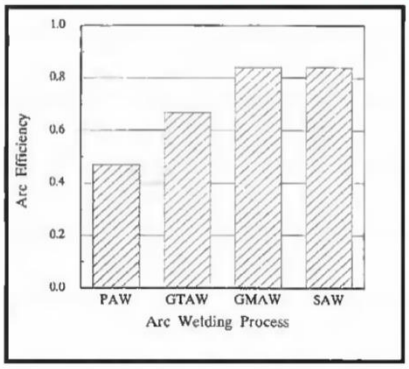

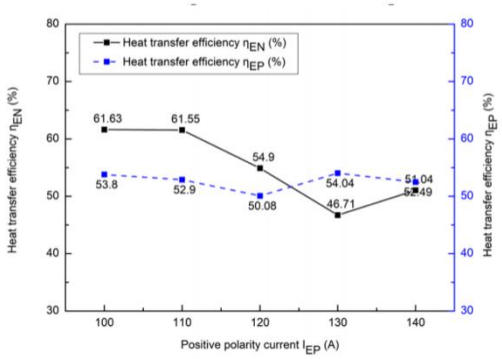

Fig. 1.3 Arc energy efficiency in the KPAW and VPPAW processes

1.2.4 Easy formation of undercutting

The undercut formation mechanism had been widely discussed in the arc welding based on the experimental observation and numerical simulation. In the GTAW process, the inward Marangoni force caused by the positive surface tension temperature coefficient was proposed by Mills to explain the undercut formation [46]. However, the undercut was not generated during the GTAW process of high Sulphur steel (positive surface tension temperature coefficient) with low welding speed. Mendez found that a thin layer of liquid metal was formed under the arc due to the large arc pressure in the high current GTAW

process. The premature solidification of this thin liquid layer initiated the undercut [32]. Meng developed a three dimensional numerical model for the high speed GTAW process [36,38]. The premature solidification of the thin liquid layer at the periphery and the inward flow at the trailing periphery promoted the undercut formation [36]. He also proposed that the arc shear stress was the dominant driven force for the weld pool deformation and backward flow of the liquid metal [38]. However, the arc shear stress and arc pressure in his studies were calculated based on the empirical equations. In the submerged arc welding (SAW) process, based on the X-ray observation, the undercut occurred when the liquid metal was displaced more than the solidification point [47]. The large arc pressure was suggested to be responsible for the undercut formation [48]. In the gas metal arc welding (GMAW) process, Nguyen suggested that the backward flow of the liquid metal caused by the arc pressure and droplet impact was the main reason for the undercut and humping formation [49]. Based on the observation of the weld pool and the movement of the tracer particles, Zong suggested that the large longitudinal to transverse velocity ratio, and the inward flow in the middle of the weld pool contributed to the undercut formation [50,51]. It can be concluded from previous studies that the weld pool convection in the arc welding plays an important role in the undercut formation.

It should be noted that the undercut formation in the KPAW process is much different from that in the GTAW, SAW and GMAW processes. The undercut is likely formed in the GTAW, SAW and GMAW processes with high current and high welding speed [36,48,50], while can be formed in the KPAW process with low current and low welding speed. As shown in **Fig. 1.4**, undercutting formed in the KPAW process with a low current of 120 A, and a low welding speed of 3 mm/s.

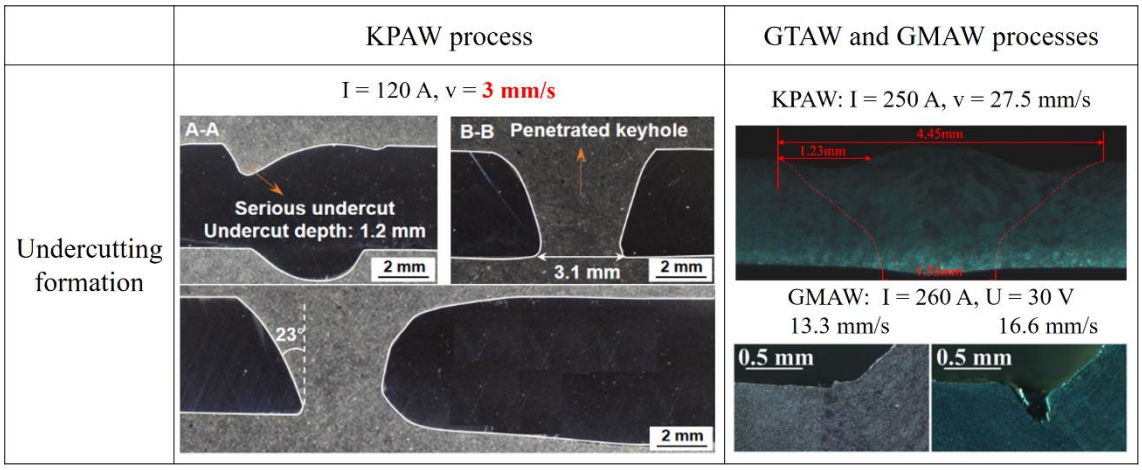

Fig. 1.4 Undercutting formation in the KPAW, GTAW and GMAW processes

This may be caused by the formation of the penetrated keyhole and the complex weld pool convection. Previous studies of full penetration laser welding showed that the molten metal was pressured towards the bottom surface, which caused the redistribution of the thermal energy between the top and bottom welds [52], and facilitated the weld defects formation on the top and bottom surfaces [53].

As shown in **Fig. 1.5**, based on the comprehensive experimental measurement of the weld pool convection with the help of the X-ray transmission system, high-speed video camera system and thermal camera system, Nguyen et.al [10] suggested that the undercut formation was caused by the irregular fluid flow and uneven energy distribution of the weld pool in the KPAW process. As the plasma gas rate is increased, the anti-clockwise eddy inside the weld pool is increased, and the backward flow at the top surface is decreased, so more energy is transported to the bottom surface, while less energy is transported to the top surface. The rear part of the top weld pool is easily solidified, so a teardrop-shaped profile is easily formed. Due to the strong inward flow at the top surface caused by the teardrop-shaped top weld pool profile and the dominant anti-clockwise eddy inside the weld pool, more energy is transported from the lateral sides to the center line of the top weld pool. A high temperature zone is formed at the center line of the top weld pool, while the lateral sides are easily prematurely solidified, causing the undercut formation at the top surface.

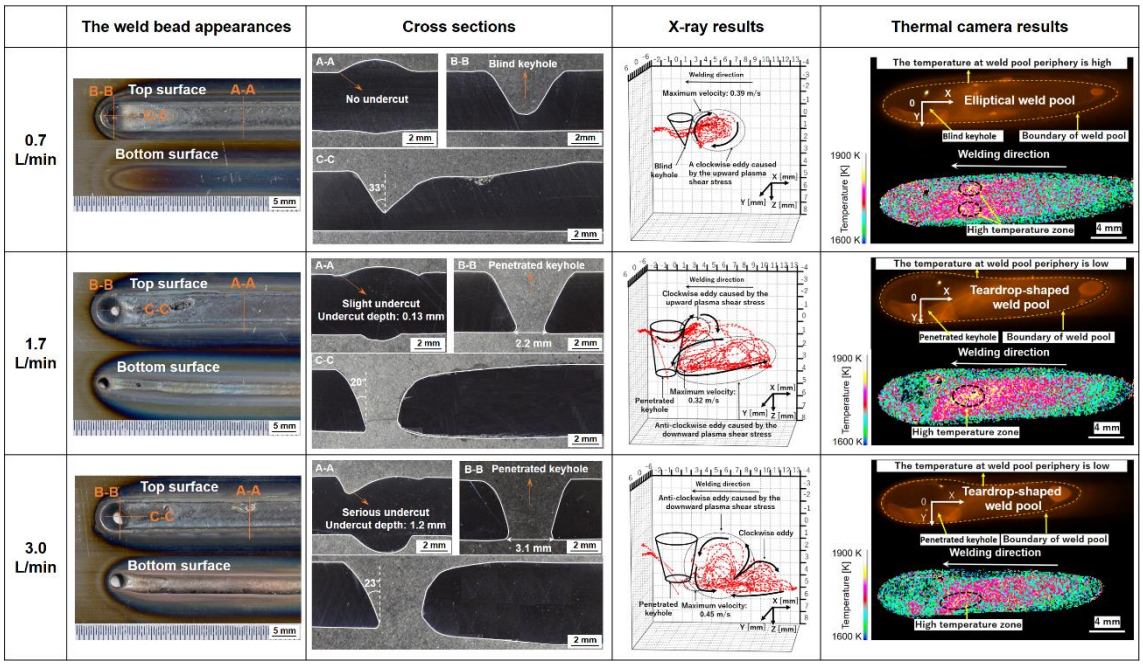

Fig. 1.5 Experimental study of undercutting formation in the KPAW process

1.3 Developing of hybrid KPAW-GMAW welding

As discussed above, weld defects are easily formed in the KPAW process [9,10]. How to suppress the weld defects formation and improve the weld bead quality?

Many improved KPAW processes have been proposed by researchers, such as pulsed controlled KPAW process [54], ultra-sonic assisted KPAW process [29,30,31] and hybrid KPAW-GMAW process [13,55,56]. Among these technologies, the hybrid KPAW-GMAW process combines the advantages of both KPAW and GMAW, such as deep penetration and high quality. As shown in **Fig. 1.6(A)**, the leading plasma arc possesses high energy density and momentum, resulting in a deep penetrated keyhole inside the weld pool. The rearing GMA arc and droplet improve the bead formation. As shown in **Fig. 1.6(B)**, the hybrid KPAW-GMAW process is already successfully adopted in the welding of aluminum thick plates [57,58] and steel [13].

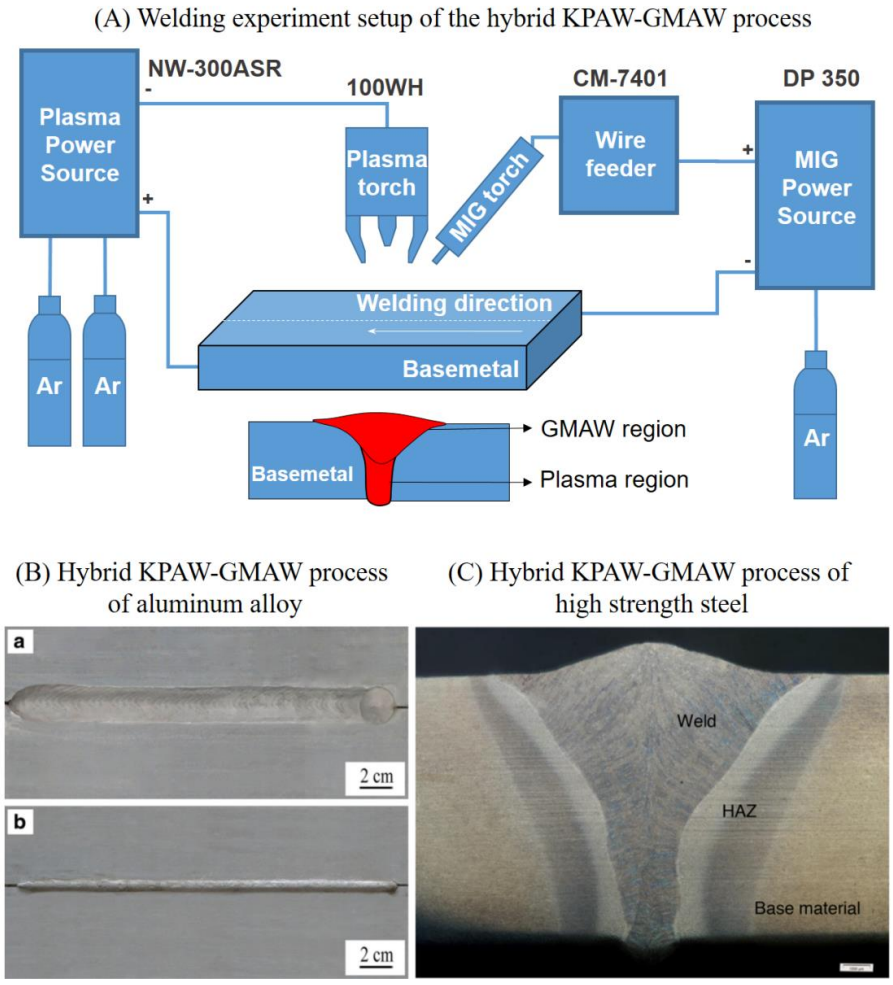

Fig. 1.6 (A) The welding experiment setup of the hybrid KPAW-GMAW process; (B) Hybrid KPAW-GMAW process of aluminum alloy; (C) Hybrid KPAW-GMAW process of high strength steel

Compared with the GMAW process, the hybrid KPAW-P-GMAW process has advantages of higher energy density, deeper weld penetration and higher welding efficiency. The KPAW process can be used to join thick plates with only one pass. However, weld defects, such as undercut, can easily form with a low welding current and a low welding speed [10]. Compared with the KPAW process, the hybrid KPAW-GMAW process has advantages of wider range of process parameters and better weld quality. The hybrid laser-GMAW process [59,60] can join thick plates with high efficiency and quality, but the laser equipment cost is high. The laser focus radius is small, so the joint tolerance is relatively low. Compared with the hybrid laser-GMAW process, the hybrid KPAW-GMAW process has advantages of lower equipment cost and higher joint tolerance. In summary, the hybrid KPAW-GMAW process has a promising future in the welding of thick plates.

1.4 Interactive phenomena in hybrid KPAW-GMAW welding

1.4.1 Interactive phenomena of the arc and droplet

The arc coupling behaviors in other hybrid arc welding processes, such as tandem-TIG [61,62], tandem-GMAW [63,64] and hybrid GTAW-GMAW processes [65,66], have been widely investigated. Both hybrid GTAW-GMAW and hybrid KPAW-GMAW processes are characterized by the formation of the direct current path between the tungsten electrode and GMAW anode (welding wire) [67]. In the hybrid GTAW-GMAW process, cathode spots of the GMA become stable [66,68]. The temperature gradient on the top surface at the middle and rear parts of the hybrid weld pool is lower than that in the conventional GMAW weld pool, while the heat input is increased [66]. Due to the additional heat input and electromagnetic force generated by the GTA, the GMA length increases, and the droplet transfer also becomes easy and stable [66]. In the hybrid KPAW-GMAW process, owing to the strong impingement of the PA, a large keyhole forms [5,6], which may have a great influence on the arc and droplet behaviors. Han et.al [57] proposed that owing to the large number of metal ions and electrons provided by the keyhole, the electrical conductivity of GMA increased in the hybrid variable polarity plasma arc (VPPA)-GMAW process. Besides, the VPPA had a compression effect on the GMA.

Both hybrid laser-GMAW and hybrid KPAW-GMAW are characterized by complex interaction of the arc, droplet and keyhole. In the hybrid laser-GMAW process, due to the

irradiation of the laser beam on the basemetal surface, the metal temperature increases, and intense evaporation occurs [69]. Under the influence of the vaporization induced recoil pressure, a keyhole with a large depth to width ratio generates [70]. Shinn et.al [71] found that a laser can stabilize the arc cathode spots in the hybrid laser-GMAW process of a titanium alloy. Zhang et.al [72] investigated the plasma and droplet behaviors in the hybrid CO2 laser-GMAW process, and proposed that the metal vapor jet from the keyhole acted as a resistant force on the droplet, and suppressed the droplet transfer. Liu et.al [73] calculated the forces acting on the droplet in the hybrid laser-GMAW process, and found that the laser plasma compressed the arc, causing an increase of electromagnetic resistant force of the droplet, so the droplet shape changed and the droplet transfer frequency decreased. However, in the hybrid KPAW-GMAW process, the metal vapor ejected from the keyhole is very weak [18], which will not suppress the droplet transfer. Besides, the phenomenon that the metal vapor ejected from the keyhole cools the arc plasma in hybrid laser-arc process [74,75], will not occur in the hybrid KPAW-GMAW process.

In summary, the interactive phenomena of the arc and droplet in the hybrid KPAW-GMAW process may be significantly different from these in the hybrid GTAW-GMAW and hybrid laser-GMAW processes.

1.4.2 Interactive phenomena of droplet, keyhole and weld pool

An obvious “pull-push” flow pattern defined as a backward molten metal flow after the leading arc, and a forward molten metal flow before the rearing arc, exists on the top weld pool surface between two arcs in the tandem-TIG [76], tandem-GMAW [77] and hybrid GTAW-GMAW [66] processes. It should be noted that the keyhole may have a great influence on the weld pool convection in the hybrid KPAW-GMAW process.

Based on the numerical simulation, Gao et.al [78] predicted an outward flow near the keyhole in the hybrid laser-GMAW process of single-crystal nickel-base superalloys. Zhao et.al [79] measured the fluid flow of the weld pool in the hybrid laser-GMAW process by an advanced X-ray transmission system, and found that the arc shear stress and droplet momentum promoted the inward flow in the keyhole. However, in the hybrid KPAW-GMAW process, the keyhole size is relatively large, and the action areas of the plasma arc pressure and plasma arc shear stress are very large [11], thus the droplet momentum may have a minor influence on the fluid flow near the keyhole.

It can be concluded that the interactive phenomena of droplet, keyhole and weld pool in the hybrid KPAW-GMAW process may significantly differ from these in the hybrid

laser-GMAW process.

1.5 Objectives of this study

The hybrid KPAW-GMAW process characterized by complex interactions of the arc, droplet, keyhole and weld pool is proposed to improve the weld bead formation. In order to better understand the interactive phenomena in the hybrid KPAW-GMAW process, some fundamental phenomena related weld pool convection, keyhole behaviors and energy propagation in the KPAW process are firstly investigated. The objectives of this study are as follows:

(1) Investigate the weld pool convection in the KPAW process based on numerical simulation and experiment. The driven forces for the weld pool convection are discussed. The mechanisms for the low weld pool temperature are revealed.

(2) The keyhole formation mechanisms in the KPAW process are elucidated.

(3) A coupled arc, keyhole and weld pool numerical model is developed to investigate the energy propagation in the KPAW process.

(4) The interactive phenomena of the arc, droplet, keyhole and weld pool in the hybrid KPAW-GMAW process are elucidated.

1.6 Structure of this study

As shown in **Fig. 1.7**, this thesis consists of seven chapters. Chapter 1 is introduction and literature review. In Chapter 2, Chapter 3 and Chapter 4, the weld pool convection, keyhole formation and energy propagation in the KPAW process are analyzed.

In chapter 5 and chapter 6, the interactive phenomena of the arc, droplet, keyhole and weld pool in the hybrid KPAW-GMAW process are analyzed. In chapter 7, all the findings are concluded.

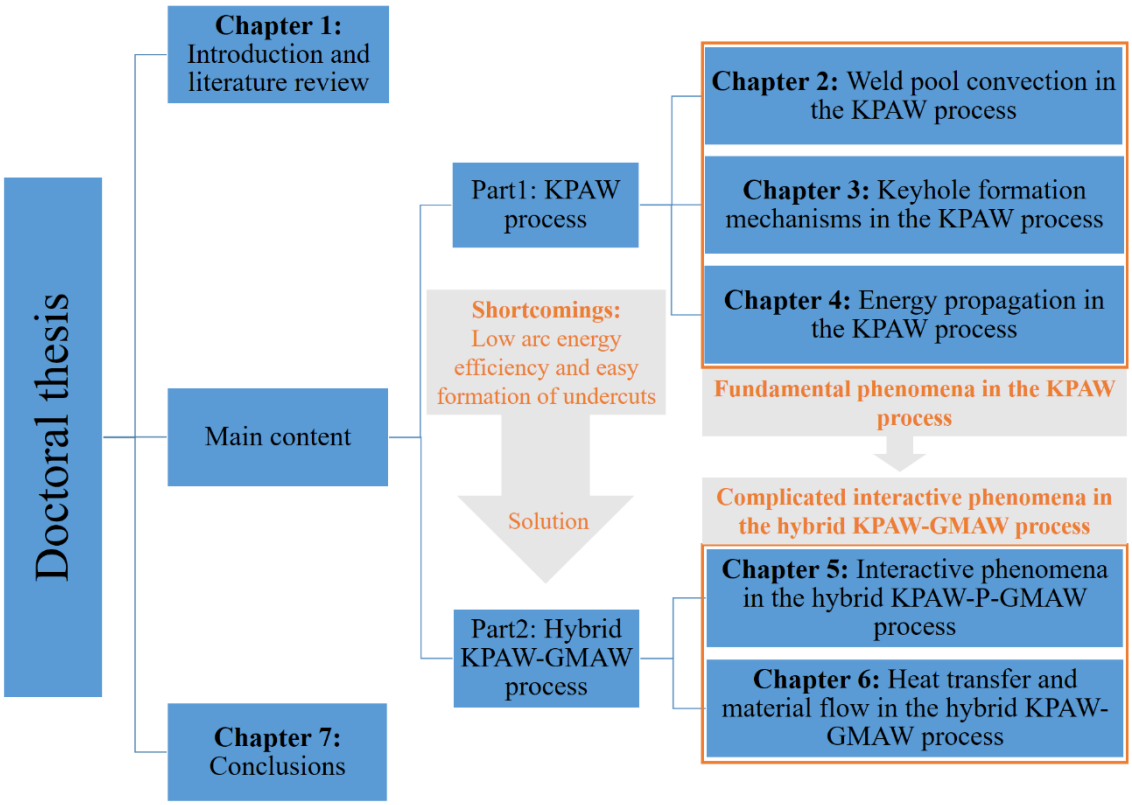

Fig. 1.7 Structure of this study

Chapter 2 Elucidation of the weld pool convection in the keyhole plasma arc welding process

2.1 Introduction

Different sensing and observation methods had been carried out to study the weld pool convection in the KPAW process [80,81]. However, owing to the complexity of the KPAW process, detail information of the weld pool convection is difficult to be obtained only by experimental methods, so numerical simulation is also used to better understand the thermo-physical behaviors of the KPAW process. Fan [82] built a two dimensional model to investigate the keyhole formation and keyhole closure in the KPAW process. In this model, the heat source was not changed with the keyhole geometry. The combined volume heat source models changed with the keyhole shape were proposed to simulate the three dimensional temperature and fluid flow fields in the KPAW process [83-85]. However, the time for the open keyhole formation was very short in their numerical simulations. Li [86] built a 3D transient numerical model for KPAW process to investigate influences of the keyhole shape and size on the arc heat flux and pressure distribution. However, the shear stress caused by plasma flow was ignored in above studies [83-86]. As known to all, the shear stress, arc pressure, Marangoni force, Lorentz force and buoyancy force are five principal forces for the melt flow in the KPAW process. Based on the comprehensive experimental measurement of weld pool convection, the shear stress due to the plasma flow was found to be the dominant driven force in the KPAW weld pool [18]. So without considering the shear stress, the weld pool convection was much different from experimental results.

Pan [16] proposed a coupled tungsten-plasma-anode mathematic model to analyze the heat transfer and fluid flow in the stationary KPAW process, and found that the outward convection on the weld pool surface was induced by the shear stress and Marangoni force. Jian also developed a unified 3D model to study the interaction mechanisms of the plasma arc, weld pool and keyhole in the stationary KPAW process [87], and moving KPAW process [88]. However, the bottom surface deformation, and the fluid flow on the bottom surface were ignored in their numerical simulations. Based on the experimental study, the backward flow of the molten metal can be observed on the bottom surface [18]. When a penetrated keyhole is formed in the KPAW process, special treatments on the heat source

and shear stress should be considered in the numerical model.

In this study, an electrode-arc model, and a three dimensional weld pool model are developed to investigate the weld pool convection in the KPAW process. The self-adaptive heat source, the shear stress caused by plasma flow, and deformations of the top and bottom surfaces are considered in the numerical model. An X-ray transmission system is used to estimate convective patterns inside the weld pool. A high-speed video camera is used to measure the convective patterns on weld pool surfaces. A thermal camera is used to measure the weld pool surfaces temperature. For the first time, the convective patterns inside the weld pool measured by the X-ray are predicted by numerical simulation. The reasons for the low weld pool temperature are discussed.

2.2 Mathematical model and numerical simulation

As shown in **Fig. 2.1**, an electrode-arc model is firstly built for the KPAW process to study plasma arc physics. The important parameters related to the current density, arc pressure and plasma shear stress are obtained. Then a three dimensional weld pool model is developed to investigate the weld pool convection and keyhole formation in the KPAW process, in which special treatments on the heat source, arc pressure and plasma shear stress are considered.

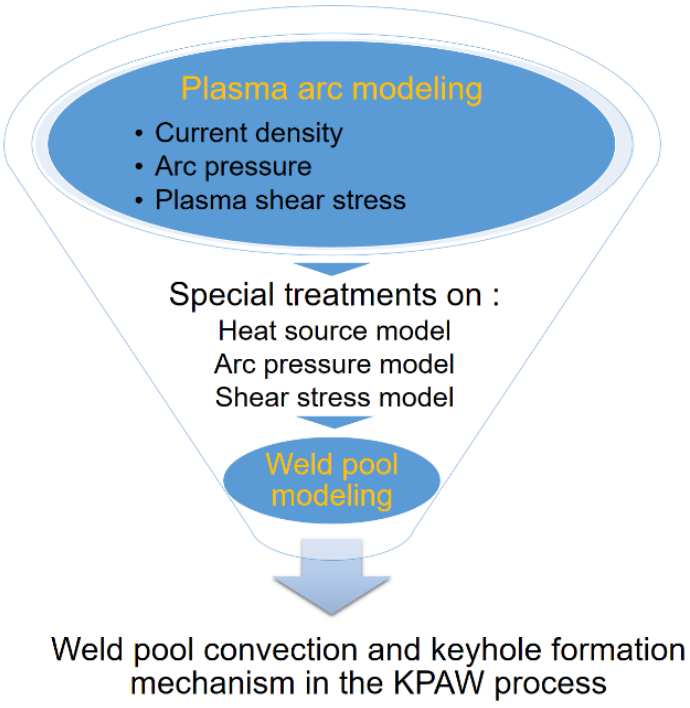

Fig. 2.1 The framework of the whole mathematic model

In the electrode-arc model, the mesh size is 0.1 mm in the electrode region, and 0.2 mm in the nozzle and gas regions. The detail information of the model can be seen in our previous work [89]. In order to verify the accuracy of our model, the welding parameters are obtained from previous study, and the numerical results are compared with experimental results [29]. When the welding current is 120A and the torch orifice diameter is 3.2mm, as shown in **Fig. 2.2(A)**, the maximum temperature of the arc is 23400K. As shown in **Fig. 2.2(B)**, the maximum calculated arc pressure is 1778 Pa, which is similar to that obtained by the experiment (1820 Pa).

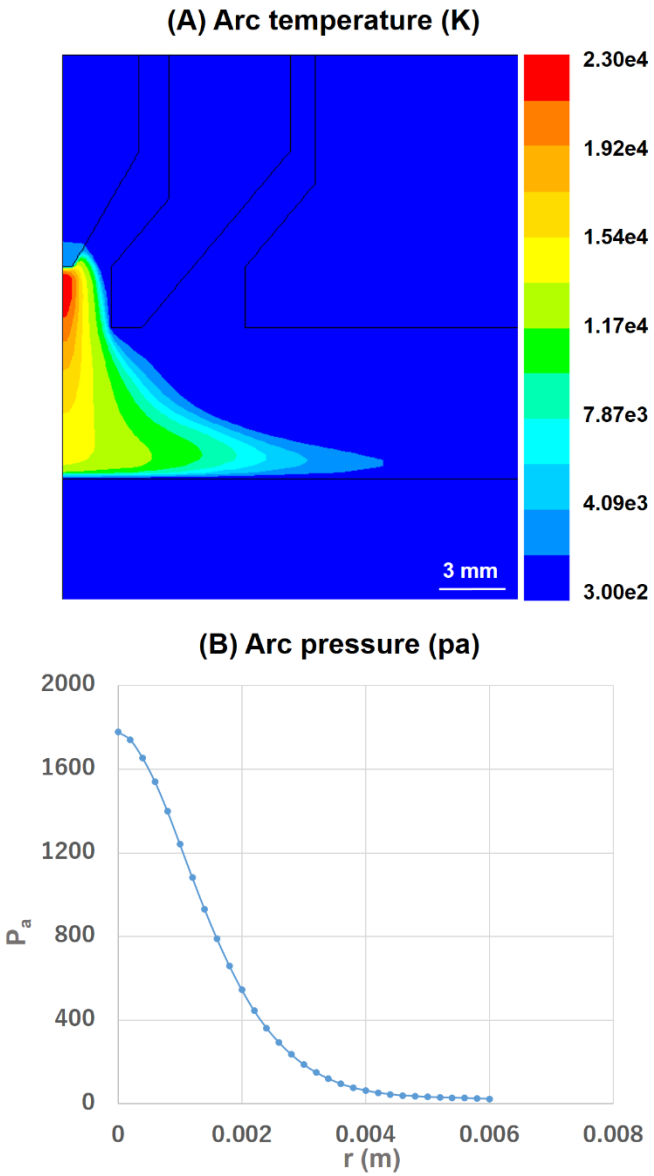

Fig. 2.2 Plasma arc modeling: (A) Arc temperature; (B) Arc pressure

In the weld pool model, some assumptions have been made: (1) The flow is laminar, and the liquid metal is considered as a Newtonian and in-compressible fluid. (2) The gas phase (plasma gas and shielding gas) is omitted. (3) Owing to the low weld pool temperature, the metal evaporation from the weld pool is ignored.

Four governing equations including mass, momentum, energy conservation equations, and VOF (Volume of Fluid) equations [90] are solved to calculate the heat and mass transfer in the KPAW weld pool. The enthalpy-temperature relationship is used to model the solid-liquid phase change [91] and the porous media drag concept is used to model the flow in the mushy zone [92]. The main driven forces of the weld pool are shear stress, arc pressure, Marangoni force, Lorentz force, and buoyancy force. The governing equations, surface tension, Lorentz force, buoyancy force and boundary conditions are similar to our previous works [77]. In this section, only the special treatments on the heat source, arc pressure and plasma shear stress are discussed.

2.2.1 Self-adaptive heat source model

The Gaussian distributed heat source model [82,85], the combined volume heat source models [83,84,85] were used in previous studies. In this study, the VOF method is used to track the free surface of the weld pool. However, due to the large deformation of the weld pool surface in the KPAW process, as shown in **Fig. 2.3**, the total number of free surface cells is increased. If the Gaussian distributed heat source model is used, the total energy absorbed by the free surface is overestimated.

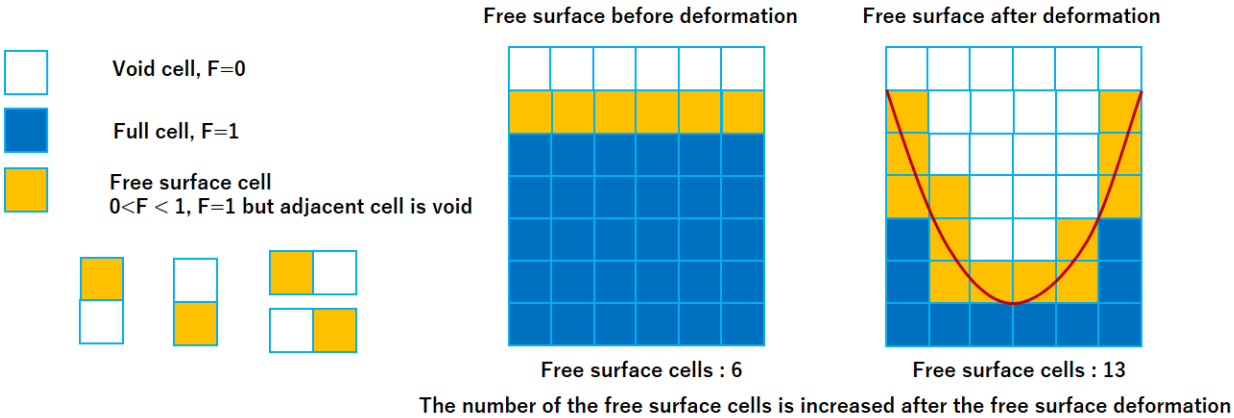

Fig. 2.3 The selection of the free surface before and after deformation

It should be noted that before the penetrated keyhole formation, only the top free surface is heated by the arc plasma. After the penetrated keyhole formation, both the top

and bottom free surfaces are heated by the arc plasma, as shown in **Fig. 2.4(A)** and **(B)**. Based on Xu's study [32], after the penetrated keyhole formation, the welding current mainly flows from the upper part of the base metal to the tungsten, so the decrease of heat flux caused by the increase of the arc length should be considered in the heat source model.

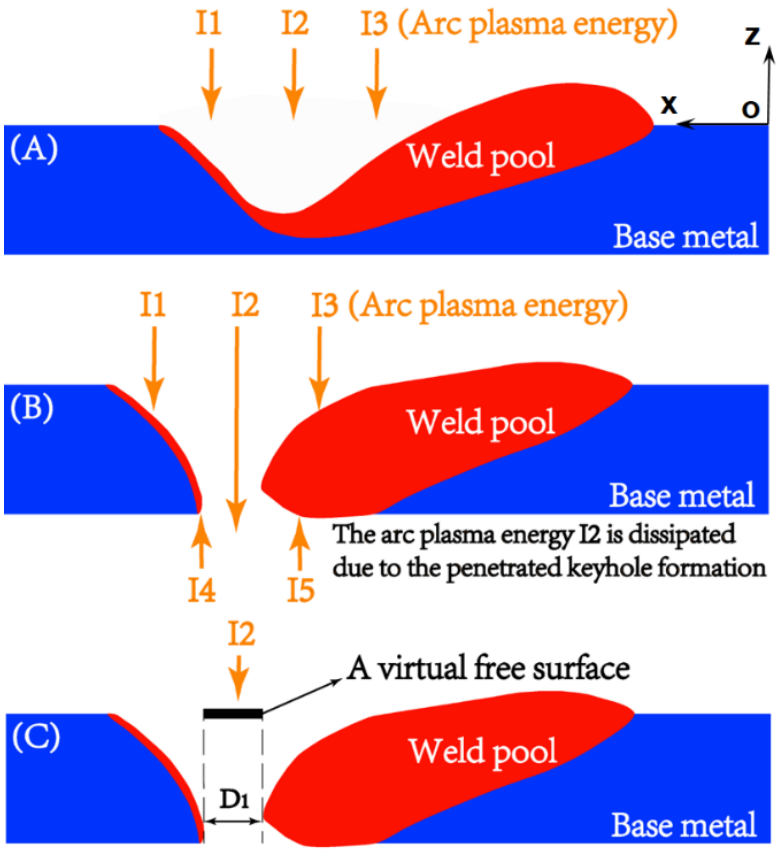

Fig. 2.4 The heat source model: (A) The energy absorbed by the top free surface; (B) The energy absorbed by both the top and bottom free surfaces; (C) The calculation of I_2

In this study, a self-adaptive heat source model is adopted. Before the penetrated keyhole formation, as shown in Eq. (2.1), the heat source is considered as Gaussian distributed. The shape function of the keyhole wall L_q is introduced in the heat source model to consider the decrease of heat flux, as shown in Eq. (2.2). A global controlling parameter K_q is introduced to conserve the total energy absorbed by the free surface, which is calculated by Eq. (2.3).

$$q(x,y,z)=K_q L_q \frac{3\eta UI}{\pi r_q^2}\exp\left\{-\frac{3(x-vt)^2+3y^2}{r_q^2}\right\} \tag{2.1}$$

$$L_q = (1 - \frac{Z_k}{H_b + H_{nb}})^2 \quad (2.2)$$

$$\eta UI = \iint q(x, y, z) \quad (2.3)$$

Where *x, y, z* are coordinates, η is arc power efficiency, *U* is the arc voltage, *I* is the welding current, r_q is the effective radius of the heat source, *v* is the welding speed, *t* is the time, Z_k is the distance between the cell center and the top of the base metal, H_b is the thickness of the base metal, H_{nb} is the distance between the nozzle and the top of the base metal.

After the penetrated keyhole formation, as shown in Eq. (2.4), the heat source is considered as double-ellipse distributed. As shown in **Fig. 2.4(B)**, the arc plasma energy I_2 is dissipated, so the total energy absorbed by the top and bottom free surfaces is equal to $\eta UI - I_2$. I_2 is assumed to be equal to the energy absorbed by the virtual free surface at the top of the base metal, as shown in **Fig. 2.4(C)**, and the K_q is calculated by Eq. (2.5).

$$\begin{aligned} \mathrm{q(x,y,z)} &= K_q L_q \frac{6\eta UI}{\pi(a_f + a_r)b} \exp\left\{-\frac{3(\mathrm{x} - vt)^2}{a^2} - \frac{3y^2}{b^2}\right\} \\ \mathrm{a} &= \begin{cases} a_f & x < vt \\ a_r & x \geq vt \end{cases} \end{aligned} \quad (2.4)$$

$$\eta UI - I_2 = \iint q(x, y, z) \quad (2.5)$$

Where a_f, a_r and *b* are the distribution parameters of the double-ellipse heat source. In this study, before and after the penetrated keyhole formation, a same arc power efficiency (0.6) is used.

2.2.2 Arc pressure model

Li [86] considered the plasma arc pressure varying with the dynamic keyhole wall. In his study, the arc pressure was decreased from the top to the bottom of the base metal. However, based on Xu's study, the formation of a keyhole in the KPAW process was believed to have great influences on the arc pressure. From the top to the bottom of the base metal, the plasma arc pressure was decreased firstly, and then increased due to the additional constraint of the keyhole [93].

For simplicity, in this study, from the top to the middle of the base metal, the arc pressure is assumed to be linearly decreased, and from the middle to the bottom of the base metal, the arc pressure is assumed to be linearly increased. The parameter K_p calculated based on Xu's study is introduced to control the variation of the arc pressure. It should be noted that K_p is negative from the top to the middle of the base metal, and is positive from the middle to the bottom of the base metal.

$$p(x,y,z) = (1 + K_p \bullet Z_k)\, p_{max} \exp\left\{-\frac{3(x^2+y^2)}{r_p^2}\right\} \tag{2.6}$$

Where P_{max} is the maximum arc pressure, r_p is the effective radius of the arc pressure. P_{max} and r_p are obtained from numerical results, as shown in **Fig. 2.5**. Here, a small torch orifice with diameter 2.0 mm is used, so the maximum arc pressure is 4532 Pa.

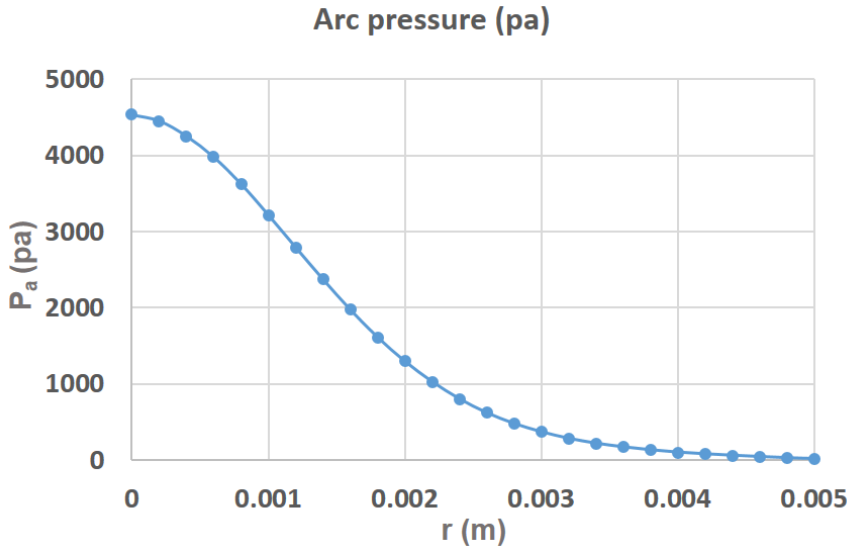

Fig. 2.5 The arc pressure distribution

2.2.3 Plasma shear stress model

In the simulations of the GTAW process [94] and GMAW process [95], the Phares's model [96] was used to consider the shear stress caused by plasma flow. It should be noted that the Phares's model is used to determine the shear stress produced by the normal impingement of a jet on a flat surface. In the GTAW process and GMAW process, the deformation of the weld pool surface is small, so the weld pool surface can be regarded as a flat surface. However, In the KPAW process, the weld pool surface is largely

deformed, so an improved shear stress model should be adopted.

Before the penetrated keyhole formation, the direction of the shear stress at the keyhole wall is upward, as shown in **Fig. 2.6(A)**. The value of the shear stress is obtained from numerical results, as shown in **Fig. 2.7**.

After the penetrated keyhole formation, the reverse flow can be observed at the top part of the keyhole wall [93]. In this study, it is assumed that the direction of shear stress is upward at the top part of the keyhole wall, but downward at the bottom part of the keyhole wall, as shown in **Fig. 2.6(B)**.

At the top part of the keyhole wall, the value of shear stress caused by the reverse flow can be expressed as below:

$$\tau(x, y, z) = \alpha_{top}\tau \tag{2.7}$$

At the bottom part of the keyhole wall, the plasma velocity is relatively low, and the value of shear stress can be expressed as below:

$$\tau(x, y, z) = \frac{8\rho_{Ar}U_0^2}{\mathrm{Re}} \tag{2.8}$$

It should be noted that Eq. (2.8) is used to determine the value of shear stress induced at the cylindrical keyhole walls by the vapor [97]. However, the shape of the keyhole in the PKAW process is in dynamically changing, so it is important to calculate the shear stress vector at each free surface cell.

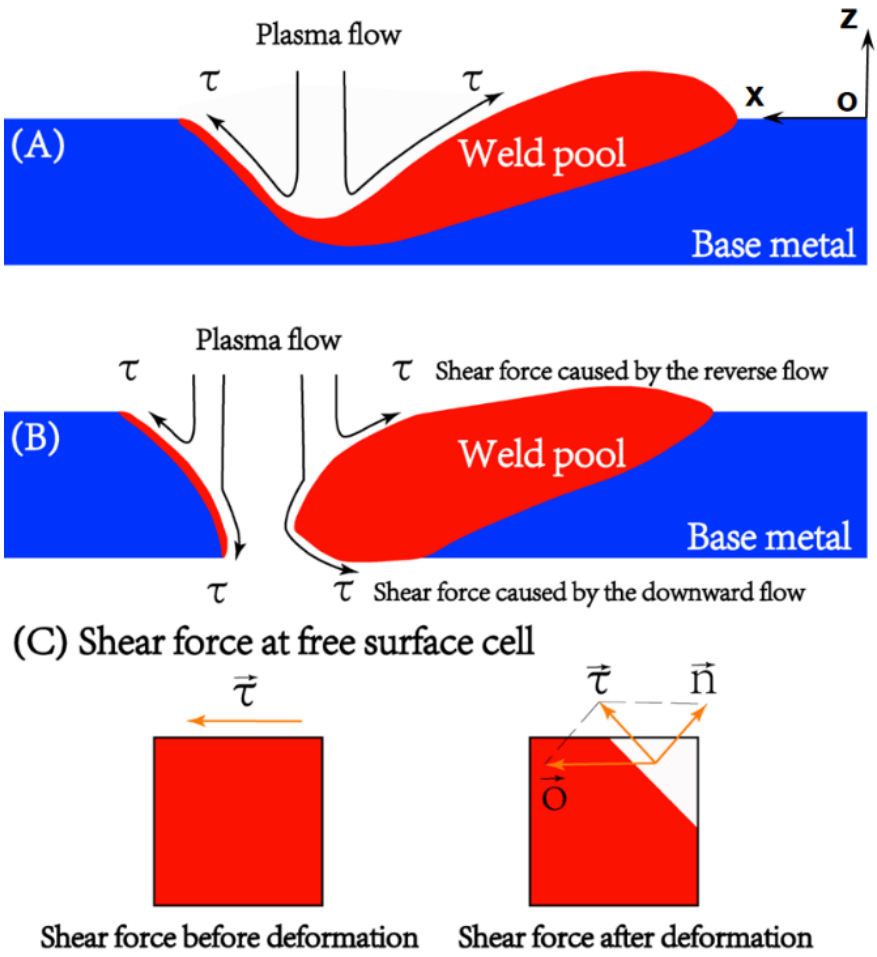

Fig. 2.6 The shear stress model: (A) The shear stress model before the penetrated keyhole formation; (B) The shear stress model after the penetrated keyhole formation; (C) The shear stress at free surface wall

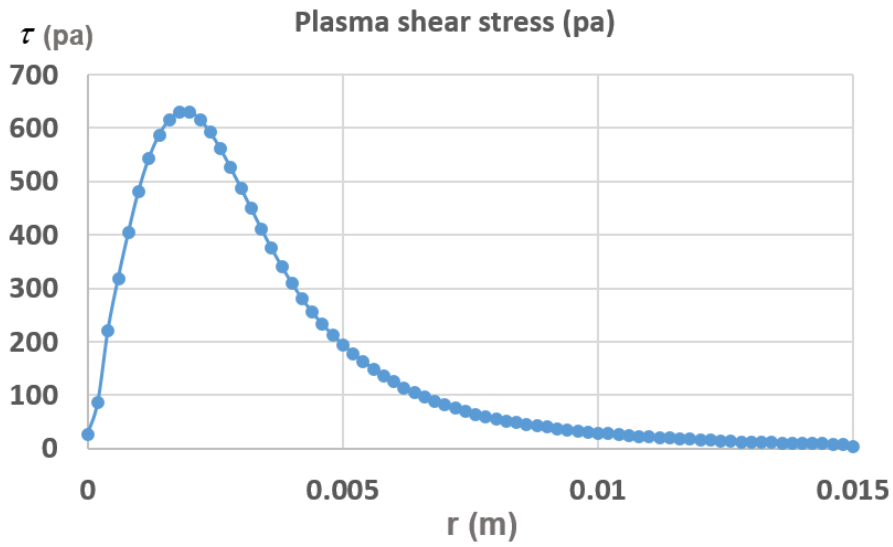

Fig. 2.7 The plasma shear stress distribution

As shown in **Fig. 2.6(C)**, before the free surface deformation, the direction of shear stress is horizontal. After the free surface deformation, the shear stress is redirected. It is assumed that the horizontal vector $\vec{o}$, redirected shear stress vector $\vec{\tau}$, and free surface normal vector $\vec{n}$ are coplanar, so the redirected shear stress vector can be determined as:

$$\begin{cases} \vec{\tau} \cdot \vec{n} = 0 \\ |\vec{\tau}| = \tau(x, y, z) \\ \vec{\tau} = A\vec{o} + B\vec{n} \end{cases} \tag{2.9}$$

Where U_0 is the average plasma jet speed inside the keyhole after penetration. Re is the Reynolds number of the plasma inside the keyhole after penetration. α_{top}, A and B are real numbers.

2.2.4 Numerical simulation

The commercial CFD (Computational Fluid Dynamics) software FLOW3D is used to solve the governing equations and VOF equation. Finite volume method is applied to discrete the governing equations. Due to the symmetry, half of the computational domain is used in the actual calculation, which is 50 mm in length (x-axis), 15 mm in width (y-axis), and 10 mm in thickness (z-axis). The plate thickness is 4 mm, and the other parts are void region. The mesh size is 0.2 mm. The origin of z-axis locates at the top surface of the plate. The details of the iteration scheme can be found in our previous work [30].

The thermo-physical material properties of SUS304 stainless steel can be seen in **Table 2.1**, which are obtained from previous study [98] and the fluid database of FLOW3D. It can be seen from previous studies that the numerical results agree well with experimental results when constant material properties are used [98,99]. Besides, the temperature of the weld pool in the KPAW process is relatively low, so the constant material properties are also used in this study.

Table 2.1 Thermo-physical material properties of SUS304 stainless steel

Nomenclature	Value	Nomenclature	Value
Density (kg/m^3)	6900	Liquidus temperature(K)	1727
Viscosity (kg/m·s)	0.0059	Solidus temperature	1697
Specific heat (l) (J/kg·K)	720	Boiling temperature(K)	3133
Specific heat (s) (J/kg·K)	760	Heat transfer coefficient (W/m^2·K^4)	20
Latent heat of fusion(J/kg)	2.47×10^5	Coefficient of thermal expansion(K^{-1})	1.5×10^{-4}

Thermal conductivity (l) (W/m·K)	28.4	Surface tension(N/m)	1.8
Thermal conductivity (s) (W/m·K)	33.2	Surface tension gradient(N/m·K)	-0.00043

2.3 Experimental method

The welding equipment consists of a transfer-type plasma arc welding torch (100WH, Nippon Steel Welding & Engineering Co., Ltd.) and a welding power source (NW-300ASR, Nippon Steel Welding & Engineering Co., Ltd.). As shown in **Fig. 2.8**, An X-ray transmission system is used to observed the movement of tungsten particles, so the convective patterns inside the weld pool can be estimated. A high-speed video camera is used to observe the movement of Zirconia particles on the weld pool surfaces, so the convective patterns on the top and bottom surfaces can be measured. A thermal camera (Miro Ex4 Phantom, Vision research Inc.) including three color sensors composed of Red (R), Green (G) and Blue (B) is used to take the weld pool surfaces images. The base metal used in the experiments is stainless steel SUS304 plates with a dimension of 300 mm x 100 mm x 4 mm.

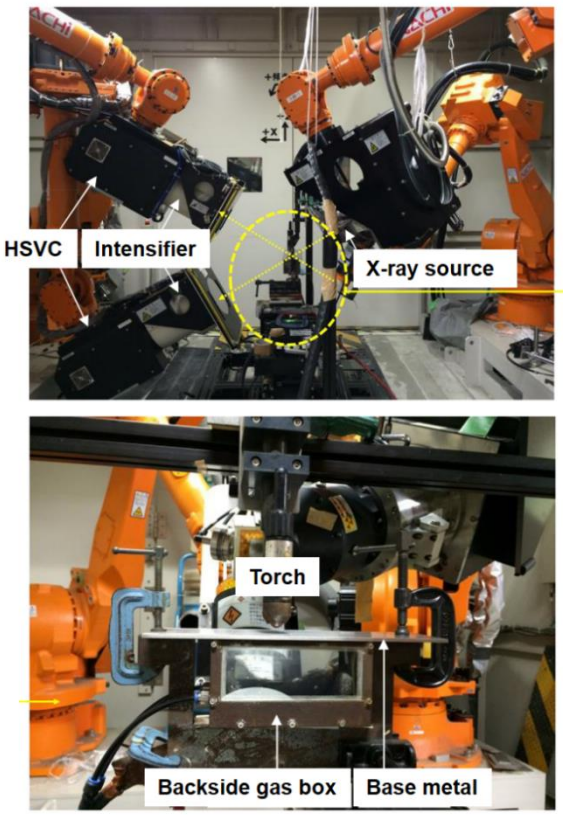

Fig. 2.8 The photographs of the welding equipment and X-ray transmission system [35]

A small torch orifice with a diameter of 2.0 mm is used in the experiments. The

electrode setback is 3 mm. The distance between the nozzle and the base metal is 5 mm. The welding speed is 3 mm/s. The pure Ar is used as the main plasma gas and the shielding gas. In order to protect the back weld bead formation, a back-shielding gas box is put on the welding jig. The main plasma gas flow rate is 1.7 l/min, and the shielding gas flow rate is 7.5 l/min. The main current is DC120 A, and the output arc voltage is approximately 27 V. The detail descriptions of the experimental methods can be seen in our previous work [18]. The same welding parameters are used in the numerical simulation.

2.4 Results and discussion

2.4.1 Weld pool convection

2.4.1.1 Before the penetrated keyhole formation

When the plasma arc with high energy impinges on the base metal surface, the metal is melted. At the beginning, the top surface deformation is small. At about t=0.6 s, as shown in **Fig. 2.9(A)**, the large deformation of the top surface can be observed, and the molten metal is pushed from the arc center to the weld pool edge. A gouging region with few molten metal is formed under the arc. The temperature of the molten metal near the arc center is high. At about t=1.2 s, as shown in **Fig. 2.9(B)**, the top surface is largely deformed, and a deep blind keyhole is generated. The front keyhole wall is very thin. The molten metal flows backward along the rear keyhole wall due to the plasma shear stress and Marangoni force, so a large swelling is formed at the rear part of the weld pool. It can be seen that there are two convective eddies formed inside the weld pool. An anti-clockwise eddy is formed near the arc center under the influence of the arc pressure and Lorenz force, and a clockwise eddy is formed at the rear part of the weld pool under the influence of the plasma shear stress and Marangoni force. In **Fig. 2.9(C)**, the keyhole depth is increased, and the temperature is uniformly distributed on the weld pool surface. Besides, the size of the clockwise eddy is increased. In **Fig. 2.9(D)**, the convective patterns of the weld pool are unchanged, while the weld pool length and keyhole depth are increased.

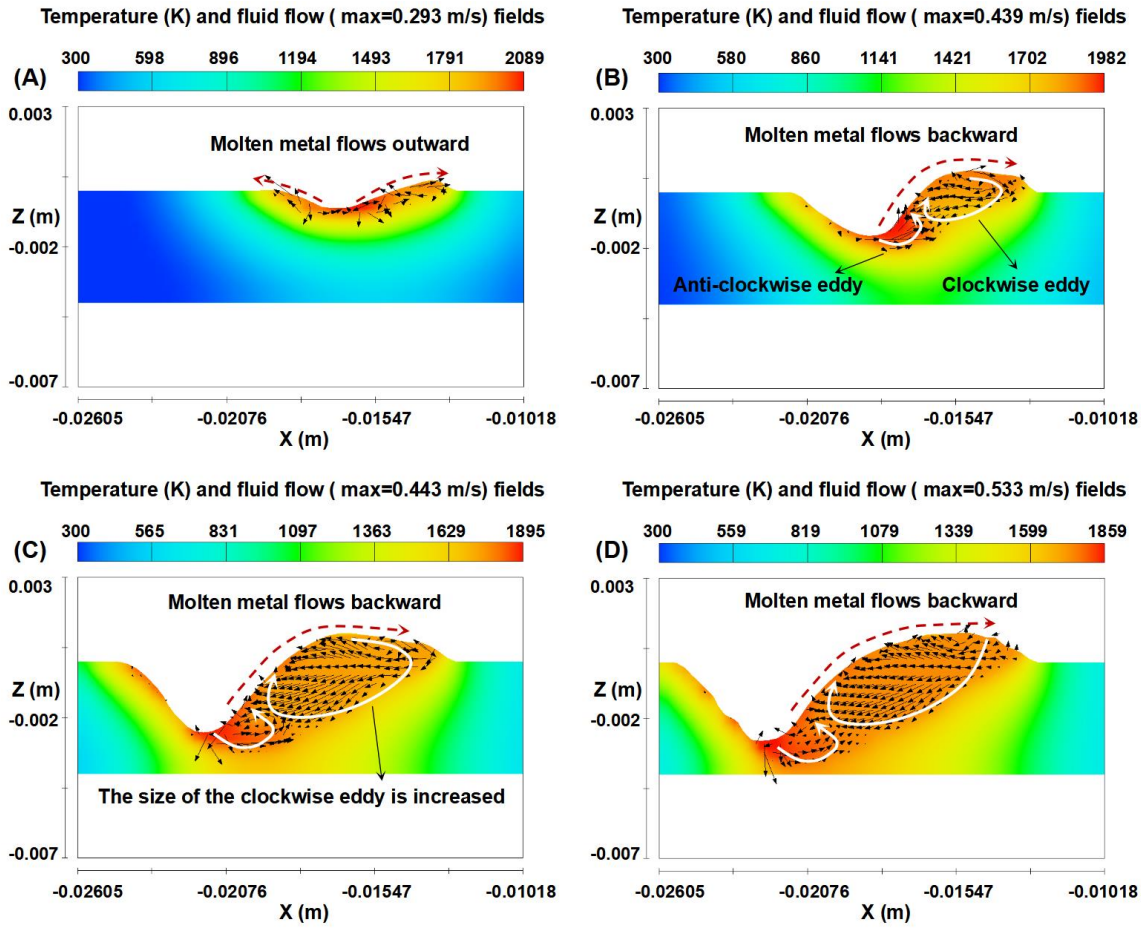

Fig. 2.9 Temperature (K) and fluid flow fields of y=0 cross sectional view at: (A) t= 0.6 s; (B) t= 1.2s; (C) t= 2.2 s; (D) t= 2.5 s

An interesting thermo-physical phenomenon confirmed by experiment is that even though the heat flux density of the KPAW process is much high, the temperature of the weld pool is low. Based on Anh's study [18], the maximum temperature on the top and bottom surfaces of the weld pool was about 1800 K, which was similar to that in the moving GTAW process [19], and lower than that in the stationary GTAW process [20]. As shown in **Fig. 2.9**, under the arc center, the temperature of the molten metal is the highest, and its value is about 1900 K. The reasons for this phenomenon are explained as follows.

The simulation without the arc pressure and plasma shear stress is carried out. As shown in in **Fig. 2.10**, the weld pool deformation is small, and the maximum velocity of the fluid flow is very low. The maximum temperature of the weld pool is more than 2600 K.

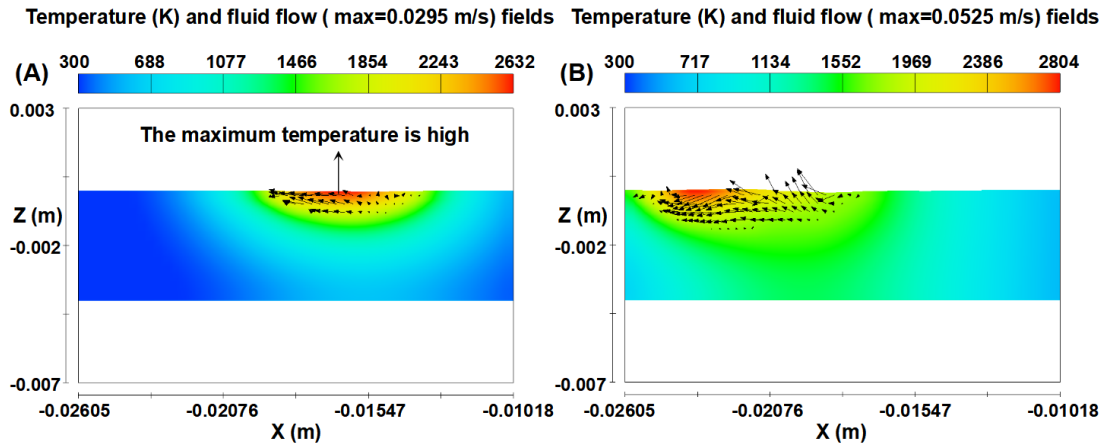

Fig. 2.10 Temperature (K) and fluid flow fields of y=0 cross sectional view at: (A) t= 0.6 s; (B) t= 2.5 s (Simulation without the arc pressure and plasma shear stress)

The simulation without the arc pressure is carried out. As shown in **Fig. 2.11(A)**, the molten metal flows outward from the arc center with high velocity. In **Fig. 2.11(B),** the weld pool surface is largely deformed. The molten metal flows backward, and a clockwise eddy is formed at the rear part of the weld pool. The maximum temperature of the weld pool is more than 2000 K.

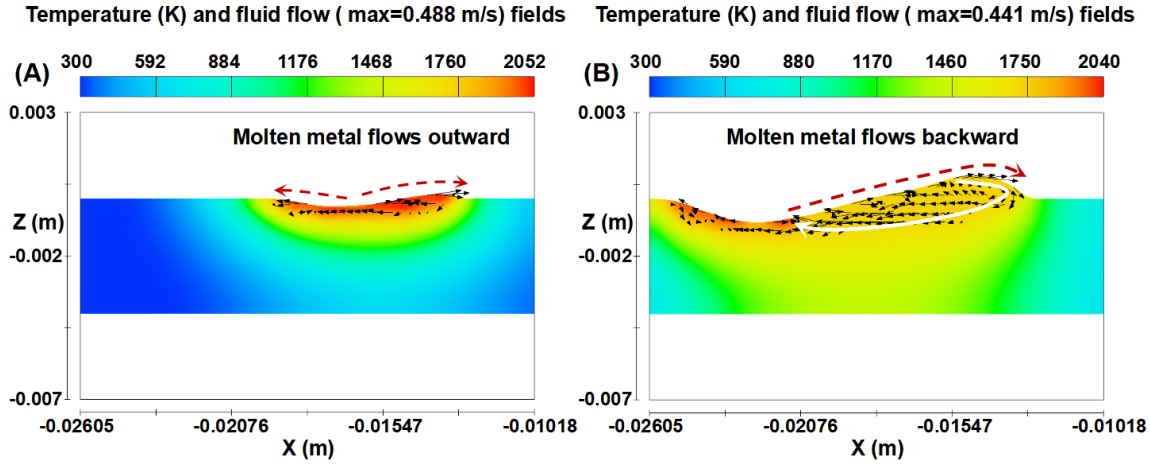

Fig. 2.11 Temperature (K) and fluid flow fields of y=0 cross sectional view at: (A) t= 0.6 s; (B) t= 2.5 s (Simulation without the arc pressure)

The simulation without the plasma shear stress is carried out. As shown in **Fig. 2.12(A)**, an anti-clockwise eddy is formed inside the weld pool under the influence of the arc pressure and Lorenz force. The fluid flow is strong. In **Fig. 2.12(B)** and **Fig. 2.12(C)**, a blind keyhole is formed. The molten metal near the rear keyhole wall flows inward, and the size of the anti-clockwise eddy is increased. The maximum temperature of the weld pool is more than 2000 K.

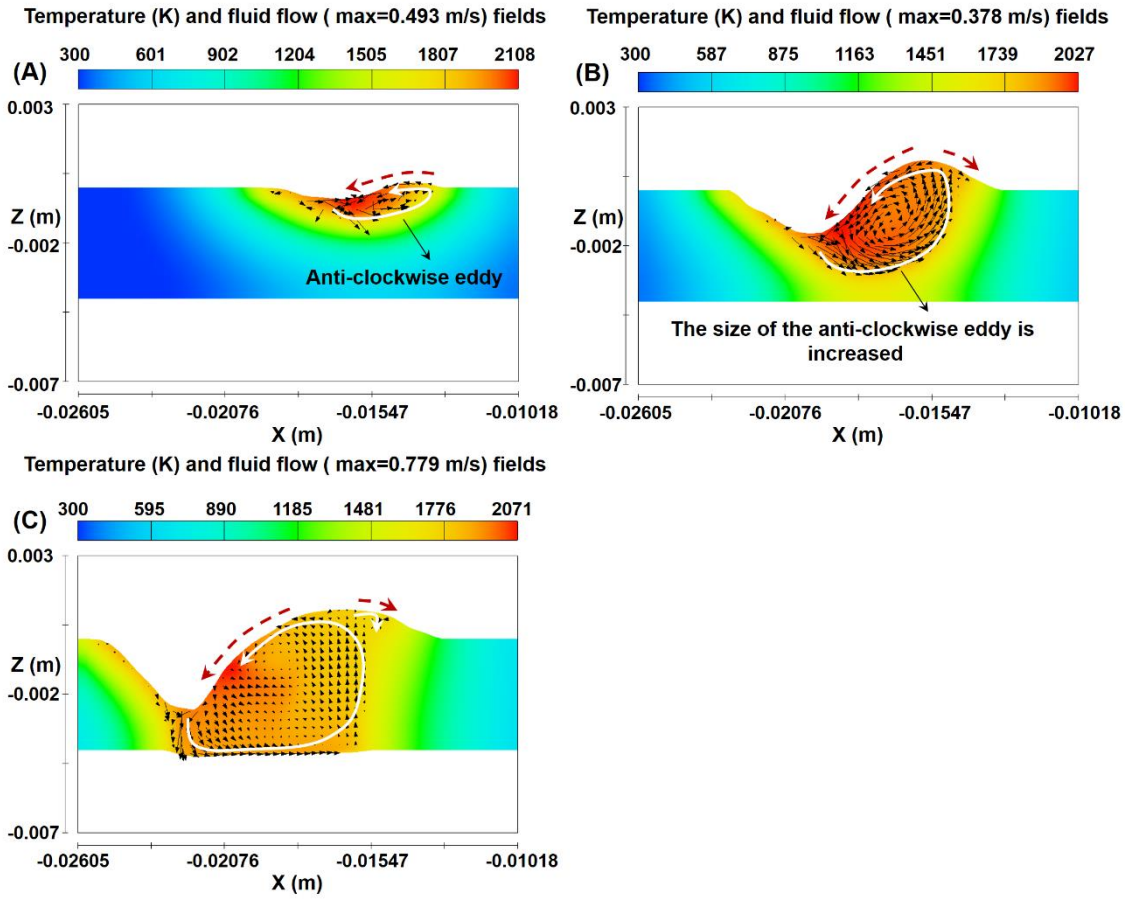

Fig. 2.12 Temperature (K) and fluid flow fields of y=0 cross sectional view at: (A) t= 0.6 s; (B) t= 1.6 s; (C) t= 2.5 s (Simulation without the plasma shear stress)

The Peclet number of the weld pool is calculated. Based on equation (2.10), its value is about 980. The Peclet number of the weld pool in double electrodes tungsten inert gas welding is only 77 [100]. The Peclet number is a dimensionless number showing the ratio between convection and conduction. The much high Peclet number means that the heat transportation by the fluid flow is the dominant mechanism for energy transportation inside the weld pool.

$$Pe = \rho CVL/K \tag{2.10}$$

Where ρ is fluid density (6900 kg/m^3). C is specific heat (720 J/kg·K). L is the characteristic length (Molten pool length: 0.014 m). V is the characteristic velocity (0.4 m/s). K is the thermal conductivity (28.4 W/m·K).

Based on our numerical simulation, the arc pressure and plasma shear stress are the two most important driven forces for the fluid flow in the KPAW process. The significance of shear stress had been revealed in the previous studies of the GTAW process. The unified model developed by Tanaka et al. [17] suggested that the fluid flow

in the GTAW process was mainly driven by the arc shear stress. Meng's studies suggested that in the GTAW process, the arc shear stress is the dominant force for the backward flow of the liquid metal, which masks the effect of Marangoni force [36-38]. However, in the KPAW process, the arc pressure is much high, which also has great influences on the fluid flow.

The Marangoni force has minor influence on the fluid flow in the KPAW process, which is different from the previous studies of the GTAW process. The Marangoni force is calculated by Eq. (2.11):

$$F_M = \frac{\partial \gamma}{\partial T}\frac{\partial T}{\partial r} \tag{2.11}$$

Where $\partial\gamma/\partial r$ is the surface tension gradient (-0.00043 N/m·K), $\partial T/\partial r$ is the temperature gradient.

At the rear part of the weld pool, the maximum temperature (1859 K) is located at the weld pool center, and the minimum temperature (1727K) is located at the weld pool edge, so the average Marangoni force in longitudinal direction is about 6 Pa.

Here, the dominant driven forces for energy transportation in the KPAW and GTAW processes can be concluded. Due to the much high arc pressure and plasma shear stress, the energy can be easily transported in the vertical and horizontal directions, so a weld pool with large weld depth and weld length is obtained in the KPAW process. For simplification, it is assumed that the energy absorbed by the weld pool in the KPAW process is same to that in the GTAW process. Based on Eq. (2.12), the volume of the weld pool in the KPAW process is much larger than that in the GTAW process, so the average temperature of the weld pool in the KPAW process is lower.

$$1427\,\rho V_1 \mathrm{C_S} + \rho V_1 H_f + \rho V_1 \mathrm{C_L} \bullet (T_1 - 1727) = 1427\,\rho V_2 \mathrm{C_S} + \rho V_2 H_f + \rho V_2 \mathrm{C}_L \bullet (T_2 - 1727) \tag{2.12}$$

Where V_1 and V_2 is the volume of the weld pool in the KPAW process and GTAW process, respectively, T_1 and T_2 is the average temperature of the weld pool in the KPAW process and GTAW process, respectively, C_S, C_L is specific heat of the solid and liquid phase, respectively. H_f is the latent heat of fusion.

In summary, the much high arc pressure and plasma shear stress promote the fluid flow and energy transportation in the vertical and horizontal directions, such that a large weld pool is formed in the KPAW process, leading to the low temperature distribution in the weld pool.

2.4.1.2 After the penetrated keyhole formation

The penetrated keyhole is formed at about 2.8s. At t=3.6 s, it can be seen from **Fig. 2.13** that the front keyhole wall is very thin. The keyhole width at the top is much higher than that at the bottom. The temperature of the molten metal near the keyhole is the highest. At the top surface of the weld pool, the molten metal flows upward and backward due to the reverse flow of the plasma. A clockwise eddy is formed inside the top weld pool. At the bottom surface of the weld pool, the molten metal flows downward and backward due to the arc pressure and the downward flow of plasma. An anti-clockwise eddy is formed inside the bottom weld pool.

It should be noted that the average velocity of the molten metal at the top surface of the weld pool is decreased after the penetrated keyhole formation. Before the penetrated keyhole formation, as shown in **Fig. 2.9**, the average velocity at the top surface of the weld pool is about 0.3 m/s. After the penetrated keyhole formation, as shown in **Fig. 2.13**, the average velocity at the top surface of the weld pool is about 0.10 m/s. This is because all the arc plasma flows upward and outward before the penetrated keyhole formation. However, most of the arc plasma flows downward, and the reverse flow is weak after the penetrated keyhole formation.

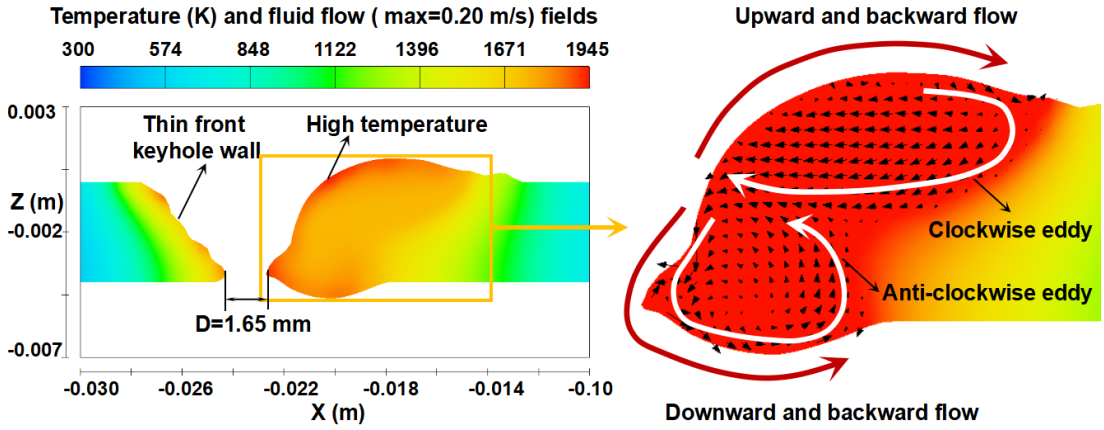

Fig. 13 Temperature (K) and fluid flow fields of y=0 cross sectional view at t= 3.6 s

The similar convective patterns can be seen in the high speed x-ray results. As shown in **Fig. 2.14**, the clockwise eddy and anti-clockwise eddy can be observed at the top and bottom parts of the weld pool, respectively. The maximum velocity (0.32 m/s) is located at the convective pattern near the bottom surface. Because the plasma flows downward near the keyhole with high velocity, and the top surface is far away from the arc center, but the bottom surface is closer to the arc center, so the plasma shear stress is higher near

the bottom surface. Besides, the arc pressure near the bottom surface is also higher. All of these reasons contribute to the higher fluid flow velocity near the bottom surface.

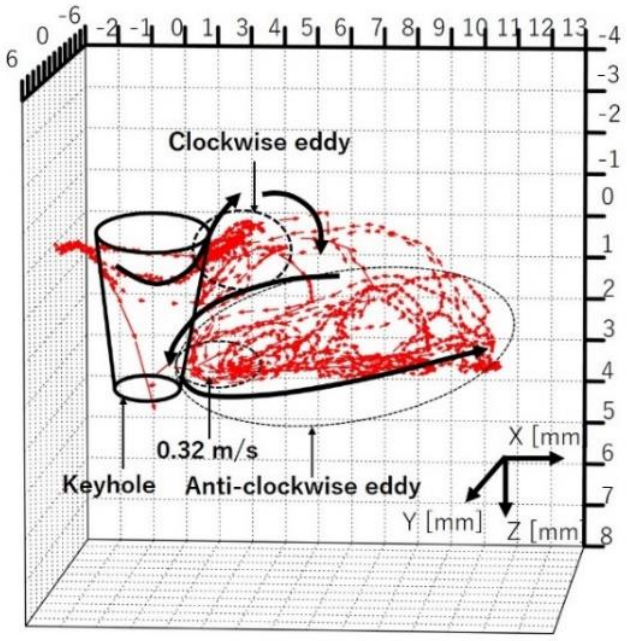

Fig. 2.14 Three dimensional convective patterns inside the weld pool based on the high speed x-ray results [35]

The convective patterns on the top and bottom surfaces are also obtained by tracing the movement of Zirconia particles on the weld pool surfaces. As shown in **Fig. 2.15(A)**, at the top surface of the weld pool, the molten metal flows backward at the rear part of the weld pool. As shown in **Fig. 2.15(B)**, at the bottom surface of weld pool, the molten metal flows backward.

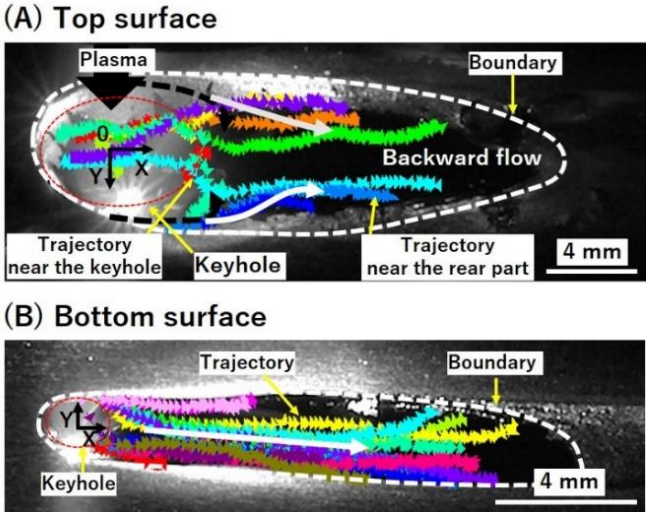

Fig. 2.15 Convective patterns on the weld pool surfaces: (A) Top surface; (B) Bottom surface [35]

The temperature distributions at the top and bottom surfaces are studied based on experiment. As shown in **Fig. 2.16(A)**, at the top surface, a teardrop shaped weld pool is formed. The weld pool width is the widest at the arc center. A high temperature zone can be observed near the keyhole, and the maximum temperature of the weld pool is about 1875K, as shown in **Fig. 2.16(B)**. A teardrop shaped weld pool and a high temperature zone near the keyhole can also be seen at the bottom surface, as shown in **Fig. 2.16(C)** and **(D)**. The weld pool at the top surface is obviously wider than that at the bottom surface.

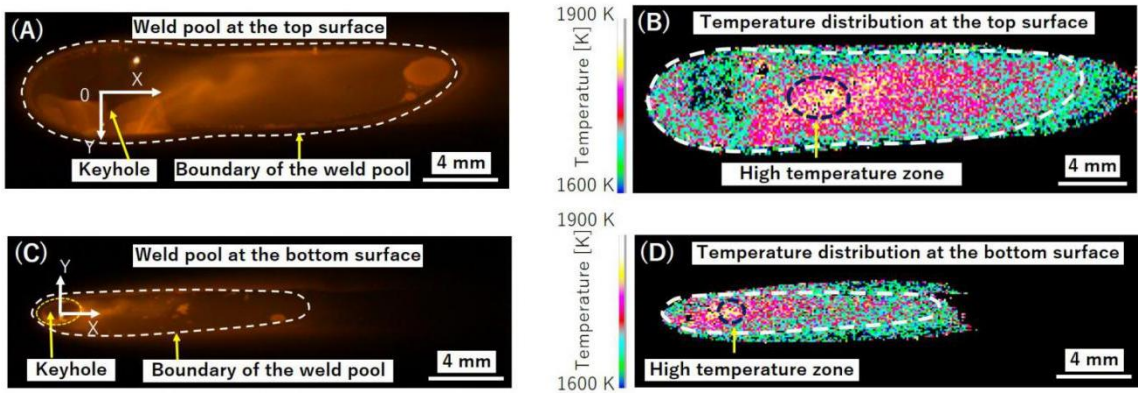

Fig. 16 (A) Weld pool image at the top surface; (B) Temperature distribution of the weld pool at the top surface; (C) Weld pool image at the bottom surface; (D) Temperature distribution of the weld pool at the bottom surface [35]

Due to the strong radiation of the arc, it is difficult to take the weld pool surface images by the thermal camera. In this study, the temperature of the weld pool is measured immediately after switching off the main arc. The main arc completely disappears within 1.0 ms. Yamazaki et al reported that the decrease of the surface temperature was negligible within 2 ms after cutting the arc [20]. However, it should be noted that the molten metal inside the keyhole is very difficult to be obtained by experiment, so the temperature distribution of the weld pool is studied based on numerical simulation. As shown in **Fig. 2.17**, after the penetrated keyhole formation, the molten metal at the front keyhole is very thin, and the temperature is low. At the top surface, a high temperature zone can be observed near the keyhole, but far from the torch axis. As discussed above, the heat transportation by the fluid flow is the dominant mechanism for energy transportation in the KPAW process. Due to the reverse flow of the plasma, the molten metal at the top surface of the keyhole flows upward and backward, causing the energy accumulation and the high temperature zone formation at the top surface.

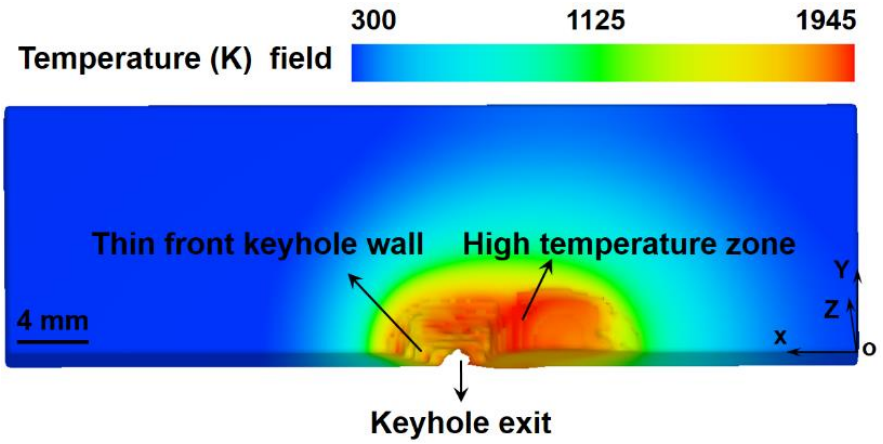

Fig. 2.17 Temperature (K) field of the weld pool at t=3.6 s

2.4.2 Comparison of experiment and numerical simulation

As shown in **Fig. 2.18**, under the influence of the Marangoni force, the molten metal near the keyhole flows backward. Under the influence of the arc pressure and Lorentz force, the molten metal near the keyhole flows downward. Under the influence of the plasma shear stress, the molten metal at the top of the weld pool flows upward and backward, and the molten metal at the bottom of the weld pool flows downward and backward. Under the influence of the buoyance force, the molten metal inside the weld pool flows upward. The convective patterns on the weld pool surfaces and inside the weld pool in numerical simulation agree well with those in the experiment [35].

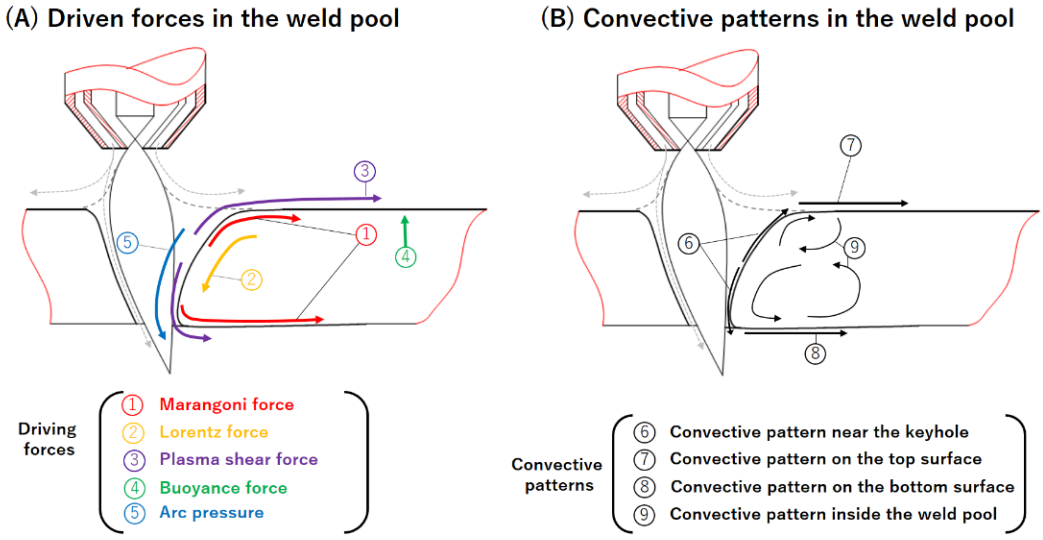

Fig. 2.18 Schematic illustration of the main driven forces and convective patterns of the weld pool

As shown in **Fig. 2.13** and **Fig. 2.16**, the maximum temperature obtained by

numerical simulation is about 1945K, which is similar to that obtained by experiment (about 1875K).

Fig. 2.19 shows the comparison of the calculated and experimental weld profiles at transverse cross section [35]. The weld widths at the top and bottom surfaces, and fusion line obtained by numerical simulation are basically similar to these obtained by the experiment. However, the calculated weld widths (the weld width on the top and bottom surface is 7.2 mm and 3.5 mm, respectively) are larger than the experimental weld widths (the weld width on the top and bottom surface is 6.4 mm and 3.1 mm, respectively), which may be caused by the overestimation of the arc efficiency and underestimation of the heat loss caused by the efflux.

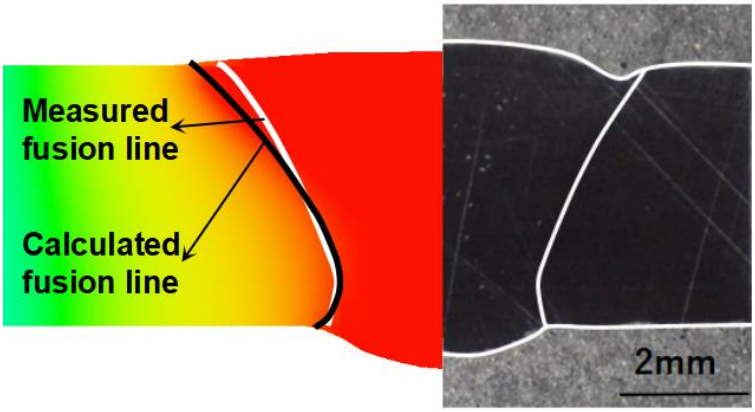

Fig. 2.19 Comparison of calculated and experimental weld profiles at the transverse cross section

2.5 Conclusions

In this study, an electrode-arc model, and a three dimensional weld pool model are developed to investigate the weld pool convection in the keyhole plasma arc welding of stainless steel. The convective patterns inside the weld pool are estimated by a X-ray transmission system. The convective patterns on the weld pool surfaces are measured by a high-speed video camera. The weld pool surface temperature is measured by athermal camera. The conclusions can be summarized as follows:

(1) After the penetrated keyhole formation, at the top surface of the weld pool, the molten metal flows upward and backward due to the reverse flow of plasma. A clockwise

eddy is formed inside the top weld pool. At the bottom surface of the weld pool, the molten metal flows downward and backward due to the downward flow of plasma. An anti-clockwise eddy is formed inside the bottom weld pool.

(2) The much high arc pressure and plasma shear stress promote the fluid flow and energy transportation, such a large weld pool is formed in the KPAW process, leading to the low temperature distribution in the weld pool.

Chapter 3 The keyhole formation mechanisms in the keyhole plasma arc welding process

3.1 Introduction

Numerical simulation provides an effective way to better understand the keyhole formation in the KPAW process. In order to improve the accuracy of numerical results, special treatments on the heat source, arc pressure and plasma shear stress should be considered.

Unlike the GTAW [94] process and GMAW process [95], in the KPAW process, the weld pool deformation is large and a keyhole is formed, so the heat source is keyhole geometry dependent. After the penetrated keyhole formation, both the top and bottom surfaces are heated by the heat source. The efflux plasma from the keyhole exit causes the heat loss. Besides, the keyhole channel is curved backward [81], which also has great effect on the heat source distribution. The combined volume heat source models were used in previous numerical simulation [83-85]. A deviation parameter of the volume heat source center was introduced to considered the thermal effect of the keyhole deviation [101]. However, the time for the open keyhole formation was very short in their numerical simulation. Li [86,102] developed a keyhole dependent surface heat source to investigate the temperature field and fluid flow in the KPAW process, but the special treatments on the heat source after the penetrated keyhole formation was not provided.

Generally, the Gaussian distributed arc pressure was used in previous numerical simulations [82]. The decrease of the arc pressure with the keyhole depth was also considered [28,102]. However, based on Xu's study [93], due to the additional constraint of the keyhole, the arc pressure was increased at the bottom of the keyhole.

In this study, one way coupled electrode-arc-weld pool model is developed to investigate the keyhole formation in the KPAW process. The influence of the backside keyhole deviation on the heat source distribution, the influence of the keyhole constraint on the arc pressure and the keyhole geometry dependent plasma shear stress are considered. A high-speed video camera is used to measure the convective patterns on weld pool surfaces. The keyhole formation mechanism and the influence of material properties on the keyhole formation are revealed.

3.2 Mathematical model and numerical simulation

Firstly, an electrode-arc model is built to investigate the plasma physics in the KPAW process. The numerical result can be seen in **Fig. 3.1**. Some important parameters related to the heat source, arc pressure and plasma shear stress are obtained. The detail information of the model can be seen in our previous work [89]. Based on Jian's study, the maximum mass fraction of the Fe vapor was only 0.24% in the KPAW process, when the welding current was 190 A [103]. The temperature distribution of the weld pool in the KPAW process was measured in our previous work. The maximum temperature was 1795 K when the welding current was 120A [18]. In this study, the relative low welding current (135 A) is used, so the metal vapor is ignored in our electrode-arc model.

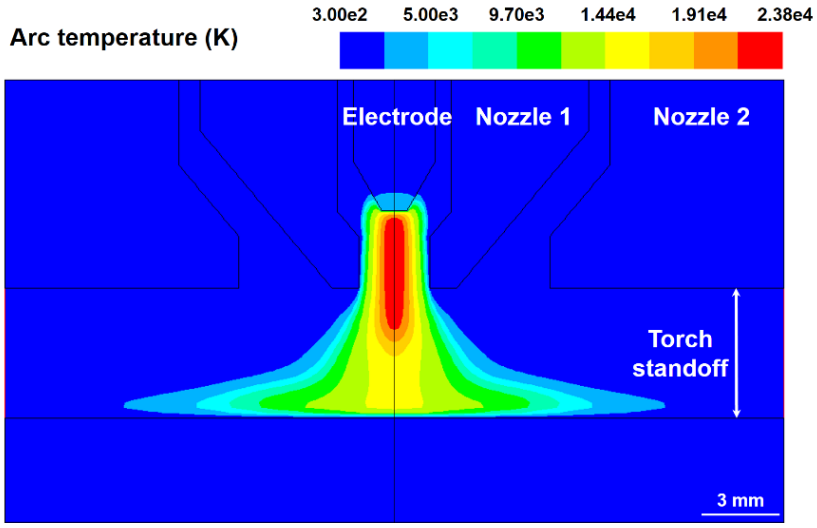

Fig. 3.1 Plasma arc modeling

Then, an improved weld pool numerical model is developed for the KPAW process. The simplification of the mathematic model, the governing equations, surface tension, Lorentz force, buoyancy force and boundary conditions can be found in our previous work [77,90]. In this section, only the special treatments on the heat source, arc pressure and plasma shear stress are discussed.

3.2.1 Self-adaptive heat source model

Before the penetrated keyhole formation, as shown in Eq. (3.1), the heat source is considered as Gaussian distributed. In order to consider the decrease of the heat flux caused by the increase of the arc length, a parameter L_q is introduced in the heat source model [86,102], as shown in Eq. (3.2). A global controlling parameter K_q is introduced to

conserve the total energy absorbed by free surfaces, which is calculated by Eq. (3.3). It should be noted that the origin of the coordinate system locates at the left of the top surface, and the heat source moves along the negative x direction.

$$q(x,y,z)=K_q L_q \frac{3\eta UI}{\pi r_q^2}\exp\left\{-\frac{3(x-vt)^2+3y^2}{r_q^2}\right\} \tag{3.1}$$

$$L_q=(1-\frac{Z_k}{H_b+H_{nb}})^2 \tag{3.2}$$

$$\eta UI=\iint q(x,y,z) \tag{3.3}$$

where *x, y, z* are coordinates, η is arc power efficiency, *U* is the arc voltage, *I* is the welding current, r_q is the effective radius of the heat source, *v* is the welding speed, *t* is the time, Z_k is the distance between the cell center and the top of the base metal, H_b is the thickness of the base metal, H_{nb} is the distance between the nozzle and the top of the base metal.

After the penetrated keyhole formation, when the arc plasma strikes the inclined front keyhole wall, it will be bent toward the rear part of the weld pool. Some part of the arc plasma flows out through the keyhole entrance aperture. The arc plasma is not symmetry along the welding direction. As shown in **Fig. 2**, the arc plasma is wider at the rear part of the weld pool.

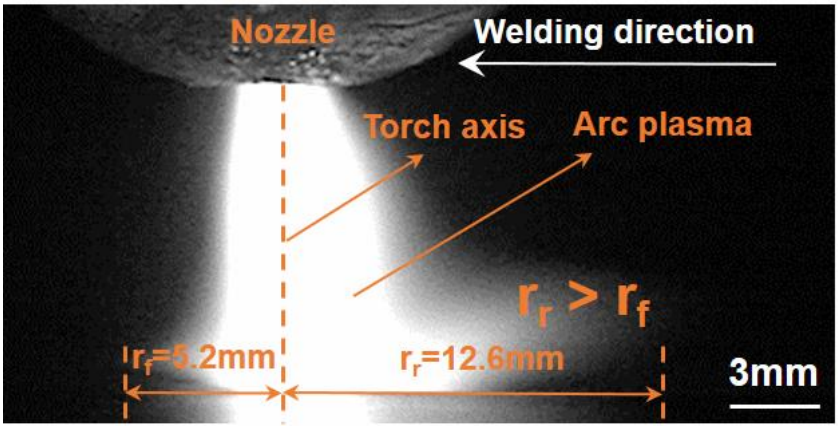

Fig. 3.2 High speed photograph of the plasma arc

As shown in Eq. (3.4), in this study, the heat source after the penetrated keyhole formation is considered as double ellipse distributed. It should be noted that the keyhole

channel is curved backward, and the keyhole exit is deviated from the torch axis, as shown in **Fig. 3.3(A)**. Here, a deviation parameter x_c is introduced to consider the backside keyhole deviation. As shown in **Fig. 3.3(B)**, at the top of the keyhole, x_c is equal to the torch axis location. At the bottom of the keyhole, x_c is equal to the average of the front keyhole and rear keyhole locations. The heat loss (I_1) due to the efflux plasma should also be considered. I_1 is assumed to be equal to the energy absorbed by the virtual free surface at the top of the base metal, as shown in **Fig. 3.3(B)**, and the K_q is calculated by Eq. (3.5).

$$q(x,y,z)=K_q L_q \frac{6\eta UI}{\pi(a_f+a_r)b}\exp\left\{-\frac{3(x-x_c)^2}{a^2}-\frac{3y^2}{b^2}\right\}$$
$$a=\begin{cases}a_f & x<vt\\ a_r & x\geq vt\end{cases} \tag{3.4}$$

$$\eta UI - I_1 = \iint q(x,y,z) \tag{3.5}$$

where a_f, a_r and b are the distribution parameters of the double-ellipse heat source.

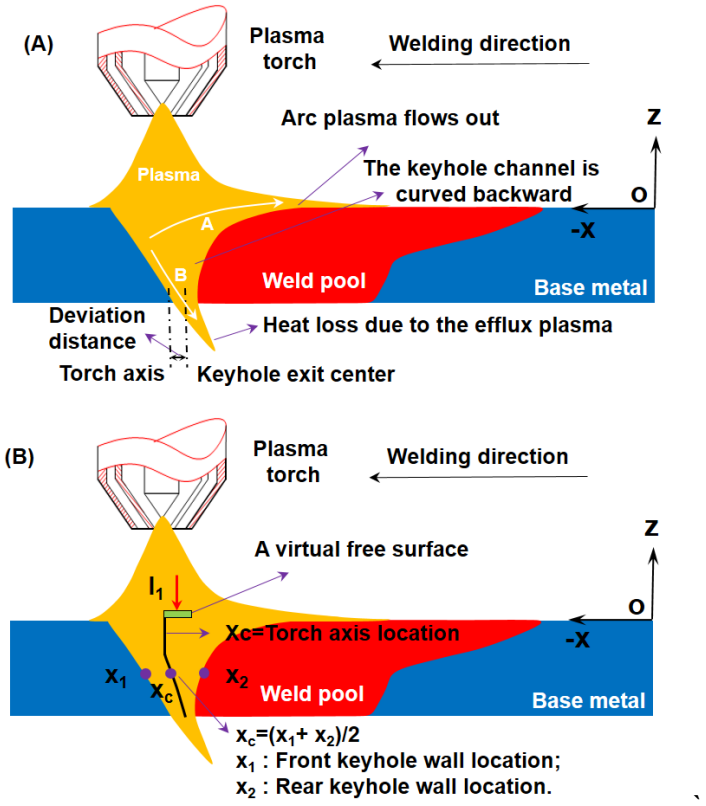

Fig. 3.3 (A) The schematic of the arc plasma-keyhole-weld pool; (B) The calculation of the deviation parameter and heat loss

3.2.2 Arc pressure model

Based on Xu's study, the plasma arc was compressed by the keyhole, which resulted in the increase of the plasma arc pressure. The plasma arc pressure was decreased firstly due to the increase of the arc length, and then increased due to the additional constraint of the keyhole [93]. For simplicity, in this study, from the top to the middle of the base metal, the arc pressure is assumed to be linearly decreased. From the middle to the bottom of the base metal, the arc pressure is assumed to be linearly increased due to the additional constraint of the keyhole. A parameter K_p is introduced to control the variation of the arc pressure. It should be noted that K_p is negative from the top to the middle of the base metal, and is positive from the middle to the bottom of the base metal.

$$p(x,y,z) = (1 + K_p \bullet Z_k)\, p_{max} \exp\left\{-\frac{3(x^2+y^2)}{r_p^2}\right\} \tag{3.6}$$

where P_{max} is the maximum arc pressure, r_p is the effective radius of arc pressure, P_{max} and r_p are obtained from numerical results, as shown in **Fig. 3.4**.

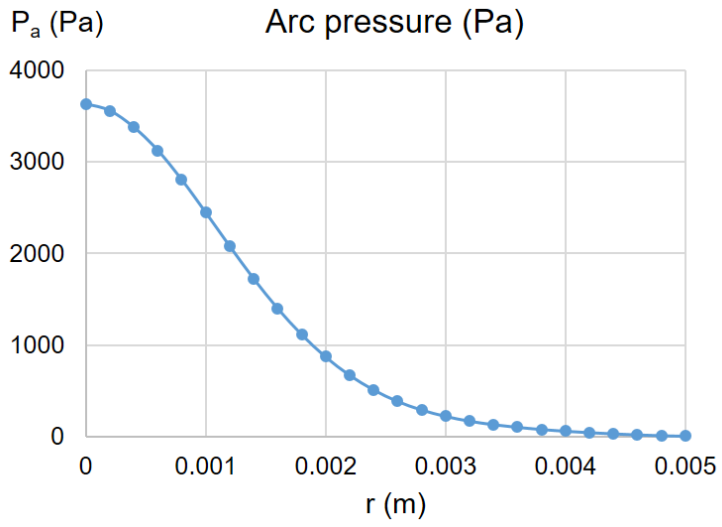

Fig. 3.4 The arc pressure distribution

3.2.3 Shear stress model

Before the penetrated keyhole formation, the arc plasma flows upward and outward along the keyhole wall, as shown in **Fig. 3.5(A)**. The values of the shear stress with different torch standoff are obtained from numerical results, as shown in **Fig. 3.6**. In the

numerical simulation, the plasma shear stress is calculated by Eq. (3.7).

$$\tau(x,y,z)=\begin{Bmatrix}\tau_1 & z\geq -0.001\\ \tau_2 & -0.001>z\geq -0.002\\ \tau_3 & -0.002>z\geq -0.003\\ \tau_4 & -0.003>z\geq -0.004\\ \tau_5 & -0.004>z\end{Bmatrix} \tag{3.7}$$

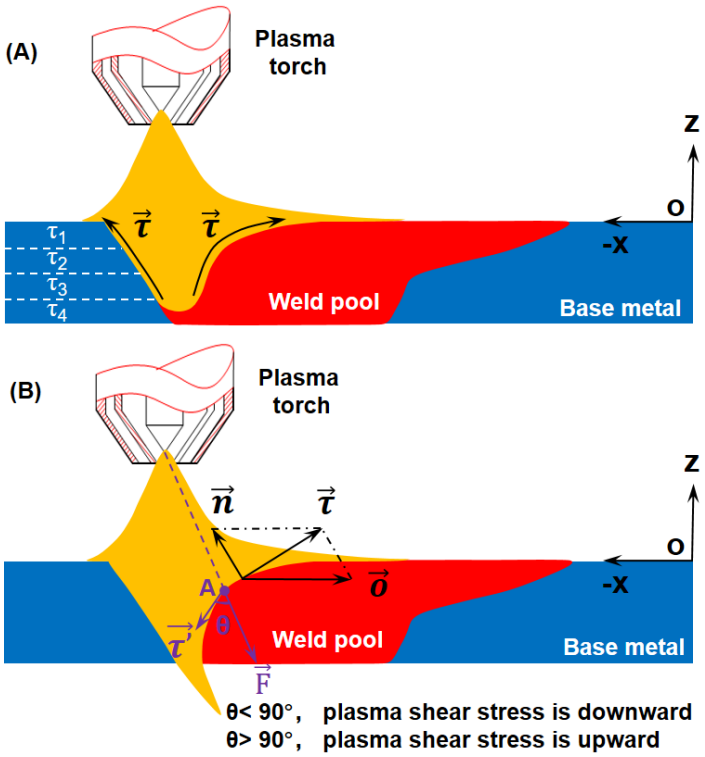

Fig. 3.5 The plasma shear stress model: (A) Before the penetrated keyhole formation; (B) After the penetrated keyhole formation

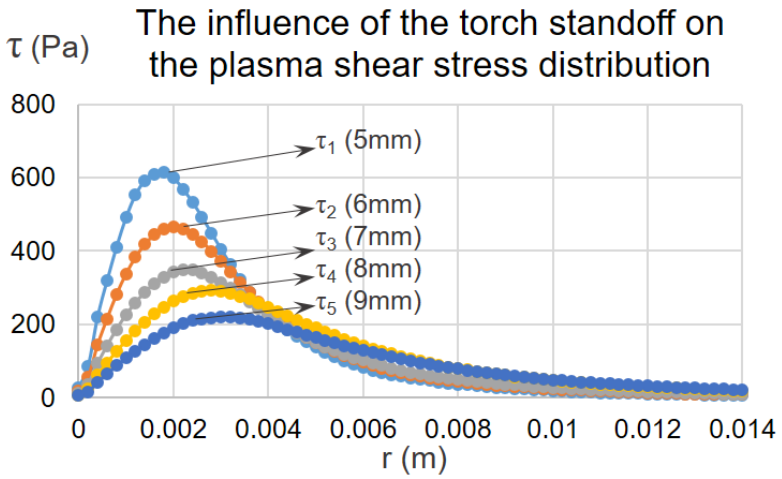

Fig. 3.6 The influence of the torch standoff on the plasma shear stress distribution

After the penetrated keyhole formation, the direction of the plasma shear stress is upward at the top part of the keyhole wall due to the reverse flow of the arc plasma [93], but downward at the bottom part of the keyhole wall. Here, as shown in **Fig. 3.5(B)**, a simple model is developed to determine the plasma shear stress direction at the keyhole wall. It is assumed that the arc plasma flows directly from the torch orifice to the point A at the keyhole wall, and the plasma shear stress direction is downward. The angle (θ) between the virtual plasma flow direction and the virtual plasma shear stress direction is used. If θ is less than 90° ,the plasma shear stress at the point A is downward. Otherwise, it is upward.

At the top part of the keyhole wall, the value of the plasma shear stress caused by the reverse flow can be expressed as below:

$$\tau(x,y,z) = \alpha_{top}\tau \tag{3.8}$$

where α_{top} is a real number.

At the bottom part of the keyhole wall, the plasma velocity is relatively low, and the value of the plasma shear stress can be expressed as below:

$$\tau(x,y,z) = \frac{8\rho_{Ar}U_0^2}{\mathrm{Re}} \tag{3.9}$$

where ρ_{Ar} is the density of argon shielding gas, U_0 is the average plasma jet speed inside the keyhole after penetration, *Re* is the Reynolds number of plasma inside the keyhole after penetration.

It should be noted that Eq. (3.10) is used to determine the value of the plasma shear stress induced at the cylindrical keyhole walls by the vapor [97]. However, the shape of the keyhole in the PKAW process is in dynamically changing, so it is important to calculate the shear stress vector at each free surface cell. As shown in **Fig. 3.5(B)**, before the free surface deformation, the direction of the shear stress is horizontal. After the free surface deformation, the shear stress is redirected. It is assumed that the horizontal vector $\vec{o}$, redirected shear stress vector $\vec{\tau}$, and free surface normal vector $\vec{n}$ are coplanar, so the

redirected plasma shear stress vector can be determined as [104]:

$$\begin{cases} \vec{\tau} \cdot \vec{n} = 0 \\ |\vec{\tau}| = \tau(x, y, z) \\ \vec{\tau} = A\vec{o} + B\vec{n} \end{cases} \tag{3.10}$$

where A and B are real numbers.

3.2.4 Numerical simulation

The commercial CFD (Computational Fluid Dynamics) software FLOW3D is used to solve the governing equations and VOF equation. The finite volume method is applied to discrete the governing equations. Due to the symmetry, half of the computational domain is used in the actual calculation, which is 50 mm in length (x-axis), 20 mm in width (y-axis), and 10 mm in thickness (z-axis). The plate thickness is 4 mm, and the other parts are void region. The mesh size is 0.2mm. The origin of z-axis locates at the top surface of the plate. The details of the iteration scheme can be found in our previous work [91].

The thermo-physical material properties of SUS304 stainless steel can be seen in **Table 3.1**. In our previous studies [105], the temperature dependent surface tension was used, and the numerical results agreed well with the experimental results. So in this study, only the influence of the temperature on the surface tension is considered.

Table 3.1. Thermo-physical material properties of SUS304 stainless steel

Nomenclature	Value	Nomenclature	Value
Density (kg/m^3)	6900	Liquidus temperature(K)	1727
Viscosity (kg/m·s)	0.0059	Solidus temperature	1697
Specific heat (l) (J/kg·K)	720	Boiling temperature(K)	3133
Specific heat (s) (J/kg·K)	760	Heat transfer coefficient (W/m^2·K^4)	20
Latent heat of fusion(J/kg)	2.47×10^5	Coefficient of thermal expansion(K^{-1})	1.5×10^{-4}
Thermal conductivity (l) (W/m·K)	28.4	Surface tension(N/m)	1.8
Thermal conductivity (s) (W/m·K)	33.2	Surface tension gradient(N/m·K)	-0.00043

3.3 Experimental method

The welding experiment setup can be seen in **Fig. 3.7**. The welding equipment consists of a transfer-type plasma arc welding torch (100WH, Nippon Steel Welding & Engineering Co., Ltd.) and a welding power source (NW-300ASR, Nippon Steel Welding & Engineering Co., Ltd.). The base metal used in the experiments is the stainless steel SUS304 plate with a dimension of 300 mm x 100 mm x 4 mm. The torch orifice with a

diameter of 2.8 mm is used in the experiments. The electrode with a diameter of 3.2 mm and tip radius of 0.5 mm is used. The electrode setback is 3 mm. The distance between the nozzle and the base metal is 5 mm. The welding speed is 3 mm/s. The pure Ar is used as the main plasma gas and the shielding gas. In order to avoid the oxidation of the weld bead as far as possible, a back-shielding gas box is put on the welding jig. The main plasma gas flow rate is 2.6 l/min. The shielding gas flow rate is 15 l/min, and the back shielding gas flow rate is 10 l/min. The main current is DC135 A. The same welding parameters are used in the numerical simulation.

In order to measure the convective pattern on the weld pool surface, the Zirconia particles with a diameter of 0.03 mm are put into the small holes on the top surface of the base metal. During the welding, a high-speed video camera (HSVC) is used to observe the movement of Zirconia particles on the weld pool surface. A band pass filter with the wavelength of 500 nm and bandwidth of 10 nm is attached in the front of the HSVC. The frequency is 3000 frame/s.

In order to investigate the evolution of the keyhole depth, the plasma arc is cut off during the welding. This method called “Sudden Stop Test” is used in previous study to investigate the evolution of the front keyhole wall [54]. After the welding, the weld length and keyhole depth are measured. After several trials, the relationship between the weld length and keyhole depth can be obtained.

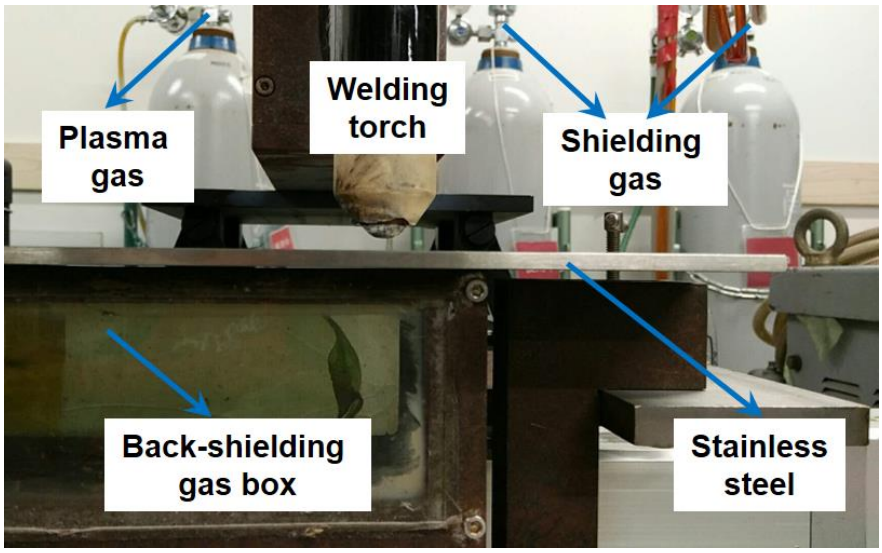

Fig. 3.7 The welding experiment setup

3.4 Results and discussion

It can be seen that from **Fig. 3.8** that the keyhole depth increases very quickly at first,

then smoothly, and then quickly again. In this study, the process between the weld pool formation and weld pool penetration is defined as the blind keyhole stage. The process between the weld pool penetration and keyhole penetration is defined as the blasting penetration stage, and the duration of this process is defined as the blasting time. The process after the keyhole penetration is defined as the penetrated keyhole stage. The weld pool convection and keyhole depth evolution in these stages are discussed.

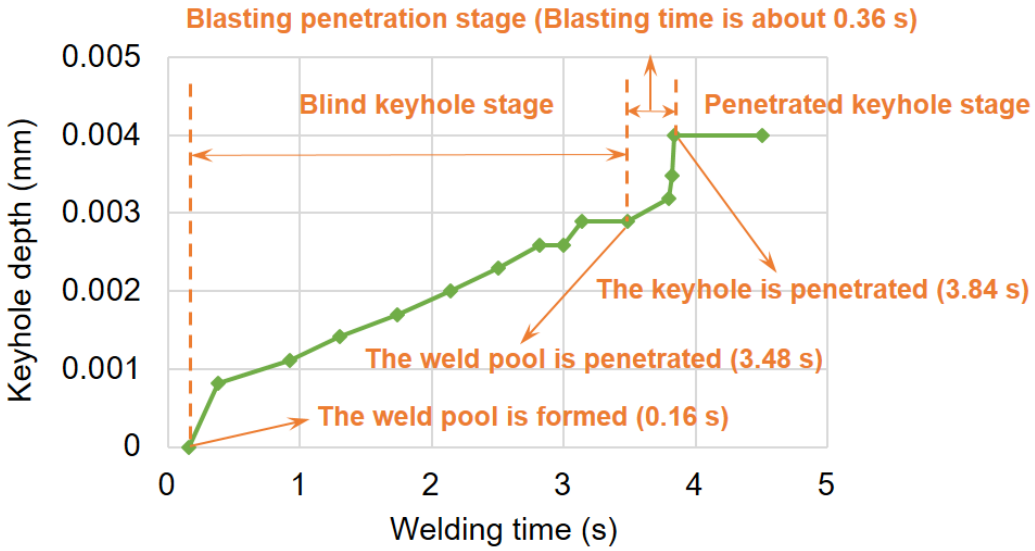

Fig. 3.8 Keyhole depth evolution in the simulation

3.4.1 Blind keyhole stage

Fig. 3.9 shows the temperature and fluid flow fields of y=0 cross sectional view. It can be seen that at the beginning of the welding, the weld pool surface is deformed under the influence of the arc pressure and plasma shear stress. The molten metal under the arc flows outward, and a swelling is formed at the rear part of the weld pool. At t =1.7 s, a deep keyhole is formed, and the molten metal flows backward along the rear keyhole wall. Two convective eddies exist inside the weld pool. The anti-clockwise eddy near the arc center is caused by the arc pressure and Lorenz force, and the clockwise eddy at the rear part of the weld pool is caused by the plasma shear stress and Marangoni force. The size of the latter eddy is larger. At t =3.48 s, the weld pool is penetrated, while the keyhole depth is only 2.89 mm. The size of the anti-clockwise eddy becomes larger.

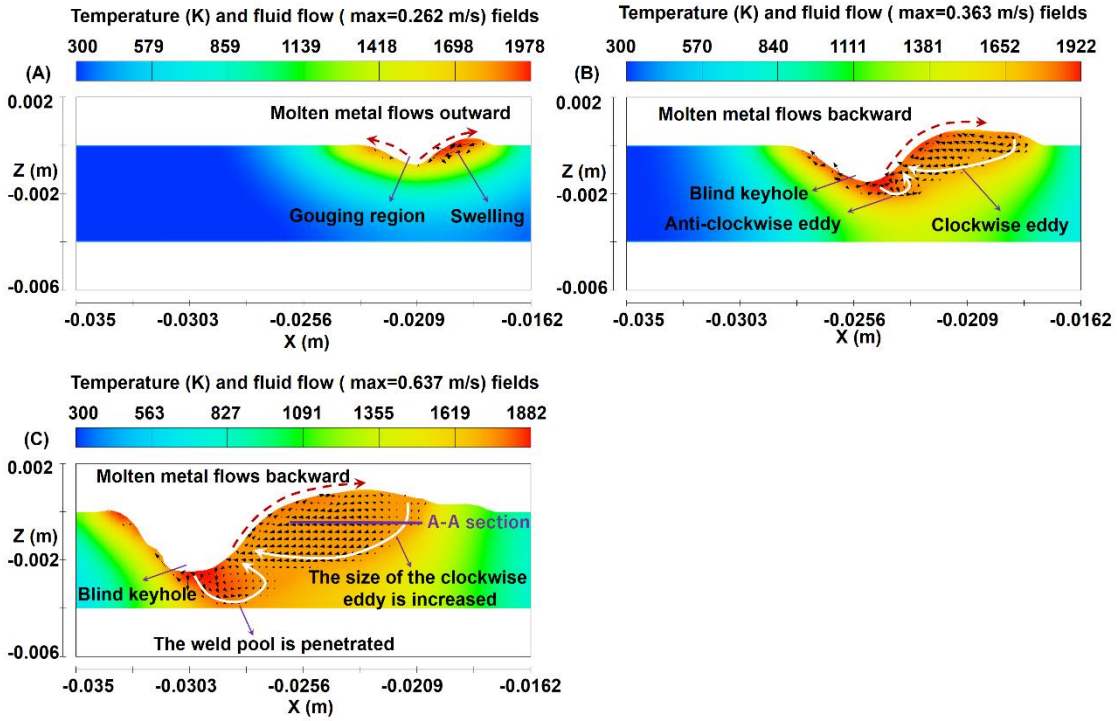

Fig. 3.9 Temperature (K) and fluid flow fields of y=0 cross sectional view at: (A) t = 0.42 s; (B) t = 1.7 s; (B) t = 3.48 s

Fig. 3.10 shows the temperature and fluid flow fields of different cross sectional views at t = 3.48 s. It can be seen that near the keyhole center, the convection pattern on the top surface is similar to that in **Fig. 3.9**, and the forward flow can be observed inside the weld pool. Near the weld pool edge, the molten metal on the top surface and inside the weld pool flows backward to the rear part of the weld pool.

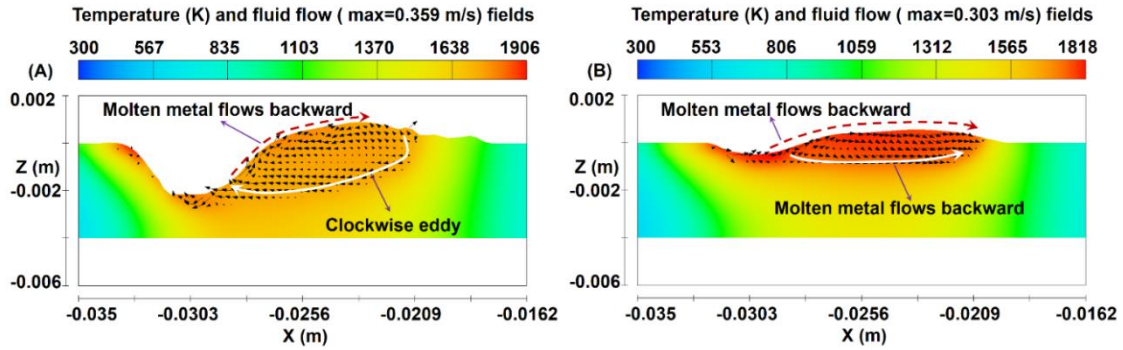

Fig. 3.10 Temperature (K) and fluid flow fields at t = 3.48 s: (A) y= 0.001 mm cross sectional view; (B) y= 0.003 mm cross sectional view

Fig. 3.11 shows the temperature and fluid flow fields at the A-A section in **Fig.9 (C)**. It can be seen that at the lateral sides of the keyhole, the molten metal flows outward and backward with high momentum. When the molten metal reaches the weld

pool edge, it will change the flow direction, causing the forward flow.

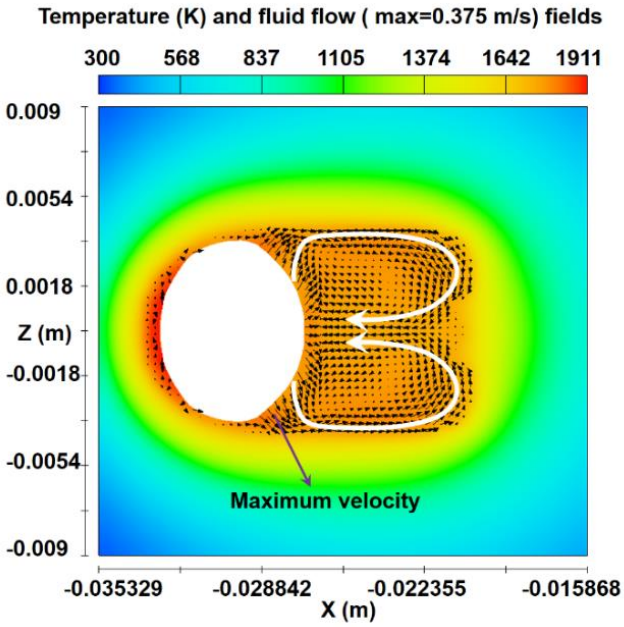

Fig. 3.11 Temperature (K) and fluid flow fields of A-A sectional view at t = 3.48 s (z=0.0002mm section)

The weld pool convection in the three dimensional view in the blind keyhole stage can be summarized as **Fig. 3.12**. The molten metal flows outward and backward along the rear keyhole wall. Two contrary convective eddies can be found at the top and bottom parts of the weld pool.

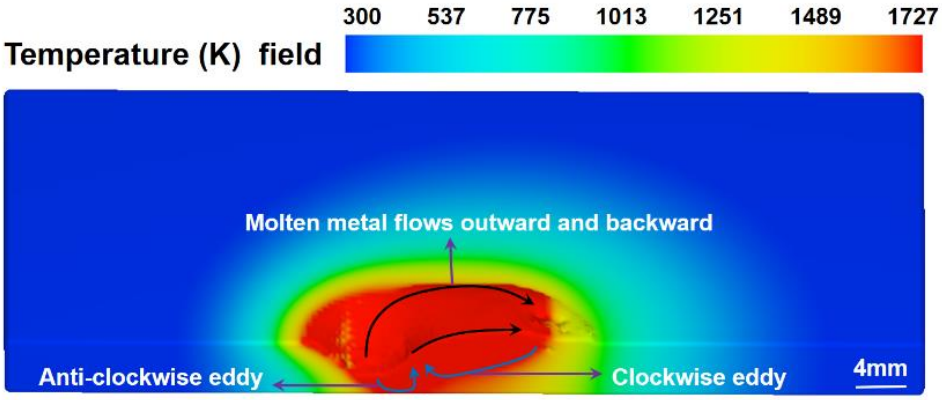

Fig. 12 Three dimensional temperature (K) field of the weld pool at t = 3.48 s

It can be obviously seen from **Fig. 3.9** that the weld pool depth is larger than the keyhole depth. The same conclusion can also be obtained from the experiment. As shown in **Fig. 3.13**, when the low plasma gas rate is used (2.0 L/min), only a blind keyhole is formed in the experiment, but the weld pool is penetrated, and the bottom surface is largely deformed.

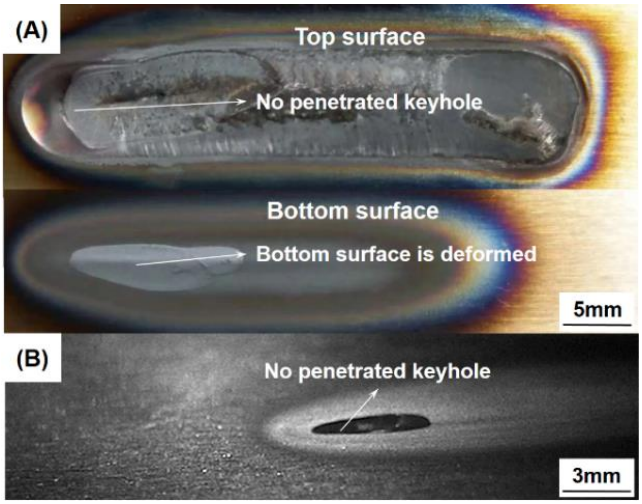

Fig. 3.13 Weld bead formation with low plasma gas rate (2.0 L/min): (A) Top surface; (B) Bottom surface; (C) The high speed photography of the bottom surface

In order to explain this phenomenon, the simulations with large arc pressure or large plasma shear stress are restarted at t = 2 s. As shown in **Fig. 3.14**, when the arc pressure is doubled, at t = 2.1 s, the molten metal layer under the arc is very thin, and the keyhole depth is almost same to the weld depth. At t = 2.2 s, the keyhole becomes deep, and the depth to width ratio of the keyhole bottom is about 2.96. It should be noted that the anti-clockwise eddy is disappeared, and only a clockwise eddy exists inside the weld pool. At t = 2.54 s, the keyhole is penetrated.

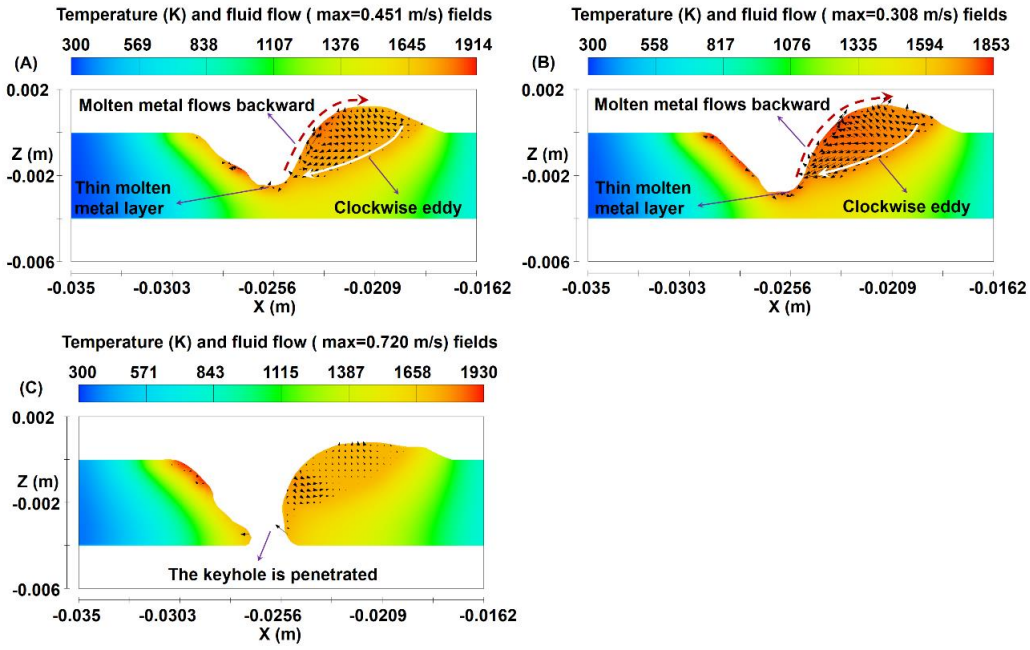

Fig. 3.14 Temperature (K) and fluid flow fields of y=0 cross sectional view at: (A) t = 2.1 s; (B) t = 2.2 s; (C) t = 2.54 s (The simulation is restarted at t = 2s with double arc pressure)

As shown in **Fig. 3.15**, when the plasma shear stress is doubled, at t = 2.1 s, the keyhole depth is also almost same to the weld depth. At t = 2.2 s, the keyhole becomes deep and only a clockwise eddy exists inside the weld pool. The depth to width ratio of the keyhole bottom is about 1.62. At t = 2.7 s, the keyhole is penetrated. Based on the above discussion, it can be concluded that the arc pressure and plasma shear stress are not large enough to push the molten metal under the arc to the rear part of the weld pool, so the weld pool depth is larger than the keyhole depth.

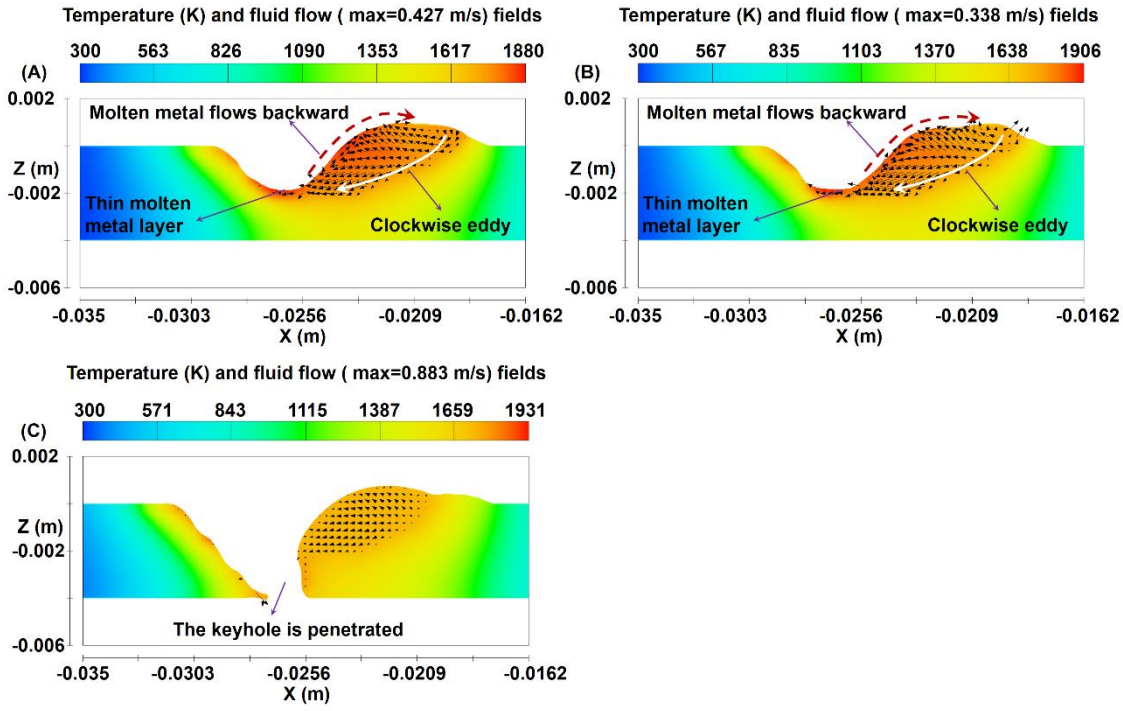

Fig. 3.15 Temperature (K) and fluid flow fields of y=0 cross sectional view at: (A) t = 2.1 s; (B) t = 2.2 s; (C) t = 2.7 s (The simulation is restarted at t = 2s with double plasma shear stress)

Here, the blind keyhole formation mechanism is concluded. The pressure balance of the blind keyhole bottom in the vertical direction is shown in **Fig. 3.16**. P_{arc} is the arc pressure, which acts to deepen the keyhole. P_σ is the surface tension pressure ($P_\sigma = \sigma / r$; σ is the surface tension. r is the keyhole bottom radius), which acts to shrink the keyhole. P_{re} is the resistant drag force. In this study, the porous media drag model is used to model the flow in the mushy zone in which the temperature of the cell is between the liquidus and solidus temperature [90,91]. At the blind keyhole bottom, the resistant drag force acts on the mushy zone, so the flow is suppressed. The resistant drag force suppresses the keyhole formation.

The arc pressure is larger than the sum of the surface tension pressure and the resistant drag force, so the anti-clockwise eddy is formed, and the energy can be easily transported in the vertical direction. It should be noted that parallel to the rear keyhole wall, the plasma shear stress is very large, and the resistant drag force for the fluid flow is very small. So the molten metal flows backward easily along the rear keyhole wall, and the depth to width ratio of the keyhole is decreased. These conclusions can be verified by **Fig. 3.14** and **Fig. 3.15**. Even though the arc pressure is doubled, the molten metal still flows backward along the rear keyhole wall. When the plasma shear stress is doubled, the depth to width ratio of the keyhole bottom becomes smaller. In summary, the arc pressure deepens the keyhole. The plasma shear stress facilitates the fluid flow along the rear keyhole wall and decreases the curvature of the keyhole. All of these reasons contribute to the formation and depth increase of the blind keyhole.

Which force is more dominant for keyhole formation? In **Chapter 2**, in the normal case, the keyhole depth is about 3.2 mm at t=2.5 s. Without the arc shear stress and arc pressure, the keyhole is not formed. Without the arc pressure, a shallow blind keyhole is formed at t=2.5s, and the keyhole depth is about 1.1 mm. Without the arc shear stress, a deep blind keyhole is formed at t=2.5s, and the keyhole depth is about 2.9 mm. It can be concluded that the arc pressure has greater influences on the keyhole formation than the plasma shear stress.

In the blind keyhole stage, the relationship between the keyhole depth and time can be explained as follow. As shown in **Fig. 3.16**, at the beginning of the welding, the weld pool deformation is small, so the surface tension pressure is small. The arc pressure is much higher than the sum of the surface tension pressure and the resistant drag force, and the plasma shear stress is also very large, so the keyhole depth increases very quickly. When keyhole depth is large enough, the surface tension pressure is increased and the plasma shear stress is decreased, so the keyhole depth increases smoothly.

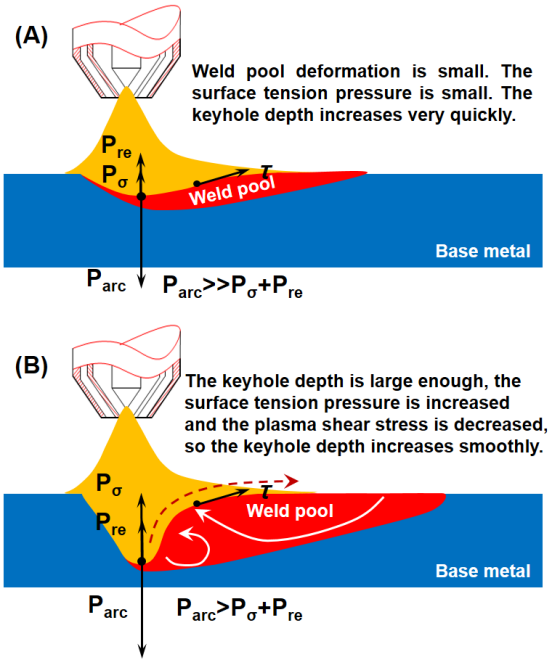

Fig. 3.16 The pressure balance of the blind keyhole bottom in the vertical direction: (A) The weld pool deformation is small; (B) A deep keyhole is formed

3.4.2 Blasting penetration stage

As shown in **Fig. 3.17(A)**. The molten metal under the arc center is defined as the molten bridge. Even though the weld pool is penetrated, at the bottom surface, some solid metals still exist near the arc center. Based on the pressure balance of the molten bridge, P_{arc} acts to break the molten bridge. P_{σ} and P_{re} act to keep the molten bridge. At the beginning of the blasting penetration stage, the molten metal on the bottom surface is few, and the mushy zone is large, so P_{re} is large. As shown in **Fig. 3.17(B), (C)** and **(D)**, more energy is transported in the vertical direction. The size of the anti-clockwise eddy inside the weld pool is increased, and the molten metal on the bottom surface becomes more and more. Even though the keyhole bottom radius becomes smaller, and P_{σ} becomes larger, but P_{re} is very small. The thickness of the molten bridge becomes smaller and smaller, and it will be broken soon. The blasting time is about 0.36 s (3.48s ~ 3.84s).

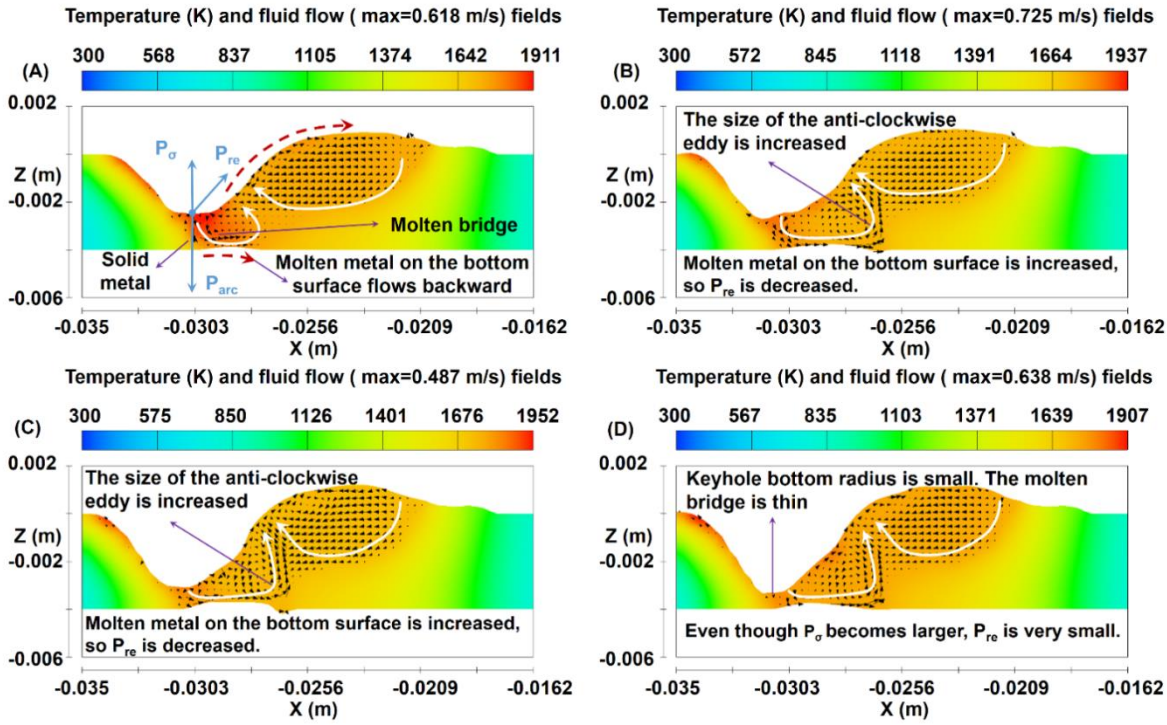

Fig. 3.17 Temperature (K) and fluid flow fields of y=0 cross sectional view at: (A) t = 3.56 s; (B) t = 3.76 s; (C) t = 3.80 s; (D) t = 3.82 s

As shown in **Fig. 3.18**, before the weld pool penetration, the average maximum velocity of the weld pool is only 0.375 m/s. After the weld pool penetration, the maximum velocity becomes very high, and the average maximum velocity is 0.586 m/s.

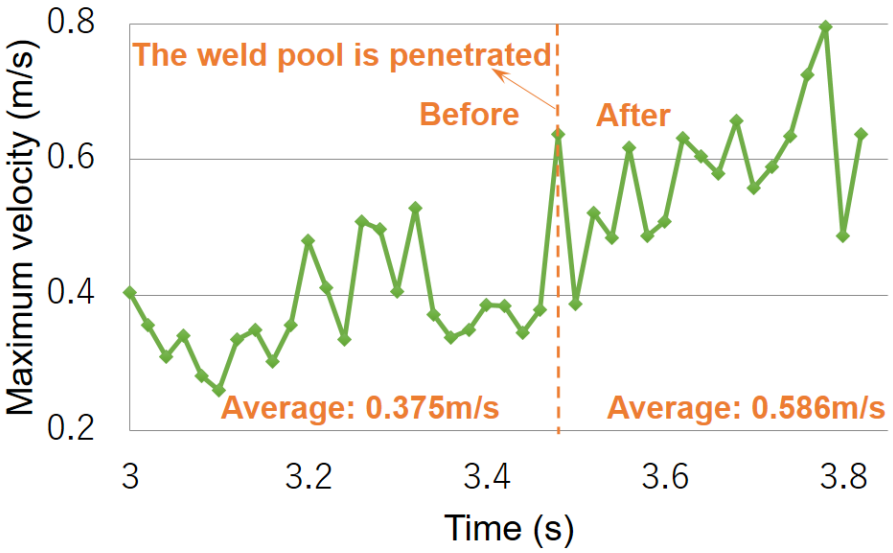

Fig. 18 The maximum velocity of the weld pool vs time

Before the weld pool penetration, the molten metal flows backward along the rear keyhole wall. After the weld pool penetration, as shown in **Fig. 3.17(A)**, the molten metal

flows backward along the rear keyhole wall and the bottom surface with higher velocity. As shown in **Fig. 3.19**, after the weld pool penetration, the outflow velocity of the molten metal in the molten bridge is much larger than the inflow velocity. Based on the mass conservation, the thickness of the molten bridge becomes smaller and smaller quickly.

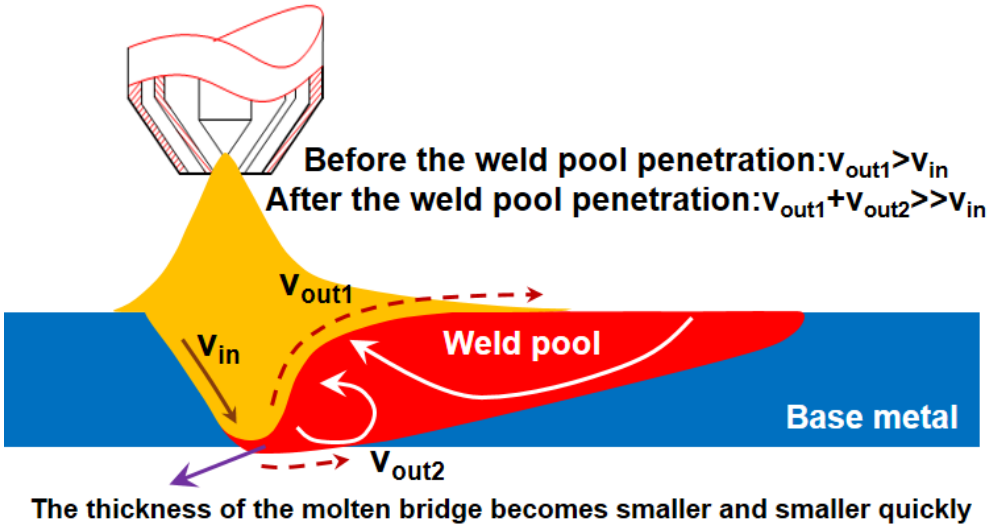

Fig. 3.19 Mass conservation mechanism contributes to the blasting penetration

In summary, both the pressure balance and mass conservation mechanisms are proposed to be responsible for the blasting penetration. After the weld pool penetration, the arc pressure is much larger than the sum of the surface tension pressure and resistant drag force. The outflow velocity of the molten metal in the molten bridge is much larger than the inflow velocity. All of these reasons contribute to the break of the molten bridge.

Here some simulations are carried out to verify the proposed mechanisms. Based on the pressure balance mechanism, the decrease of the resistant drag force plays an important role on the break of the molten bridge. The simulation with low melting temperature (1200 K) is restarted at t = 3.48 s. It can be seen from **Fig. 3.20(A)** that a lot of fluid in the mushy zone in the normal case becomes liquid metal, because its temperature is larger than 1200 K. So the resistant drag force on the molten bridge is very small, and the arc pressure is much larger than the surface tension pressure. In **Fig. 3.20(B)**, a deep keyhole is formed and the maximum velocity is 0.469 m/s. The molten bridge is thin. In **Fig. 3.20(C)**, the keyhole is penetrated. The blasting time is only 0.009 s.

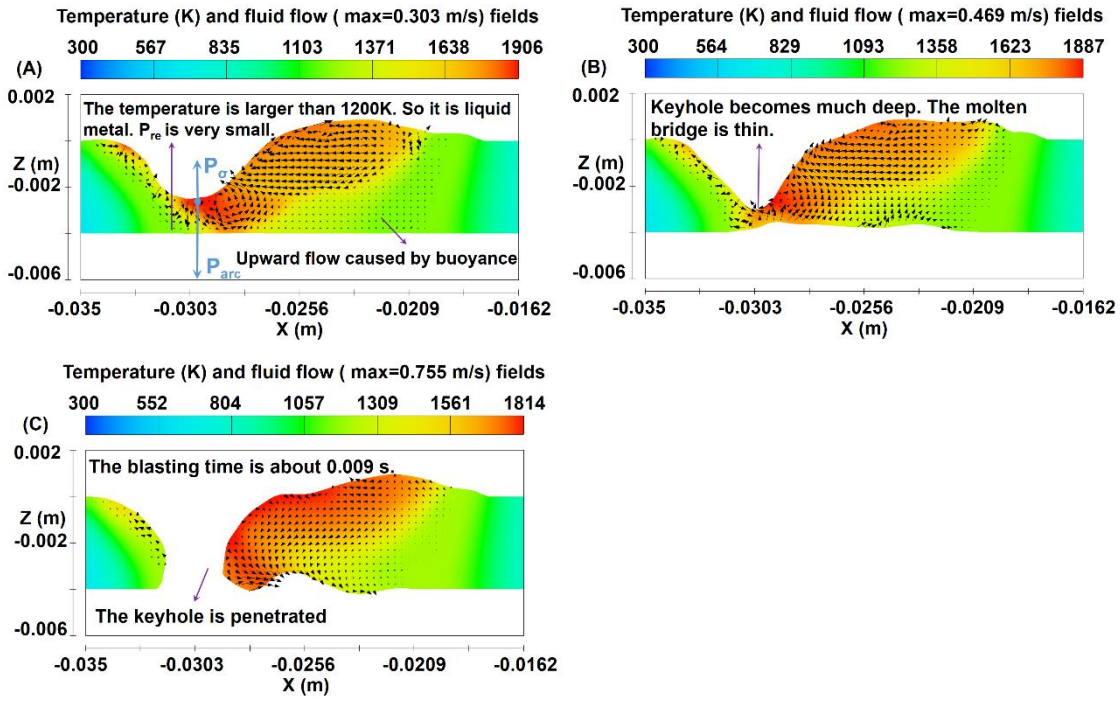

Fig. 3.20 Temperature (K) and fluid flow fields of y=0 cross sectional view at: (A) t = 3.481 s; (B) t = 3.484 s; (C) t = 3.489 s (Simulation with low melting temperature)

Based on the pressure balance mechanism, the decrease of the surface tension pressure facilitates the break of the molten bridge. The simulation with low surface tension (0.87 N/m) is restarted at t = 3.48 s. As shown in **Fig. 3.21(A)**, even though the keyhole bottom radius is small, but the surface tension is small. The surface tension pressure is small, and the arc pressure is much larger than the sum of the surface tension pressure and reaction force. As shown in **Fig. 3.21(B)**, the keyhole depth becomes much deep, and the maximum velocity is 0.568 m/s. The molten bridge is very thin. As shown in **Fig. 3.21(C)**, the keyhole is penetrated, and the blasting time is only 0.08 s.

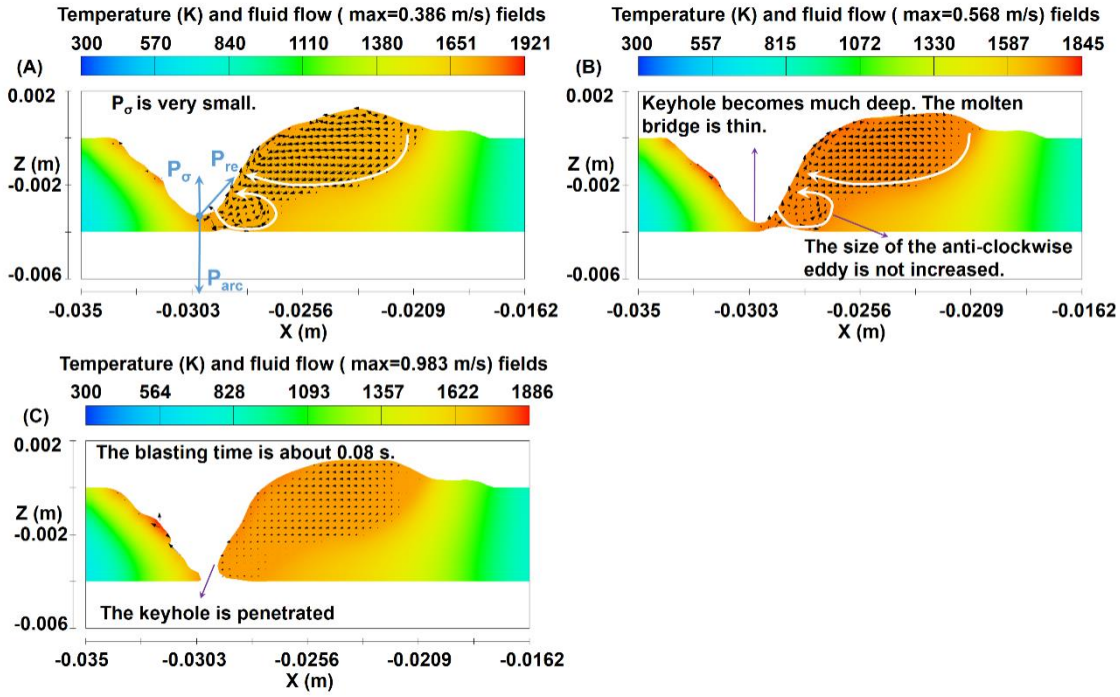

Fig. 3.21 Temperature (K) and fluid flow fields of y=0 cross sectional view at: (A) t = 3.52 s; (B) t = 3.54 s; (C) t = 3.56 s (Simulation with low surface tension)

Based on the mass conservation mechanism, the increase of the outflow velocity in the molten bridge plays an important role on the break of the molten bridge. After the weld pool penetration, the backward flow along the rear keyhole wall is mainly caused by the plasma shear stress, and the backward flow along the bottom surface is mainly caused by the arc pressure. The simulation without the plasma shear stress is restarted at t = 3.48 s. As shown in **Fig. 3.22(A)**, the molten metal on the bottom surface flows backward with high velocity, and the flow of the anti-clockwise eddy becomes strong. It can also be seen that without the plasma shear stress, the molten metal flows to the molten bridge along the rear keyhole wall, and only flows out of the molten bridge along the bottom surface. So the inflow velocity in the molten bridge is high, but the outflow velocity is decreased. As shown in **Fig. 3.22(B)**, at t = 3.84 s, the molten bridge is very thick, and the keyhole depth is stable.

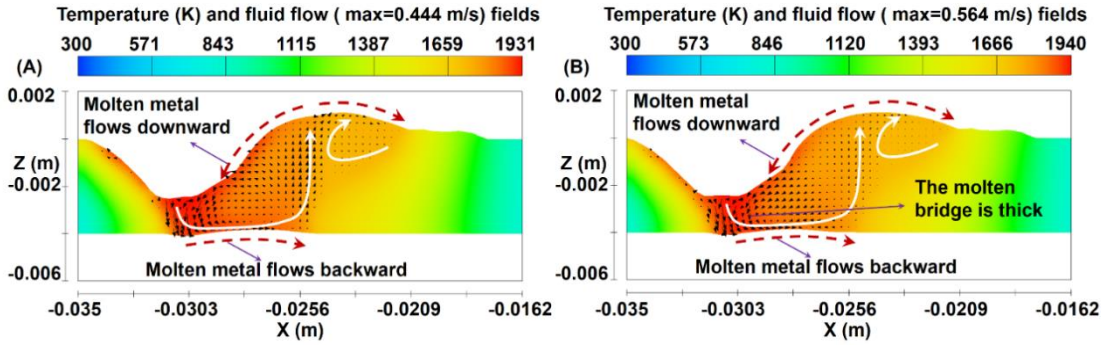

Fig. 3.22 Temperature (K) and fluid flow fields of y=0 cross sectional view at: (A) t = 3.76 s; (B) t = 3.84 s (Simulation without the plasma shear stress)

The simulation with bottom wall boundary is restarted at t = 3.48 s. As shown in **Fig. 3.23(A)**, the bottom surface is not deformed, and the backward flow on the bottom surface is suppressed. As shown in **Fig. 3.23(B)**, at 3.84 s, the flow of the anti-clockwise eddy is weak, and the keyhole depth is stable. The molten bridge is still very thick.

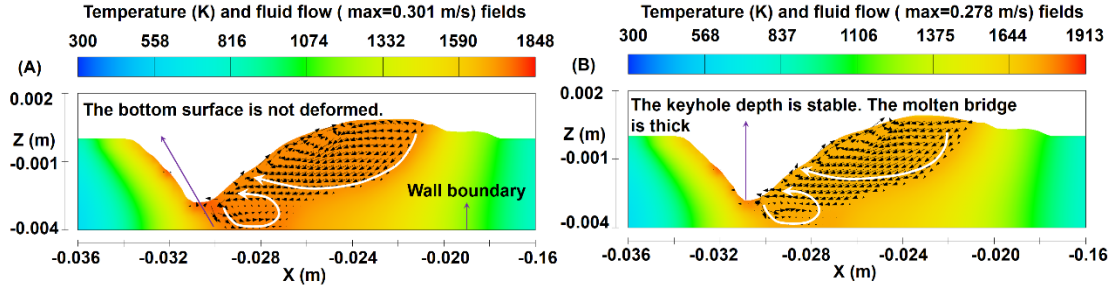

Fig. 3.23 Temperature (K) and fluid flow fields of y=0 cross sectional view at: (A) t = 3.76 s; (B) t = 3.84 s (Simulation with bottom wall boundary)

It should be noted that the pressure balance and mass conservation mechanisms are coupled. When the pressure balance condition is changed, the maximum velocity of the weld pool is also changed, as shown in **Fig. 3.19**, **Fig. 3.20**. If the fluid flow condition is changed, the keyhole shape is change, which also has great influences on the pressure balance condition.

Based on the above simulations, the penetrated keyhole is easily formed in the KPAW process of the material with low melting temperature or low surface tension. However, as is known to all, the keyhole is difficult to form in the variable polarity plasma arc welding (VPPAW) of aluminum alloy. The simulation with aluminum alloy thermal conductivity (Solid thermal conductivity: 235 W/m·K. Fluid thermal conductivity: 90 W/m·K) is restarted at t = 3.48 s. As shown in **Fig. 3.24(A)**, due to the large thermal conductivity, a lot of energy is transported from the weld pool to the solid metal. The weld pool becomes

smaller. As shown in **Fig. 3.24(B)**, the anti-clockwise eddy in the weld pool is disappeared. The bottom part is solidified, and a penetrated keyhole is not formed. It should be noted that the VPPAW of aluminum alloy is a very complex process. The simulation in this study only shows that the material properties have great influences on the keyhole formation.

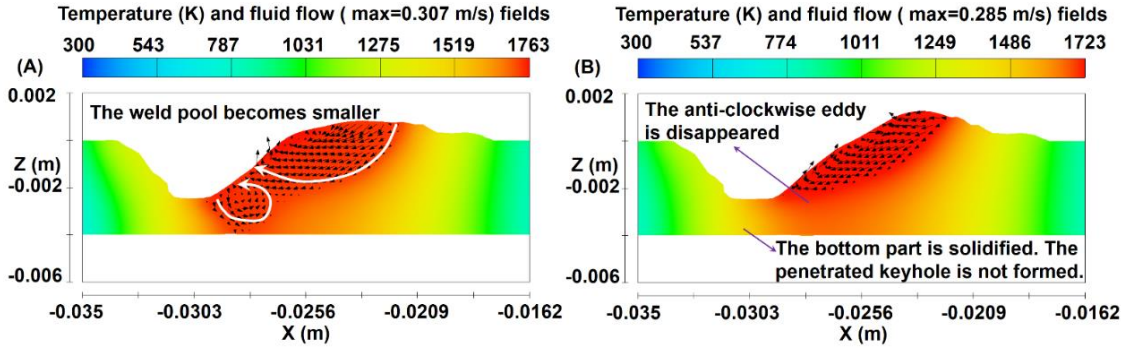

Fig. 3.24 Temperature (K) and fluid flow fields of y=0 cross sectional view at: (A) t = 3.52 s; (B) t = 3.56 s (Simulation with large thermal conductivity)

3.4.3 Penetrated keyhole stage

The keyhole is penetrated at t = 3.84s. After the penetrated keyhole formation, it can be seen from **Fig. 3.25** that at the top surface of the weld pool, near the keyhole, the molten metal flows upward and backward due to the reverse flow of the arc plasma, but obviously flows forward at the rear part of the weld pool. A clockwise eddy is formed inside the top weld pool. At the bottom surface of the weld pool, the molten metal flows downward and backward due to the downward flow of arc plasma. An anti-clockwise eddy is formed inside the bottom weld pool. In our previous study [18], with the help of an x-ray transmission system, the movement of tungsten particles was observed, and two contrary convective eddies inside the weld pool were found. With the help of a high speed camera, the movement of Zirconia particles on the weld pool surfaces was observed, and the convective patterns on the top and bottom surfaces were measured. The convective patterns on the weld pool surfaces and inside the weld pool in the numerical simulation agree well with those in our previous X-ray and high speed camera results.

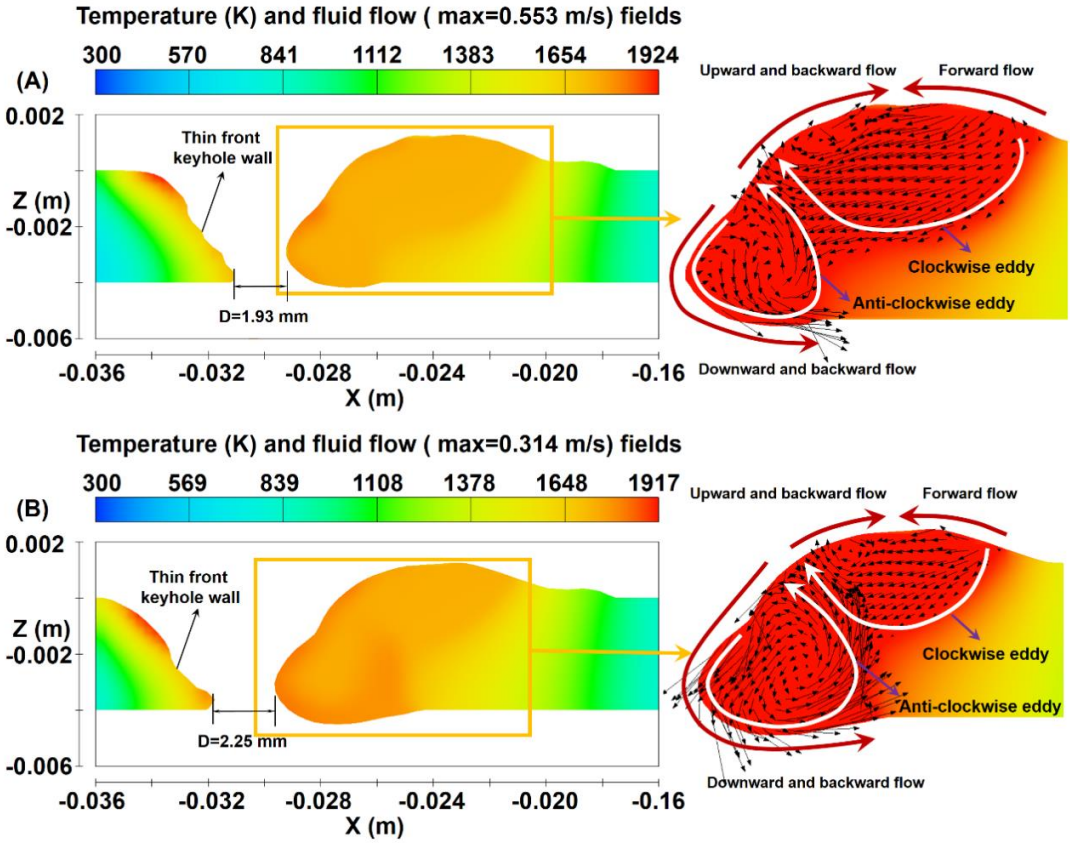

Fig. 3.25 Temperature (K) and fluid flow fields of y=0 cross sectional view at: (A) t= 3.84 s; (B) t= 4.3 s

As the plasma shear stress on the top surface of the weld pool is backward, and the Marangoni force is also backward due to the negative surface tension gradient, so near the keyhole, the molten metal on the top surface of the weld pool flows upward and backward. However, in both experiment and simulation, the forward flow can be observed at the rear part of the top surface of the weld pool. As shown in **Fig. 3.26(A)**, the dot line indicates the weld pool edge. On the top surface, Zirconia particles P_1 and P_2 locate at the rear part of the weld pool, and a Zirconia particle P_3 is close to the keyhole. As shown in **Fig. 3.26(B)** to **(C)**, P_1 and P_2 flow forward, and P_3 flows backward to the rear part of the weld pool.

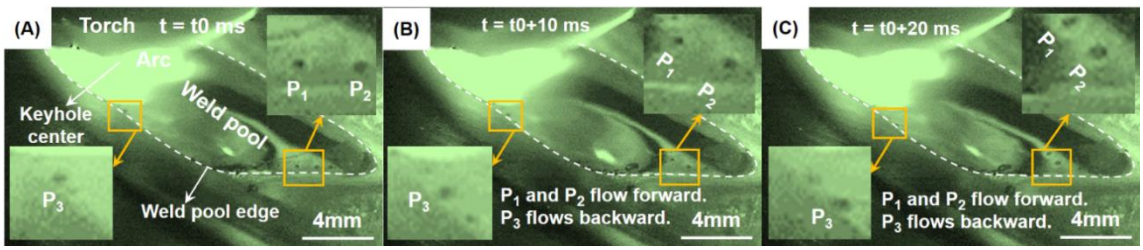

Fig. 3.26 High speed photographs of the movement of the Zirconia particles

The reason responsible for the forward flow at the rear part of the top surface is explained based on numerical simulation. **Fig. 3.27** shows the temperature and fluid flow fields of different cross sectional views at t = 4.3 s. It can be seen that near the keyhole center, the convection pattern on the top surface is similar to that in **Fig. 3.25**, and the forward flow can also be obviously observed at the rear part of the top surface of the weld pool. Near the weld pool edge, the molten metal on the top surface obviously flows backward to the rear part of the weld pool.

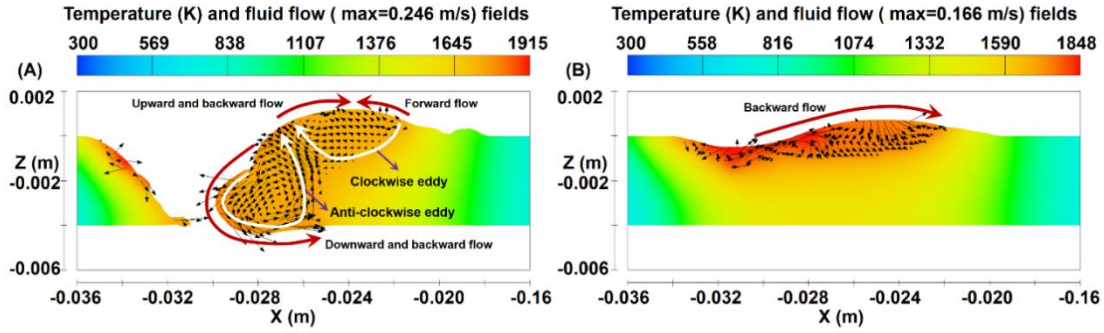

Fig. 3.27 Temperature (K) and fluid flow fields at t = 4.3 s: (A) y= 0.001 mm cross sectional view; (B) y= 0.003 mm cross sectional view

Fig. 3.28 shows the weld pool convection in the three dimensional view at t = 4.3 s. Due to the high plasma shear stress, the molten metal near the arc center flows backward and outward. As shown in **Fig. 3.6**, when the radius is larger than 0.01 m, the plasma shear stress is very small. As the rear part of the top weld pool is far away from the arc center (more than 0.01 m), the plasma shear force here is very small. Besides, due to the small temperature gradient at the rear part of the top surface of the weld pool, the Marangoni force is also very small. So at the rear part of the top surface of the weld pool, when the molten metal reaches the weld pool edge, it will change the flow direction, causing the forward flow.

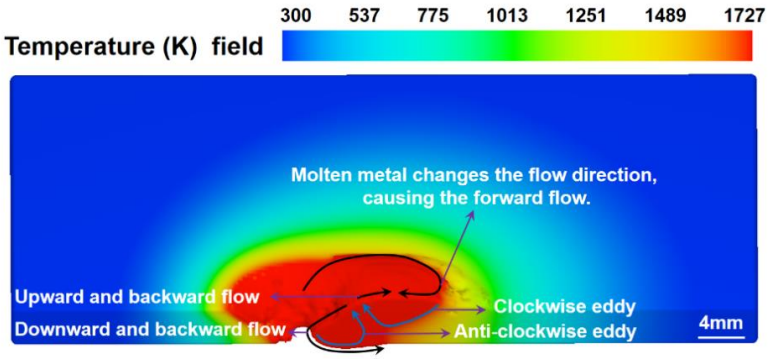

Fig. 3.28 Three dimensional temperature (K) field of the weld pool at t = 4.3 s

3.4.4 Comparison of experiment and numerical simulation

As shown in **Fig. 3.29**, both in the numerical simulation and experiment, the keyhole depth increases very quickly at first, then smoothly, and then quickly again.

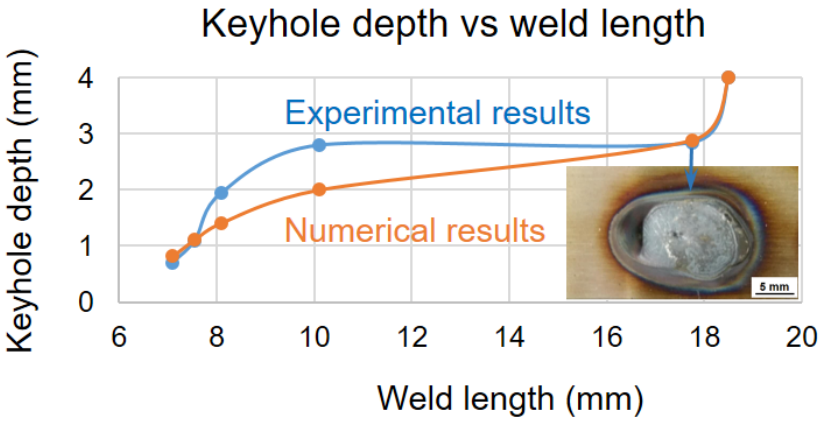

Fig. 3.29 Keyhole depth vs weld length

The schematic illustration of the convective patterns of the weld pool is shown in **Fig. 3.30**. The convective patterns of the weld pool in numerical simulation agree well with experimental results [18].

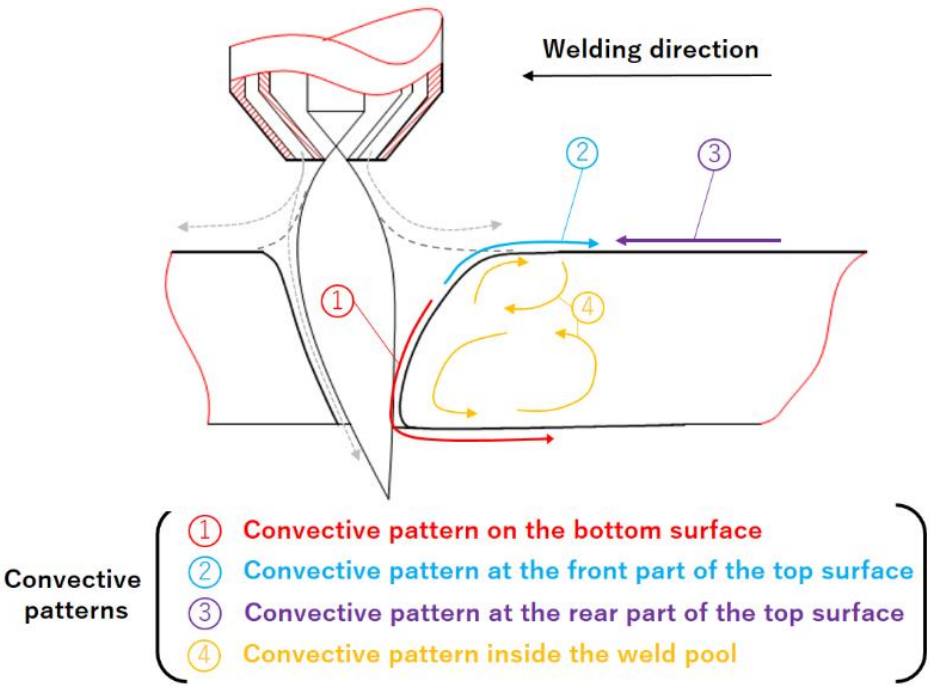

Fig. 3.30 Schematic illustration of the convective patterns of the weld pool

As shown in **Fig. 3.31**, in the experiment, the weld widths on the top and bottom surface are 8.65 mm and 4.52mm, respectively. In the simulation, the weld widths on

the top and bottom surface are 9.06 mm and 3.50 mm, respectively. The calculated weld geometry is basically in agreement with the experimental result. It should be noted that the weld width and weld reinforcement obtained by numerical simulation are smaller than these obtained by experiment, which may be caused by the underestimation of the downward plasma shear stress after the penetrated keyhole formation. In the future, we will develop fully coupled plasma arc-keyhole-weld pool model to investigate the energy propagation and force distribution in the keyhole plasma arc welding.

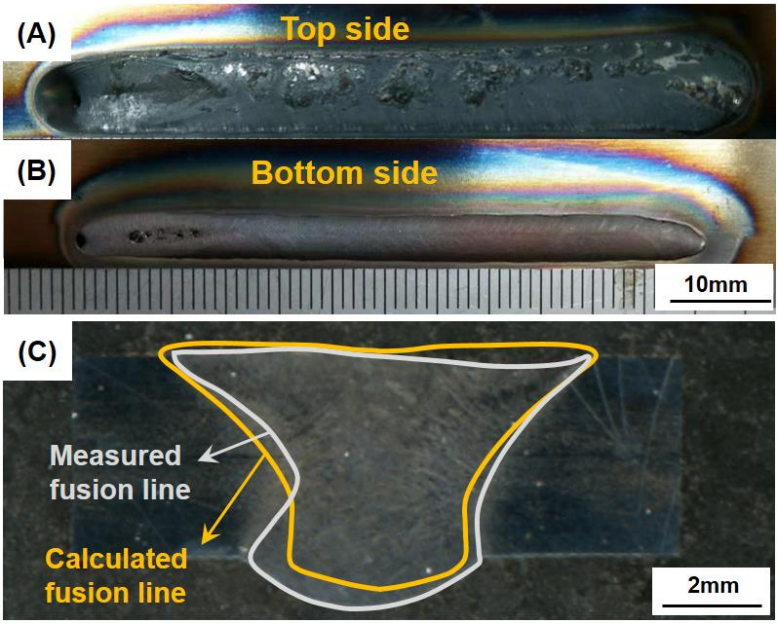

Fig. 3.31 (A) Top surface of the weld bead; (B) Bottom surface of the weld bead; (C) Comparison of calculated and experimental weld profiles at the transverse cross section

3.5 Conclusions

In this study, a novel one way coupled electrode-arc-weld pool model considering the influence of the backside keyhole deviation on the heat source distribution, the influence of the keyhole constraint on the arc pressure, and the keyhole geometry dependent plasma shear stress, is developed to study the keyhole formation in the KPAW process. The conclusions can be summarized as follows:

(1) In the blind keyhole stage, the arc pressure deepens the keyhole. The plasma shear stress facilitates the fluid flow along the rear keyhole wall and decreases the curvature of the keyhole. These two forces both contribute to the blind keyhole formation, and the arc pressure is more dominant.

(2) In the blind keyhole stage, the surface tension pressure is increased, while the

plasma shear stress is decreased with the increase of keyhole depth, so the keyhole depth increases very quickly at first, and then smoothly.

(3) Both the pressure balance and mass conservation mechanisms contribute to the blasting penetration.

(4) The material properties have great influences on the blasting penetration. Low melting temperature, low surface tension and bottom surface deformation facilitate the blasting penetration, while high thermal conductivity inhibits it.

(5) In the penetrated keyhole stage, two contrary convective eddies are found inside the weld pool. At the top surface of the weld pool, the molten metal flows upward and backward near the keyhole, but obviously flows forward at the rear part of the weld pool. At the bottom surface of the weld pool, the molten metal flows downward and backward.

Chapter 4 Analysis of the energy propagation in the keyhole plasma arc welding process

4.1 Introduction

There are many mechanisms responsible for the electrical energy propagation in the keyhole plasma arc welding (KPAW) process [106]. For example, thermionic cooling from the emission of electrons, ion heating and radiation cooling at the cathode; Ohmic heating and radiation cooling at the arc column; Electron condensation heating, energy conduction from the arc to the anode and radiation cooling at the anode. As the distribution of energy during the welding has great influences on the final weld quality [107], deep understanding of the energy propagation in the KPAW process can help provide guidance to the welding engineers in developing KPAW procedures to obtain high quality welds.

It should be noted that in the plasma system, the arc is concentrated and straight [108,109]. Due to the strong constrained effect of the water cooled copper nozzle, the arc temperature and arc pressure in the KPAW process are much high [110], and thus a penetrated keyhole is formed during the welding [6]. However, the penetrated keyhole formation can't increase the energy absorption in the KPAW process.

Developing of a coupled model considering complicated interactive phenomena is necessary to give in-depth knowledge of the energy propagation in the KPAW process. Li et. al [111, 112] developed a unified model with a preset keyhole to investigate the energy transport phenomena in the KPAW process, and found 10% of the arc plasma outflowed from the keyhole exit. Besides, the heat conduction flux was more than two times of electron condensation flux. Xu et. al [93] also established a similar unified model, and found that the energy on the top part of the weld pool was produced by the electron condensation heating and energy conduction, while that on the bottom part was provided mainly by energy conduction. However, the plasma shear stress was not considered in their model [93,111,112]. Jian et. al built a unified model to study the interaction mechanism of the plasma arc, weld pool and keyhole in the stationary KPAW process [87], and moving KPAW process [88]. The volume of fluid (VOF) method was used to track the keyhole boundary, and the plasma shear stress was automatically calculated. It

was found that in the stationary KPAW process, the total heat flux on the weld pool surface after the keyhole formation distributed in a double-peak type. In the moving KPAW process, most of the energy were transported to the rear weld pool. A similar unified model was also developed by Pan et. al [16]. It should be noted that only the energy propagation in the keyhole formation stage was analyzed in their numerical simulations [16,87,88]. Besides, due to the bottom surface deformation was ignored, the numerical convective patterns of the weld pool can't agree well with the experimental results [18].

In this study, for the first time, a fully coupled plasma arc-keyhole-weld pool model is developed to investigate the energy propagation in the KPAW process when the weld pool reaches the quasi-steady state. The plasma arc is considered as in local thermodynamic equilibrium (LTE). The turbulent model is introduced to describe the flows of the plasma arc and weld pool. The plasma shear stress acted on the weld pool surface and the molten metal flow on the bottom surface are considered. Based on this coupled model, the energy input, transfer, dissipation and energy efficiency in the KPAW process are calculated and analyzed.

4.2 Mathematical model and numerical simulation

Fig. 4.1 shows the three dimensional computation domain in the KPAW model. The computation domain contains the cathode region (tungsten), the nozzles, the arc regions, and the anode region (basemetal) with a preset keyhole. It should be noted that all the physic phenomena in the KPAW process are symmetry, so only a half computation domain is used. The Cartesian coordinate system is used, and its origin locates at the left bottom of the symmetry plane. The z-axis is normal to the top surface of the workpiece. The size of the basemetal is 50 mm x 25 mm x 4 mm. The heights of gas region 1 and gas region 2 are 20 mm and 11 mm, respectively. During the simulation, the welding torch is stationary, and the basemetal moves from the left side to the right side, so the welding direction is along the negative x-axis.

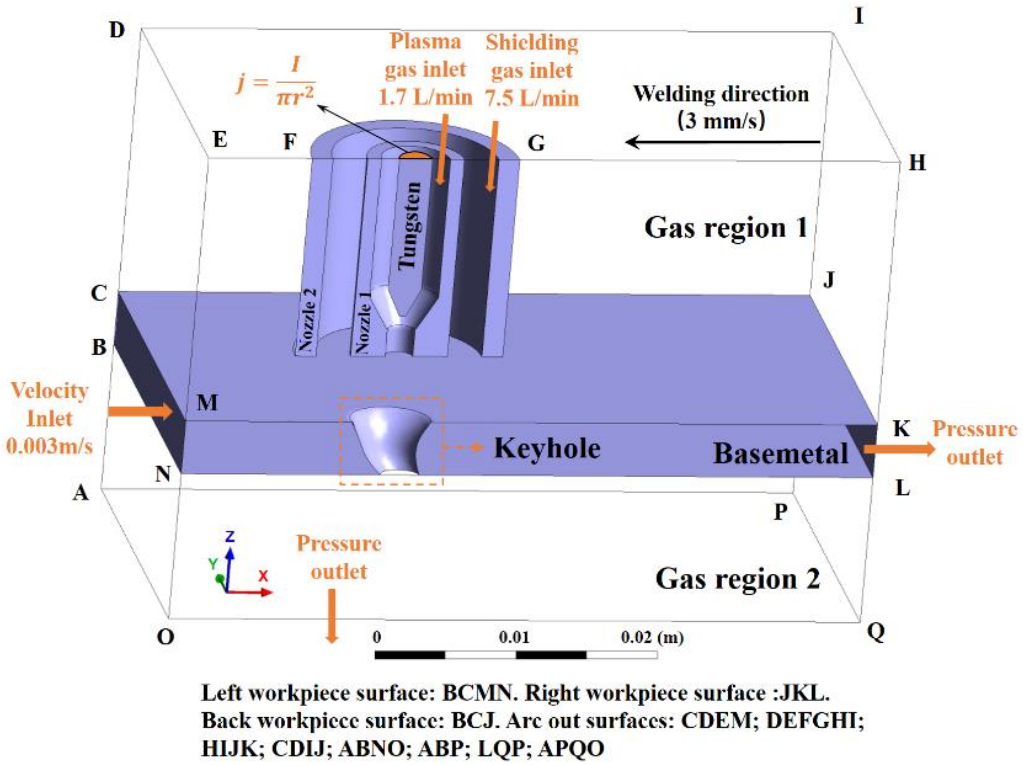

Fig. 4.1 The computation domain in the KPAW model

In previous coupled model [16,87,88], the VOF method was adopted to track the varying keyhole boundary in the KPAW process, which caused large amount of calculation. Besides, the calculated flow patterns inside the weld pool can't agree well with the X-ray results [18]. In our previous study [35], the arc heat source, arc pressure and arc shear stress were adopted as boundary conditions in the KPAW weld pool modelling, in which the VOF method was also used to track the free surface. However, the plasma arc was ignored in our numerical model. It should be noted that when the KPAW process reaches the quai-steady state, the weld pool size and keyhole shape are almost unchanged as time goes by. With this predefined keyhole method, the amount of calculation is reduced, and reasonable numerical results can be obtained.

In order to simplify the complex interaction of the plasma arc, keyhole and weld pool in the KPAW process, some assumptions are introduced: (1) The plasma arc is in LTE, which means the electron temperature and heavy temperature are same. (2) The plasma arc and weld pool are considered as Newtonian and incompressible fluids. (3) The flows of the plasma arc and weld pool are turbulent, and the k- ε model is used to describe the turbulent flows [16]. (4) The metal vapor from the weld pool is not

considered. Based on our previous experimental study [35], the maximum temperature of the weld pool was only 1875 K when the welding current was 120 A. Jian et. al [103] investigated the influence of the metal vapor on the weld pool behavior in the KPAW process based on numerical simulation, and found that the maximum mass fraction of the Fe vapor was only 0.24% when the welding current was 190 A. In this study, the welding current is 90 A, so it is reasonable to ignore the effect of the metal vapor.

4.2.1 Mathematic model

4.2.1.1 Governing equations

The mass, fluid flow, energy propagation and current in the computation domain are governed by the mass, momentum, energy, current and turbulence kinetic energy conservation equations.

Mass conservation equation:

$$\frac{\partial \rho}{\partial t} + \nabla \cdot (\rho \boldsymbol{v}) = 0 \tag{4.1}$$

where ρ is the density, t is the time, $\boldsymbol{v}$ is the velocity vector.

Momentum conservation equation:

$$\frac{\partial (\rho \boldsymbol{v})}{\partial t} + \nabla \cdot (\rho \boldsymbol{v}\boldsymbol{v}) = -\nabla P - \nabla \cdot \tau + \boldsymbol{J} \times \boldsymbol{B} + \boldsymbol{G} + \boldsymbol{S_v} \tag{4.2}$$

The Boussinesq's approximation is used to calculate the buoyance force in the weld pool [90]. The porous media drag model is used to deal with the solid- liquid phase change in the weld pool, and the Darcy damping force $\boldsymbol{S_v}$ is included in the momentum conservation equation [91].

In the plasma arc, $\boldsymbol{G} = \rho \boldsymbol{g}$, $\boldsymbol{S_v} = 0$ (4.3)

In the weld pool, $\boldsymbol{G} = \rho \boldsymbol{g} \beta (T - T_l)$, $\boldsymbol{S_v} = C_0 \frac{(1-f_l)^2}{f_l^3 + \delta} \boldsymbol{v}$ (4.4)

The liquid fraction f_l is given by [29]:

$$f_l = \begin{cases} 0 & T < T_s \\ \frac{T - T_s}{T_l - T_s} & T_s \leq T \leq T_l \\ 1 & T > T_l \end{cases} \tag{4.5}$$

where P is the pressure, τ is the viscosity stress tensor, $\boldsymbol{J}$ is the current density vector, $\boldsymbol{B}$ is the magnetic flux density vector, $\boldsymbol{g}$ is the gravitational acceleration, β is the thermal expansion coefficient, C_0 is the mushy zone constant, δ is a non-zero fractional

denominator constant, T is the temperature of the weld pool, T_l and T_s are the liquidus and solidus temperatures of the basemetal.

Energy conservation equation:

$$\frac{\partial(\rho h)}{\partial t} + \nabla \cdot (\rho \boldsymbol{v} h) = \nabla\left(\frac{K}{c_p}\nabla h\right) + \boldsymbol{J} \cdot \boldsymbol{E} - S_h \quad (4.6)$$

In the plasma arc, the radiative loss is considered. $S_h = U$ (4.7)

In the weld pool, the latent heat of fusion is considered. $S_h = \Delta H \frac{\partial f_l}{\partial t}$ (4.8)

where h is the enthalpy, K is the thermal conductivity, c_p is the specific heat, $\boldsymbol{E}$ is the electric field vector, U is the radiative loss of the plasma arc, ΔH is the latent heat of fusion of the basemetal.

Current conservation equation [113]:

$$\nabla \cdot (\sigma \nabla \varphi) = 0 \quad (4.9)$$

Ohm's law [113]:

$$\boldsymbol{J} = -\sigma(\nabla \varphi) \quad (4.10)$$

Vector potential [113]:

$$\nabla^2 \boldsymbol{A} = -\mu_0 \boldsymbol{J} \quad (4.11)$$

Magnetic field [113]:

$$\boldsymbol{B} = \nabla \times \boldsymbol{A} \quad (4.12)$$

where σ is the electric conductivity, ψ is the electric potential, $\boldsymbol{A}$ is the vector potential, μ_0 is the permeability of vacuum.

The standard two-equation k-ε model is used. The turbulence kinetic energy, k, and its rate of dissipation, ε, are obtained from the following conservation equations [16]:

$$\frac{\partial}{\partial t}(\rho k) + \nabla \cdot (\rho \boldsymbol{v} k) = \nabla \cdot \left(\left(\mu + \frac{\mu_t}{\sigma_k}\right)\nabla k\right) + \rho G_k - \rho \varepsilon \quad (4.13)$$

$$\frac{\partial}{\partial t}(\rho \varepsilon) + \nabla \cdot (\rho \boldsymbol{v} \varepsilon) = \nabla \cdot \left(\left(\mu + \frac{\mu_t}{\sigma_\varepsilon}\right)\nabla \varepsilon\right) + \frac{C_1 G_k \rho \varepsilon}{k} - \frac{C_2 \rho \varepsilon^2}{k} \quad (4.14)$$

The generation of the turbulence kinetic energy, G_k, due to the mean velocity gradients is calculated by:

$$G_k = \frac{\mu_t}{\rho}\left\{2\left[\left(\frac{\partial v_x}{\partial x}\right)^2 + \left(\frac{\partial v_y}{\partial y}\right)^2 + \left(\frac{\partial v_z}{\partial z}\right)^2\right] + \left(\frac{\partial v_x}{\partial y} + \frac{\partial v_y}{\partial x}\right)^2 + \left(\frac{\partial v_x}{\partial z} + \frac{\partial v_z}{\partial x}\right)^2 + \left(\frac{\partial v_y}{\partial z} + \frac{\partial v_z}{\partial y}\right)^2\right\} \quad (4.15)$$

The turbulent viscosity, μ_t, is given by:

$$\mu_t = c_\mu \rho \frac{k^2}{\varepsilon} \tag{4.16}$$

The turbulent thermal conductivity, K_t, is derived from the Prandtl number of the turbulence:

$$Pr_t = \frac{c_p \mu_t}{K_t} = 0.9 \tag{4.17}$$

where μ is the fluid viscosity, v_x, v_y and v_z are the fluid velocities in the x, y, z directions. The recommended values for the empirical constants are c_μ=0.09, c_1 =1.44, c_2=1.92, σ_k=1.0 and σ_ε= 1.3.

4.2.1.2 Boundary conditions

It should be noted that there is a sheath layer between the arc and metal, where the heavy particle temperature and electron temperature are different. The LTE conservation equations can't be used in this layer. In our previous study, the LTE-diffusion approximation was proposed. The mesh size close to the sheath was set to the diffusion length of electrons, so the non-LTE region can be avoided in the numerical simulation. In this study, the LTE-diffusion approximation is used to treat the plasma arc / metal interface.

At the cathode surface, the additional heat flux including the cathode thermionic cooling, ion heating, conduction energy and radiation cooling is considered [115]. The conduction energy is determined by solving the energy conservation equation in the whole computation domain.

$$H_c = -|j_e|\varphi_c + |j_i|V_i - \varepsilon_r \alpha T^4 \tag{4.18}$$

At the anode surface, the additional heat flux including the electron condensation heating, conduction energy (q_c) and radiation cooling is considered [115].

$$H_a = |j|\varphi_a + q_c - \varepsilon_r \alpha T^4 \tag{4.19}$$

$$q_c = -k_{eff} \frac{T_g - T_m}{\delta} \tag{4.20}$$

where j_e is the electron current density, j_i is the ion current density, j is the current density at the anode surface, ψ_c is the work function of the cathode, ψ_a is the work function of the anode, V_i is the ionization potential of argon, ε_r is the surface radiation emissivity, α is the Stefan-Boltzmann constant, k_{eff} is the effective thermal conductivity, δ is the length of the anode sheath region, T_g and T_m are the arc temperature and metal temperature

at the interface, respectively.

The arc pressure, Marangoni force, plasma shear stress, Lorentz force, and buoyancy force are five principal forces for the fluid flow in the weld pool. The Lorentz force and buoyancy force are volumetric forces, which are described in Eq. (4.2) and Eq. (4.4). The arc pressure, Marangoni force and plasma shear stress act on the weld pool surface.

The pressure boundary at the keyhole wall is given as:

$$\boldsymbol{P} = \boldsymbol{P_{arc}} - \frac{\gamma}{R} \tag{4.21}$$

The momentum boundary of the weld pool surface at the tangential direction is given as:

$$-\mu \frac{\partial \boldsymbol{v_t}}{\partial \boldsymbol{n}} = \boldsymbol{\tau_m} + \boldsymbol{\tau_p} \tag{4.22}$$

The Marangoni force is calculated as follows [116]:

$$\boldsymbol{\tau_m} = \frac{\partial \boldsymbol{\gamma}}{\partial T}\frac{\partial T}{\partial S} \tag{4.23}$$

In previous studies, the shear stress caused by the normal impingement of a jet on a flat surface was adopted to describe the arc shear stress [34,117]. In this study, the plasma shear stress is calculated as follows:

$$\boldsymbol{\tau_p} = -\mu_p \frac{\partial \boldsymbol{v_p}}{\partial \boldsymbol{n}} \tag{4.24}$$

where $\boldsymbol{P_{arc}}$ is the arc pressure, γ is the surface tension, R is the keyhole radius, μ is the fluid viscosity, $\boldsymbol{v_t}$ is the tangential fluid velocity, μ_p is the plasma viscosity, v_p is the plasma velocity, $\boldsymbol{S}$ is the tangential vector, $\boldsymbol{n}$ is the normal vector.

The detailed boundary conditions can be seen in Table 4.1.

Table 4.1. External boundary conditions in the numerical simulation

Boundary	V	T (K)	ψ (V)	A (T.m)
Top electrode surface(Wall)	-	300	$j = \frac{I}{\pi r^2}$	$\frac{\partial \boldsymbol{A}}{\partial \boldsymbol{n}} = 0$
Top nozzles surfaces (Wall)	-	300	$\frac{\partial \varphi}{\partial \boldsymbol{n}} = 0$	$\frac{\partial \boldsymbol{A}}{\partial \boldsymbol{n}} = 0$
Plasma gas inlet (Mass flow inlet)	1.7 L/min	300	$\frac{\partial \varphi}{\partial \boldsymbol{n}} = 0$	$\frac{\partial \boldsymbol{A}}{\partial \boldsymbol{n}} = 0$
Shielding gas inlet (Mass flow inlet)	7.5 L/min	300	$\frac{\partial \varphi}{\partial \boldsymbol{n}} = 0$	$\frac{\partial \boldsymbol{A}}{\partial \boldsymbol{n}} = 0$
Left workpiece	0.003 m/s	300	$\frac{\partial \varphi}{\partial \boldsymbol{n}} = 0$	$\frac{\partial \boldsymbol{A}}{\partial \boldsymbol{n}} = 0$

surface (Velocity inlet)				
Right workpiece surface (Pressure outlet)	-	-	$\frac{\partial \varphi}{\partial \boldsymbol{n}} = 0$	$\frac{\partial \boldsymbol{A}}{\partial \boldsymbol{n}} = 0$
Back workpiece surface (Wall)	-	$-h_{con}\nabla T - \varepsilon_r \alpha T^4$	0	0
Arc out surfaces (Pressure outlet)	-	300	$\frac{\partial \varphi}{\partial \boldsymbol{n}} = 0$	$\frac{\partial \boldsymbol{A}}{\partial \boldsymbol{n}} = 0$

where I is the welding current, r is the tungsten radius, h_{con} is the convective heat transfer coefficient.

4.2.2 Numerical simulation

The conservation equations are solved by the commercial CFD solver FLUENT. The User-Defined Scalar (UDS) is used to treat the electromagnetic scalar equations, and the User-Defined Function (UDF) is used to treat the source terms. A non-uniform grid system is used: 0.1 mm near the cathode, 0.3 mm in the arc region and weld pool, and 0.5mm in other parts. The governing equations and auxiliary equations are solved iteratively by the Pressure-Implicit with Splitting of operators (PISO) algorithm. The momentum and energy equations are discretized by Second Order Upwind difference. The turbulent kinetic energy, turbulent dissipation rate and User-Defined Scalar are discretized by First Order Upwind difference. The convergence criteria for the residuals of continuity, momentum, turbulent kinetic energy, turbulent dissipation rate and User-Defined Scalar is 10^{-3}. The convergence criteria for the residual of energy is 10^{-6}.

4.3 Experimental method

Fig. 4.2 shows the welding setup used in the experiment. A welding power source (NW-300ASR, Nippon Steel Welding & Engineering Co., Ltd.) and a transfer-type plasma arc welding torch (100WH, Nippon Steel Welding & Engineering Co., Ltd.) are used as the welding equipment. The diameter of the torch orifice is 2.0 mm and the electrode setback is 3.0 mm. The base metal is the stainless steel SUS304 plates with the dimension of 300 mm x 100 mm x 4 mm. The thermo-physical material properties of SUS304 stainless steel can be seen from our previous study. The distance between the

nozzle and the base metal is about 5.0 mm. The welding current is DC90 A and the welding speed is 3 mm/s. The pure Ar is used as the main plasma gas and shielding gas. In order to protect the back weld bead from being oxidized, a back-shielding gas box is put on the welding jig during the welding. The main plasma gas flow rate is 1.7 l/min, and the shielding gas flow rate is 7.5 l/min.

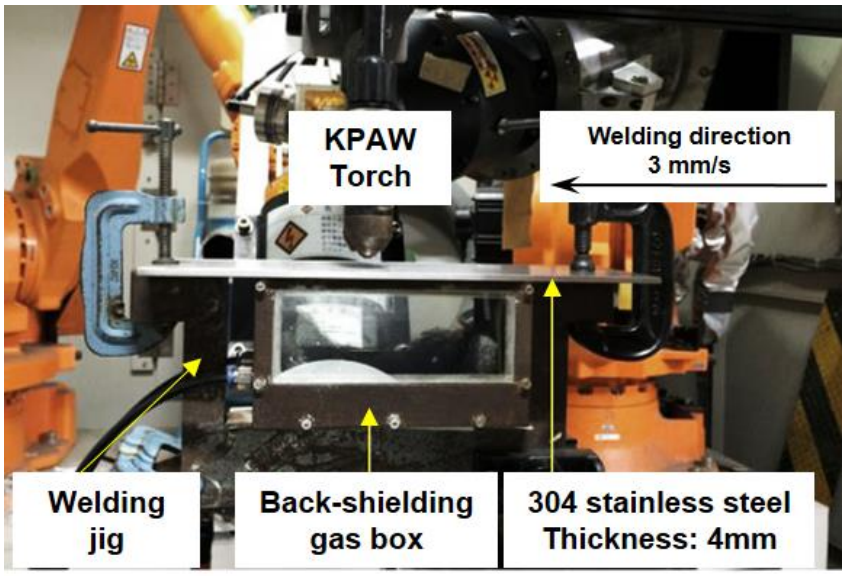

Fig. 4.2 The photograph of the welding setup

4.4 Results and discussion

Based on the numerical simulation, the plasma arc physics and weld pool convection are studied. The energy propagation from the arc to the weld pool, the energy propagation inside the weld pool and the energy efficiency are elucidated.

4.4.1 Energy propagation from the arc to the weld pool

Fig. 4.3 shows the temperature distribution in the symmetry plane. It can be seen that due to the constraint of the water cooled copper nozzle (Region 1), the arc temperature and arc temperature gradient near the nozzle are very high, and the maximum temperature (about 24000 K) can be observed at the torch axis. In the region below the nozzle and above the basemetal (Region 2), without any constraint, the arc expands freely in the horizontal direction. In the keyhole (Region 3), the arc is also confined by the keyhole. Below the basemetal (Region 4), the efflux arc can be observed from the keyhole exit.

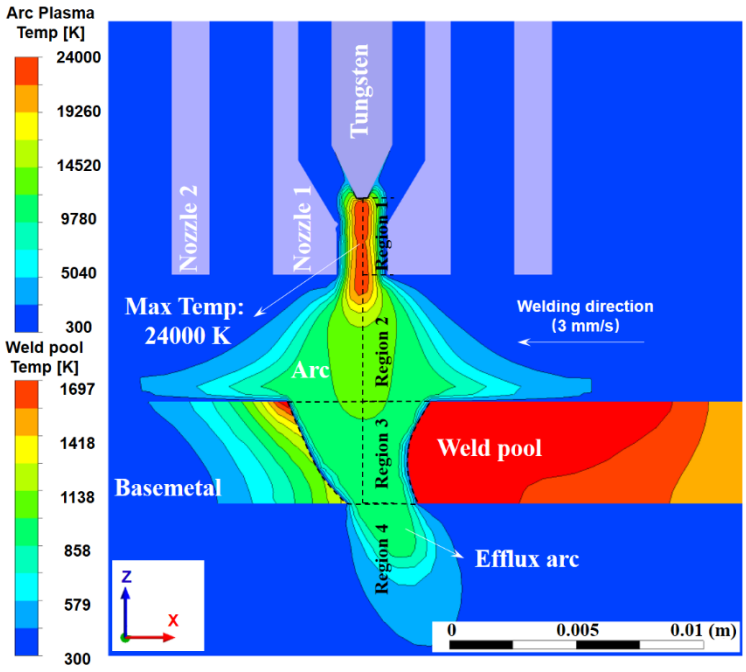

Fig. 4.3 The arc temperature distribution of the KPAW process in the symmetry plane

The arc temperature distribution along the torch axis is shown in **Fig. 4.4**. It can be seen that in region 1, the arc temperature is increased firstly, and then decreased. In the region 2, without any constraint, the arc temperature is decreased very sharply, and the average decreasing rate is 1970000 K/m. In the region 3, due to the constraint of the keyhole, the arc temperature is decreased slowly at the top part of the weld pool. At the bottom part of the weld pool, the constraint effect becomes weak, and the arc temperature is decreased quickly. The average decreasing rate in Region 3 is 287500 K/m.

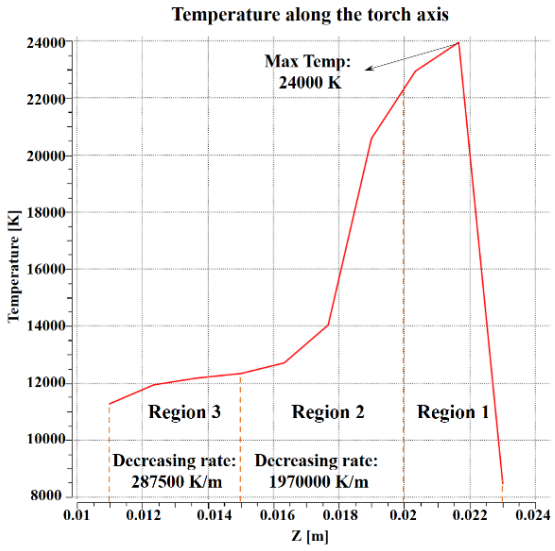

Fig. 4.4 The arc temperature distribution along the torch axis

Based on Eq. (4.20), the conduction energy flux from the arc to the weld pool can be calculated. As shown in **Fig. 4.5 (A)**, the conduction energy flux at the top part of the weld pool is higher than that at the bottom part of the weld pool. Besides, the maximum conduction energy flux locates at the middle of the rear keyhole wall, and its value is 2.685E7 W/m^2. It should be noted that that the conduction energy flux is highly related to the temperature difference between the arc temperature and metal temperature. The metal temperature at the bottom front keyhole is lower, as shown in **Fig. 4.3**, but the arc temperature is much higher at the top and rear parts of the keyhole, as shown in **Fig. 4.5 (B)**, so the conduction energy flux at the top and rear parts of the keyhole is higher.

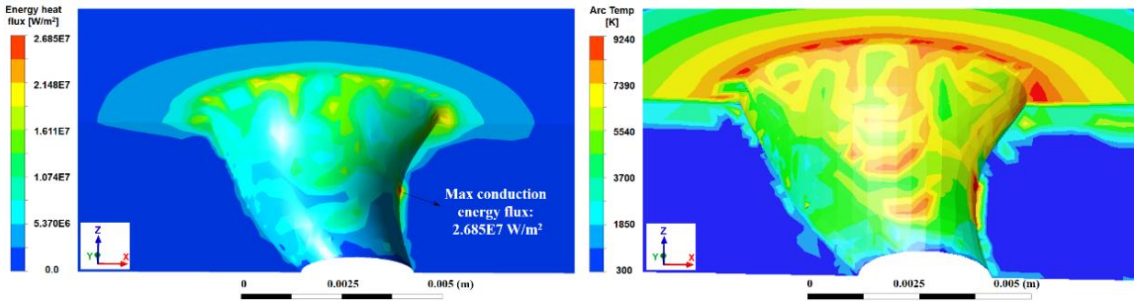

Fig. 4.5 (A) The conduction energy flux from the arc to the weld pool; (B) The arc temperature at the interface

Fig. 4.6 (A) and **(B)** shows the electric energy flux and total energy flux from the arc to the weld pool. The electric energy flux at the top part of the weld pool are much higher than that at the bottom part of the weld pool, which means that the welding current flows mainly from the top part of the weld pool to the tungsten. It should be noted that the current density distribution is determined by the electric conductivity and conductive area. In region 3, the arc temperature is within the range of [11000 K, 13000 K], and the electric conductivity increases with the temperature. From the top to the bottom part of the weld pool, the arc temperature and electric conductivity are decreased, so the current density is also decreased. The maximum electric energy flux is 2.682E7 W/m^2, which is similar to the maximum conduction energy flux. The maximum total energy flux locates at the top of the side keyhole wall, and its value is 4.648E7 W/m^2.

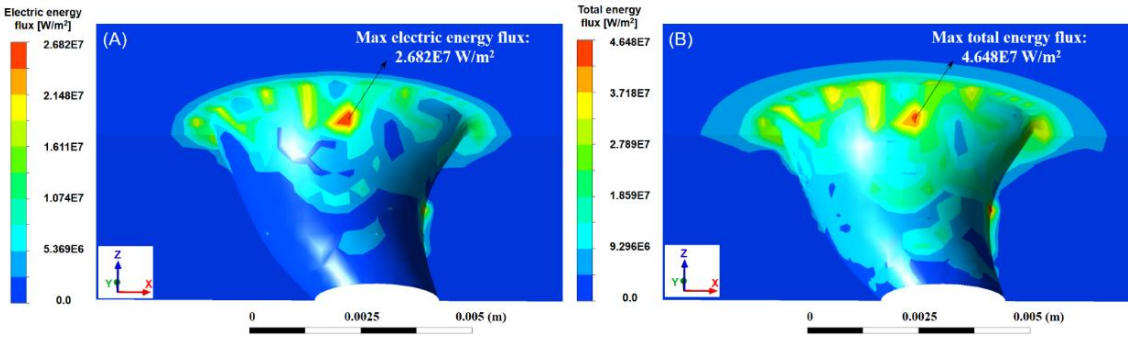

Fig. 4.6 (A) The electric energy flux from the arc to the weld pool; (B) The total energy flux from the arc to the weld pool

4.4.2 Energy propagation in the weld pool

As discussed above, the arc temperature (Max temp: 24000 K) and the total energy flux at the top part of the weld pool in the KPAW process are very high. As shown in **Fig. 4.7**, a high temperature region is formed near the keyhole. However, the maximum temperature of the weld pool is only 1857 K, which means that the energy is not accumulated on the top weld pool surface in the KPAW process. It can also be seen that the weld pool size on the top surface is larger than that on the bottom surface.

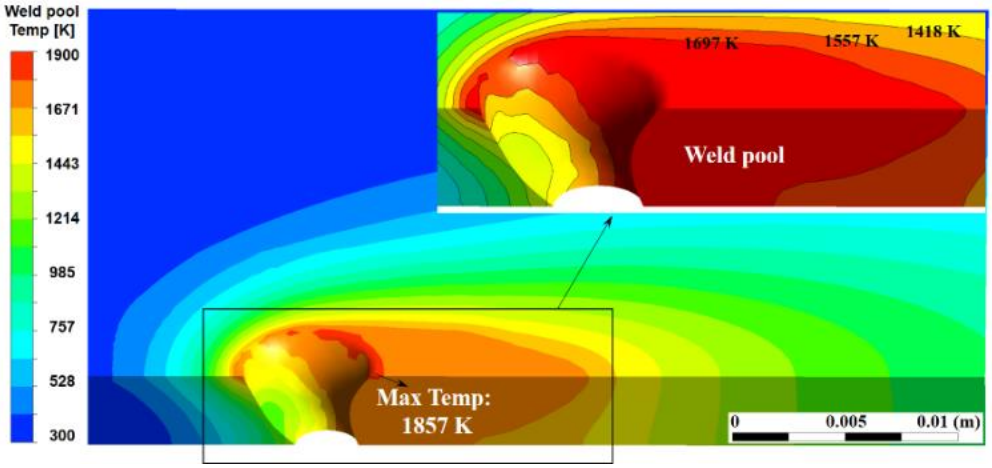

Fig. 4.7 The temperature distribution of the weld pool in the numerical simulation

The energy conduction and energy convection are two main mechanisms for the energy propagation in the weld pool, and the Peclet number can be used to determine which mechanism is dominant. The three dimensional convective patterns inside the weld pool and the weld pool convective patterns in the symmetry plane are presented in **Fig. 4.8**. It can be seen that there are two dominant convective eddies inside the weld pool: a clockwise eddy at the top part of the weld pool, and an anti-clockwise eddy at the bottom

part of the weld pool. At the top and bottom surfaces, the molten metal flows backward. The maximum velocity of the weld pool is 0.2884 m/s. Based on Eq. (4.25), the Peclet number of the weld pool is about 319. In previous study, the Peclet number of the weld pool in double electrodes tungsten inert gas welding was calculated, and its value was only 77 [100].

Qualitatively, when the Peclet number is larger than 10, the contribution of the energy convection increases. The much high Peclet number means that the energy convection caused by the fluid flow is the dominant mechanism for energy propagation in the weld pool in the KPAW process [118].

$$Pe = \rho CVL/K \tag{4.25}$$

where ρ is fluid density (6900 kg/m^3), C is specific heat (720 J/kg·K), L is the characteristic length (Weld pool surface radius: 0.00633 m), V is the characteristic velocity (0.2884 m/s), K is thermal conductivity (28.4 W/m·K).

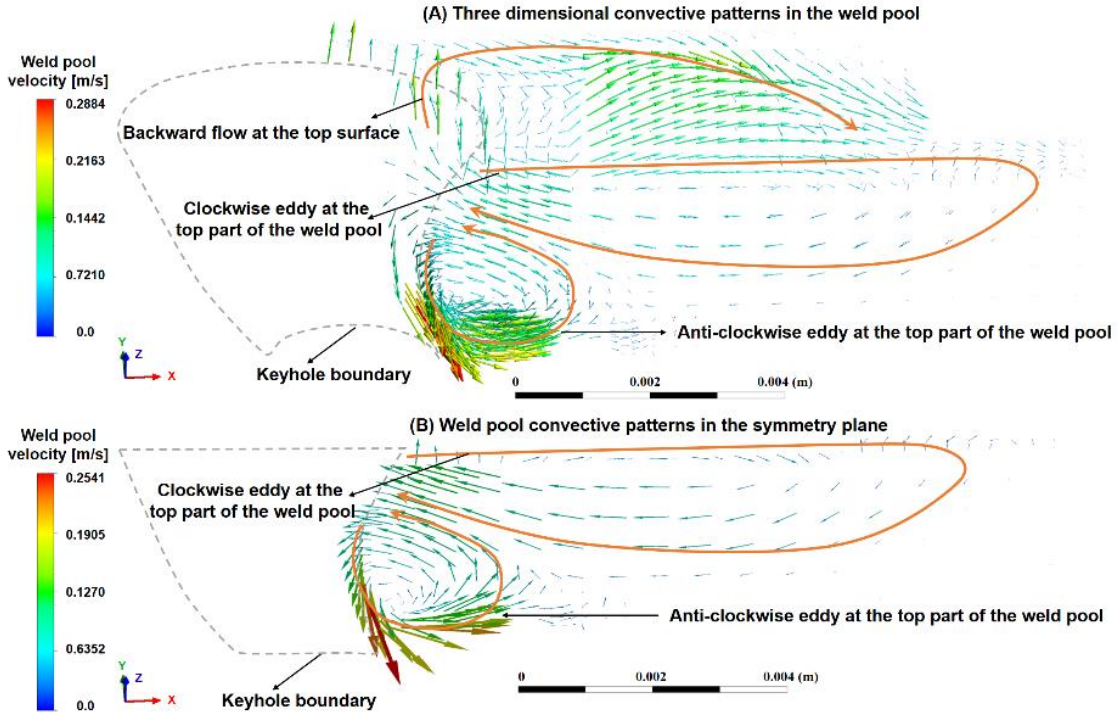

Fig. 4.8 The weld pool convective patterns

Our previous study showed that the arc pressure and plasma shear stress are the two most important driven forces for the fluid flow in the KPAW process [35]. It should be noted that the arc pressure and plasma shear stress are obtained using an electrode-arc

model with flat surface, which is much different from actual welding process. In this study, the arc pressure and plasma shear stress distributions along the keyhole wall are presented.

As shown in **Fig. 4.9**, in the *x* direction, the arc pressure is negative at the front keyhole wall, and positive at the rear keyhole wall, and the minimum value is -1.189E8 N/m^3. In the *y* direction, the arc pressure is positive at the front and rear keyhole walls, and the maximum value is 5.012E7 N/m^3. In the *z* direction, the arc pressure is negative at the front keyhole wall and top part of the rear keyhole wall, and the minimum value is -5.434E7 N/m^3. It should be noted that in the KPAW process, the keyhole channel is backward curved [119], as shown in **Fig. 4.9 (D)**. As a result, the arc pressure is positive at the bottom part of the rear keyhole wall in the *z* direction.

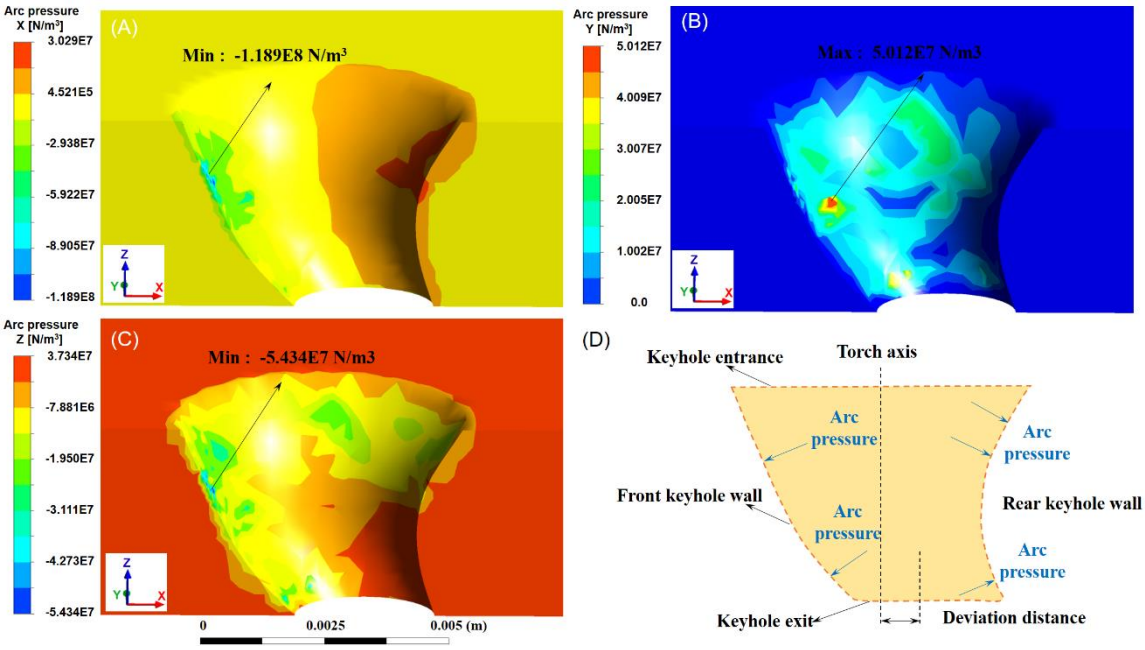

Fig. 4.9 The arc pressure distribution along the keyhole wall: (A) In the x direction; (B) In the y direction; (C) In the z direction; (D) The schematic diagram of the keyhole

Fig. 4.10 shows the plasma arc velocity distribution in the symmetry plane. It can be seen that at the top part of the weld pool, the plasma arc strikes the front and rear keyhole walls, and then flows upward and outward. At the bottom part of the weld pool, the plasma arc strikes the keyhole wall, and then flows downward. So both the reverse flow and downward flow of the plasma arc exist inside the keyhole.

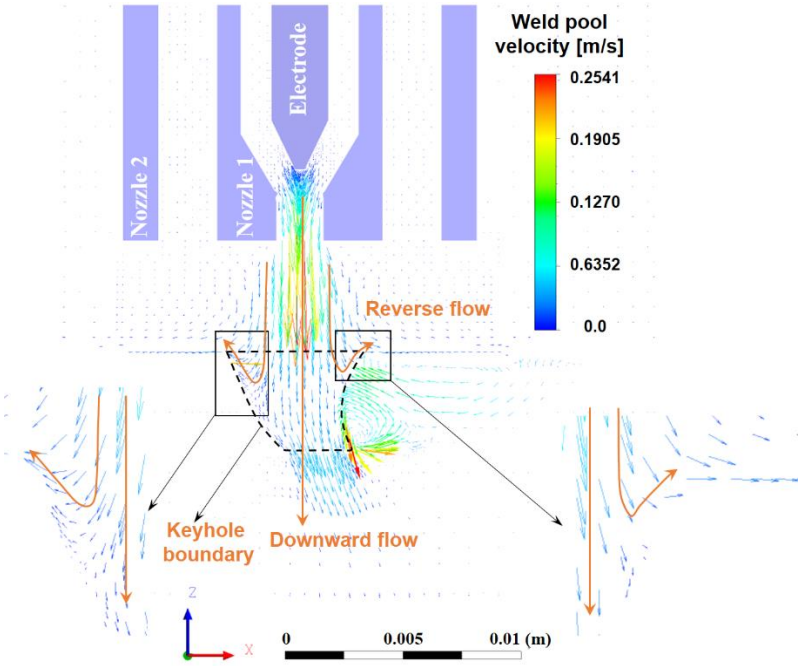

Fig. 4.10 The plasma arc velocity distribution in the symmetry plane

As shown in **Fig. 4.11**, due to the reverse flow of the plasma arc, at the top part of the weld pool, the plasma shear stress is outward in the *x* and *y* directions, and upward in the *z* direction. Due to the downward flow of the plasma arc and the reduction of bottom keyhole cross-sectional area, at the bottom part of the weld pool, the plasma shear stress is inward in the *y* direction, and downward in the *z* direction. The maximum shear stress locates at the bottom of the keyhole wall. It should be noted that owing to the backward curved keyhole channel, as shown in **Fig. 4.11 (D)**, the shear stress is inward at the bottom part of the front keyhole wall, but outward at the bottom part of the rear keyhole wall in the *x* direction.

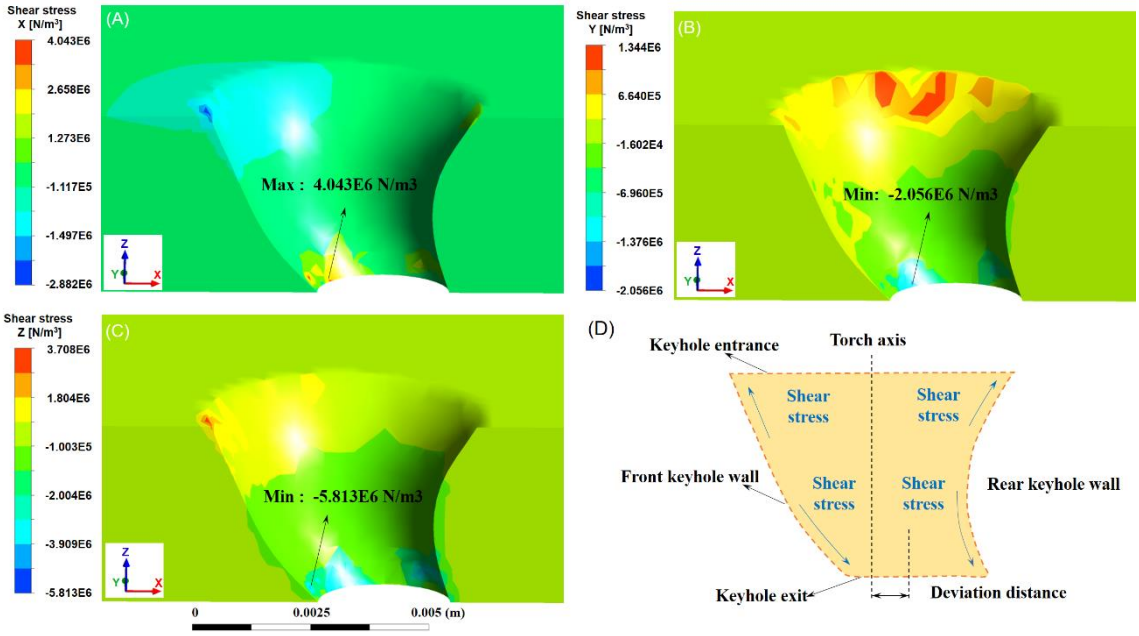

Fig. 4.11 The shear stress distribution along the keyhole wall: (A) In the *x* direction; (B) In the *y* direction; (C) In the *z* direction; (D) The schematic diagram of the keyhole

4.4.3 Energy efficiency

As shown in **Fig. 4.12**, the conduction energy from the arc to the cathode is 215.9 W, and the energy gained by the cathode from ion bombardment (ion heating) is 704.9 W. The thermionic cooling and radiation emission of the cathode is 739.7 W and 23.2 W, respectively. The Ohmic heating in the cathode is 21.6 W, and the conduction energy loss through the top of the cathode is 135.4 W.

The Ohmic heating in the arc column is 2975 W. The conduction energy loss through the arc out surfaces is 1012.3 W, and the energy loss by radiation from the arc plasma is 316.1 W.

The conduction energy from the arc to the anode is 1375.4 W, and the electron condensation heating by the electrons absorbed at the anode surface is 438.7 W. The Ohmic heating in the anode is 1 W, and the radiation emission of the anode is 58 W.

As shown in **Fig. 4.5** and **Fig. 4.6(A)**, even though the maximum conduction energy flux and maximum electric energy flux are similar, the distribution area of the conduction energy flux is much larger, so the conduction energy from the arc to the anode is much higher than the electron condensation heating. It should be noted that the conduction energy and electron condensation heating are about equal in the GTAW process [17]. The reasons can be explained as following: When the same welding current is used, the arc

size in the KPAW process is larger than that in the GTAW process, and a large penetrated keyhole is formed in the KPAW process, so the arc-anode area in the KPAW process is much larger. Besides, the arc temperature in the KPAW process is much larger than that in the GTAW process. All of these reasons contribute to a higher conduction energy / electron condensation heating ratio in the KPAW process than that in the GTAW process.

Another interesting thermo-physical phenomenon is that the radiation loss of the anode in the KPAW process is very high. This is because during the KPAW process, a large penetrated keyhole is formed, and the weld pool size is much large (the top weld pool length is 15.7 mm in the numerical simulation), so the radiation area and radiation loss are increased. However, Pan et.al [16] calculated the radiation loss of the anode in the stationary KPAW process at 0.4 s, and the value was only 2.7 W. The reasons can be explained as following: In the moving KPAW process, the model is not axisymmetric, so a large three dimensional computation domain is used. The weld pool size in the moving KPAW process is much larger than that in the stationary KPAW process. Besides, the radiation loss at the bottom surface in this study is also considered.

The calculated arc efficiency for heating the anode in this study is only 60.7%, which is much lower than these in the GTAW [17] and GMAW [107] processes. Metcalfe et.al proposed that the efficiency of energy transfer to the anode was 60%~66% in a 10 kW plasma welding arc [43]. Evans et.al measured the arc efficiency in the variable polarity plasma arc welding of 6061 aluminum alloy, and found that when the current was 110 A, and voltage was 32 V, the arc efficiency was about 60% [120]. As discussed above, the calculated arc efficiency in our study is reasonable. In the KPAW process, the arc size is large, and the arc temperature is high, so the conduction energy loss and radiation loss of the plasma arc are high. It should be noted that multiple reflections and Fresnel absorption by the keyhole do not happen in the KPAW process. Actually, due to the formation of the penetrated keyhole, the energy is dissipated from the efflux arc. The conduction energy loss from the efflux arc to the bottom surface of the computation domain is calculated, and its value is 341.4 W, which accounts for 11.5% of the arc energy.

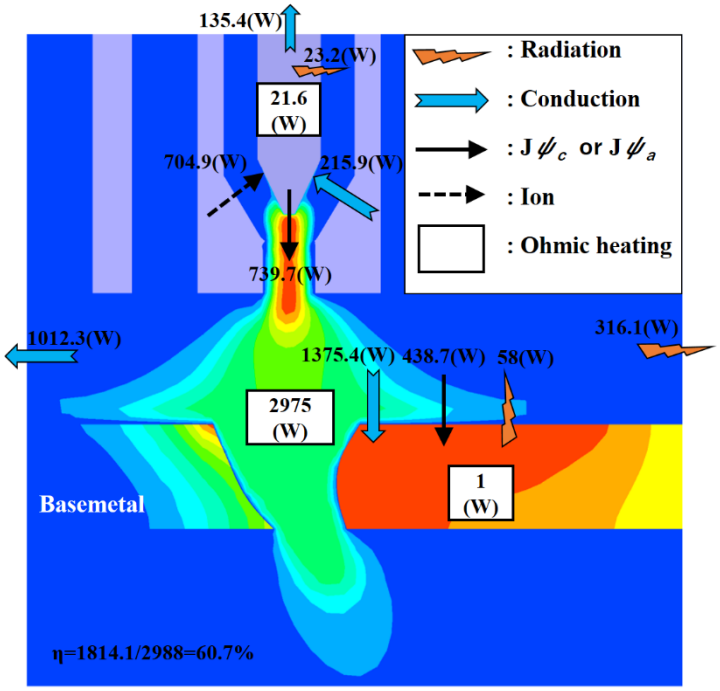

Fig. 4.12 The energy balance in the KPAW process

4.4.4 Validation of the numerical simulation

Fig. 4.13 shows the convective patterns of the weld pool based on previous high speed X-ray and high speed video camera results [35]. It can be seen that two convective eddies exist inside the weld pool: a clockwise eddy at the top part of the weld pool and an anti-clockwise eddy at the bottom part of the weld pool. At the top weld pool surface, the molten metal flows upward and backward. At the bottom weld pool surface, the molten metal flows downward and backward. The calculated convective patterns agree well with experimental results.

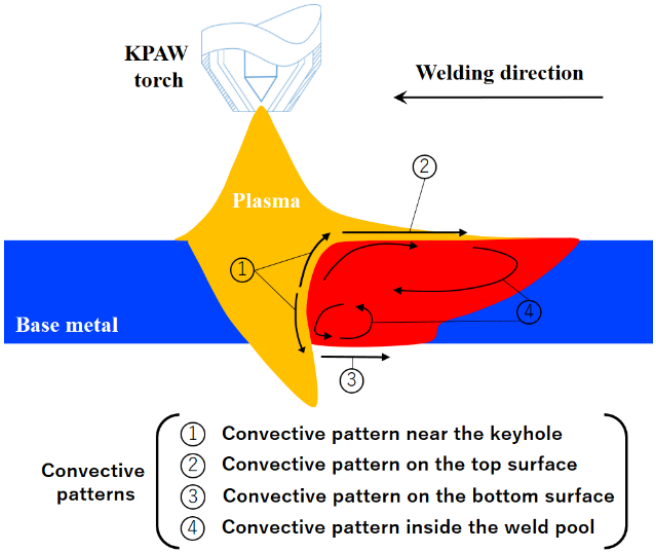

Fig. 4.13 The convective patterns of the weld pool based on the previous high speed X-ray and high speed video camera results

Based on the observation of the thermal camera in our previous study [19], the maximum temperature of the weld pool in the KPAW process is about 1875 K when the welding current is 120 A. It can be concluded that the maximum temperature of the weld pool is in the range of 1697 K~1875 K when the welding current is 90 A. In this study, the calculated maximum temperature is about 1857 K.

As shown in **Fig. 4.14**, in the simulation, the weld widths on the top and bottom surfaces are 6.33 mm and 1.67 mm, respectively. In the experiment, the weld widths on the top and bottom surface are 5.67 mm and 1.70mm, respectively. The calculated weld geometry is basically in agreement with the experimental result. It should be noted that the weld width at the top surface obtained by the numerical simulation is larger than that obtained by experiment, which may be caused by the overlook of undercut formation.

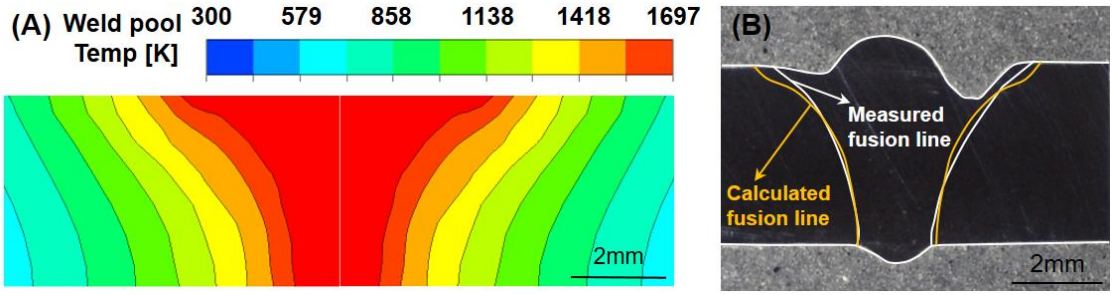

Fig. 4.14 (A) The calculated weld pool at the transverse cross section (B) The comparison of calculated and experimental weld profiles at the transverse cross section

As discussed above, the calculated the convective patterns of the weld pool and at the weld pool surfaces, maximum weld pool temperature, weld geometry and energy efficiency are in good agreement with our and previous experiment results.

4.5 Conclusions

In this study, a novel fully coupled plasma arc-keyhole-weld pool model is developed to investigate the energy propagation when the weld pool reaches the quasi-steady state in the KPAW process. The conclusions can be summarized as follows:

(1) The conduction energy flux, electric energy flux and total energy flux from the arc to the top weld pool are larger than these from the arc to the bottom weld pool. The maximum conduction energy flux and maximum electric energy flux are similar, while the distribution area of the conduction energy flux is much larger. As a result, the conduction energy from the arc to the anode is much higher than the electron condensation heating.

(2) The energy convection caused by the fluid flow is the dominant mechanism for energy propagation in the weld pool in the KPAW process. Under the influence of the arc pressure and plasma shear stress, two dominant convective eddies exist inside the weld pool.

(3) In the KPAW process, the arc size is large, and the arc temperature is high, so the conduction energy loss and radiation loss of the plasma arc are high. The keyhole formation can’t increase the energy absorption, and 11.5% of the arc energy are lost by the efflux arc. The calculated energy efficiency for heating the anode in this study is only 60.7%.

Chapter 5 Interactive phenomena in the hybrid KPAW-P-GMAW process

5.1 Introduction

In order to suppress weld defects and improve the weld bead formation of keyhole plasma arc welding (KPAW), paraxial hybrid keyhole plasma arc welding and gas metal arc welding (KPAW-GMAW) is proposed by many researchers [11,12], by which carbon steel plates with the thickness of 12 mm can be successfully welded with only one pass [11]. In this welding process, the plasma torch is located at the leading direction, and the tungsten electrode is the cathode. The GMAW torch is located at the rearing direction, and the welding wire is the anode.

As is known to all, pulsed-GMAW, especially one pulse one drop (OPOD) metal transfer mode, is capable of reducing spatters and stabilizing the GMA [121]. However, the welding parameter range for getting the stable OPOD mode is very narrow [122,123]. In this study, the paraxial hybrid KPAW-P-GMAW was carried out, and the stable OPOD mode was obtained. During the welding, the arc and droplet behaviors, keyhole and weld pool were observed by a high speed video camera (HSVC). The fluid flow of the weld pool was measured with the help of Zirconia particles. The weld pool temperature was measured by a thermal camera. Based on the observation of the complicated interactive phenomena of the arc, droplet, keyhole and weld pool in the hybrid KPAW-P-GMAW, the influences of arc interference and keyhole behaviors on the droplet transfer were discussed. The convective patterns in the weld pool and their driven forces were revealed. The interesting thermo-physical phenomenon that even though the heat input was much higher, the maximum temperature of the weld pool in the hybrid KPAW-P-GMAW was lower in comparison with the P-GMAW, was also explained.

5.2 Experimental procedures

The welding experimental setup is shown in **Fig. 5.1**. A transfer-type plasma arc welding torch (100WH, Nippon Steel Welding & Engineering Co., Ltd.), a KPAW power

source (NW-300ASR, Nippon Steel Welding & Engineering Co., Ltd.), a GMAW power source (DP 350, Daihen Co., Ltd) and a wire feeder (CM-7401, Daihen Co., Ltd) were used as the welding equipment. Carbon steel plates with the thickness of 12 mm (SS400) were used as the base metal. A constant current was adopted for the KPAW, and the pulsed mode was adopted for the GMAW. Detailed welding parameters can be seen in **Table. 5.1**.

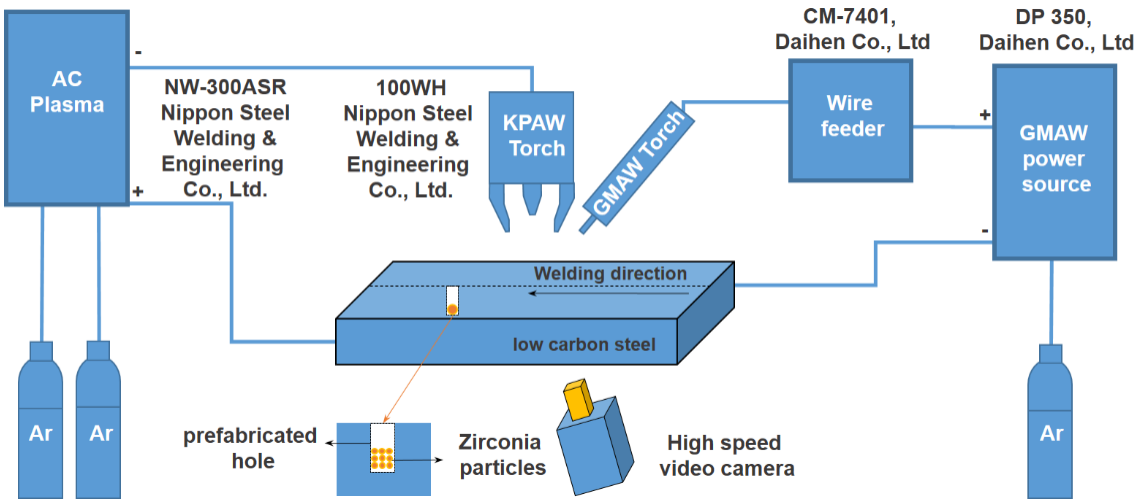

Fig. 5.1 The welding experiment setup of the hybrid KPAW-P-GMAW

Table. 5.1 Detailed welding parameters

KPAW torch orifice diameter	KPAW electrode diameter	KPAW electrode setback	KPAW torch and GMAW torch distance	GMAW torch angle	Welding wire diameter	CTWD (KPAW)
4.0 mm	4.8 mm	3 mm	22 mm	70°	1.2 mm	5 mm
CTWD (GMAW)	Welding speed	Plasma gas flow rate (Ar)	KPAW shielding gas flow rate (Ar)	GMAW shielding gas flow rate (Ar)	KPAW current	Wire feed rate
15 mm	3 mm/s	2.5 l/min	10 l/min	15 l/min	DC280 A	5.8 m/min

During the welding, the current waveform of the GMAW was measured by a clamp meter, and sent to a data logger with a frequency of 1MHz. The arc and droplet behaviors were observed by the HSVC, and the frame rate was 2000 frame/s. In order to measure the fluid flow of the weld pool, before the welding, the Zirconia particles were put into prefabricated holes in the base metal. During the welding, the movement of the Zirconia

particles on the top weld pool surface was measured by the HSVC with a frame rate of 2000 frame/s. A thermal camera (Miro Ex4 Phantom, Vision research Inc.) including three color sensors composed of Red (R), Green (G) and Blue (B) was adopted to obtain the weld pool surface images immediately after switching off the arcs. The weld pool temperatures can be calculated from the ratio of the R sensor signal to the G sensor signal in the images based on the two color pyrometry method. It should be noted that the arcs completely disappear within 1.0 ms after switching off the arcs, so the surface temperature decrease can be ignored [20]. Detail descriptions of the observation and measurement methods can be seen in our previous work [35]. For the P-GMAW and hybrid KPAW-P-GMAW, the temperatures of the weld pools were obtained after the droplet transfer in the base current stage.

5.3 Results

5.3.1 Arc and droplet behaviors in the hybrid process

The current waveform, arc and droplet behaviors in the hybrid KPAW-P-GMAW are shown in **Fig. 5.2**. In the peak current stage, both the PA and GMA are very bright. Two arcs connect, and a direct current path forms between the KPAW cathode (tungsten electrode) and GMAW anode (welding wire) through the arc plasma, as shown in **Fig. 5.2(A)**. In the current decrease stage, two arcs separate, and the arc interference becomes weak, as shown in **Fig. 5.2(B)**. At the end of the current decrease stage, as shown in **Fig. 5.2(C)**, the GMA is still bright near the wire axis, while very weak far from the wire axis. In the base current stage, as shown in **Fig. 5.2(D)**, the GMA is rather weak, and a globular droplet is detached from the tip of the welding wire. In **Fig. 5.2(E)**, the droplet almost arrives at the top surface of the weld pool. The average current in the hybrid KPAW-P-GMAW is 170.1 A. In summary, the stable OPOD mode can be obtained in the hybrid KPAW-P-GMAW. The arc interference is strong only in the peak current stage.

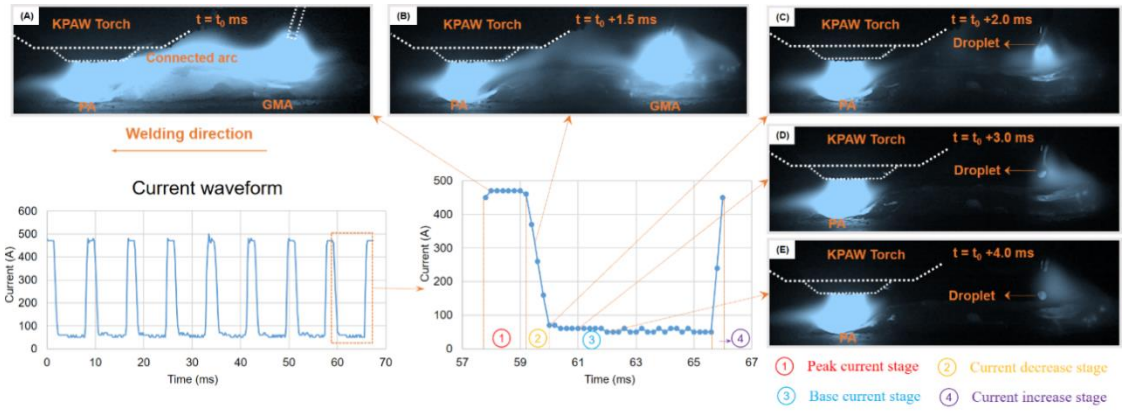

Fig. 5.2 The current waveform, arc and droplet behaviors in the hybrid KPAW-P-GMAW

The current waveform, arc and droplet behaviors in the P-GMAW are shown in **Fig. 5.3** and **Fig. 5.4**. Two droplet transfer modes are observed: globular transfer mode, and short circuit transfer mode.

As shown in **Fig. 5.3**, in the peak current stage, the GMA is very bright. In the current decrease stage, the arc length and width decrease. In the base current stage, a globular droplet is transferred. The average current in the P-GMAW is 157 A.

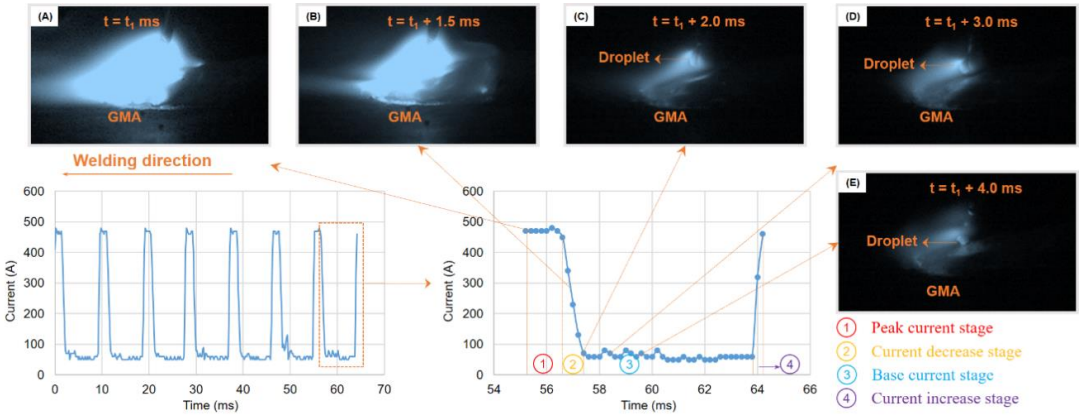

Fig. 5. 3 The current waveform, arc and droplet behaviors in the P-GMAW

As shown in **Fig. 5.4**, the GMA length is small. When a globular droplet is almost detached from the tip of the welding wire, it contacts the weld pool, and the GMA is extinguished.

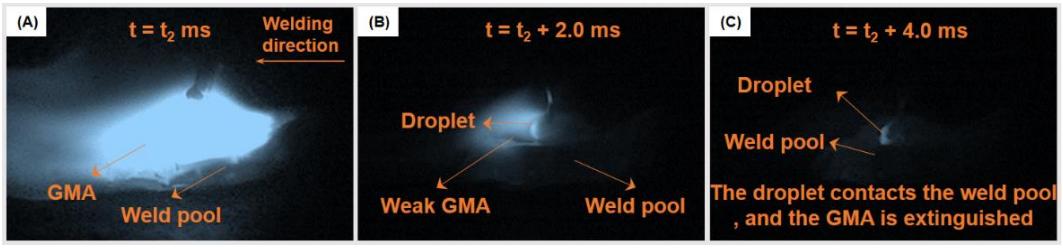

Fig. 5. 4 The short circuit transfer mode in the P-GMAW

Here, the wire extension length (L_1) and arc length (L_2) are presented based on statistics of several pulse periods. It can be seen from **Fig. 5.5** that the wire extension length in the hybrid KPAW-P-GMAW and P-GMAW (globular transfer mode) is 5.4 mm and 7.1 mm, respectively. The arc length in the hybrid KPAW-P-GMAW and P-GMAW (globular transfer mode) is 7.1 mm and 6.4 mm, respectively. In summary, the wire extension length is shorter, while the average arc length is larger in the hybrid KPAW-P-GMAW.

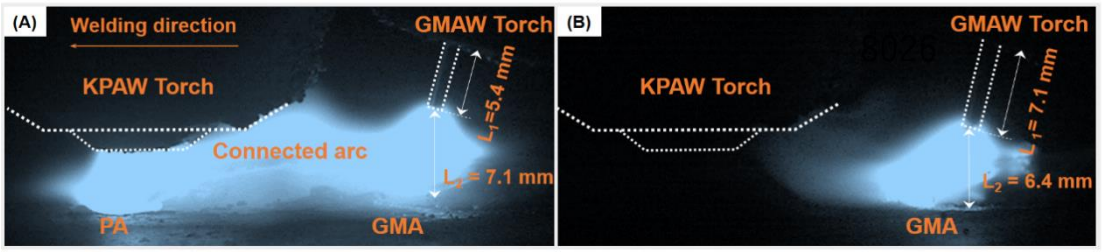

Fig. 5.5 Comparisons of arcs in the hybrid KPAW-P-GMAW process and P-GMAW

The droplet diameter, droplet velocity and droplet transfer frequency are shown in **Fig. 5.6** based on statistics of several pulse periods. The droplet diameter (D) in the hybrid KPAW-P-GMAW and P-GMAW (globular transfer mode) is 1.14 mm and 1.22 mm, respectively. The droplet velocity (V) in the hybrid KPAW-P-GMAW and P-GMAW (globular transfer mode) is 1.16 m/s mm and 0.69 m/s, respectively. The transfer frequency (f) in the hybrid KPAW-P-GMAW and P-GMAW (globular transfer mode) is 119 Hz and 107 Hz, respectively. In summary, the droplet velocity and droplet transfer frequency increase, while the droplet diameter decrease in the hybrid KPAW-P-GMAW.

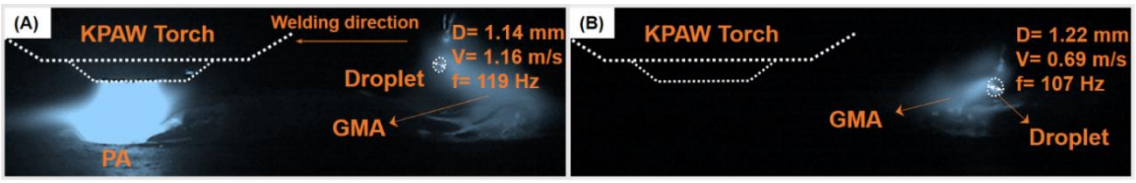

Fig. 5. 6 Comparisons of droplet behaviors in the hybrid KPAW-P-GMAW and P-GMAW

5.3.2 Convective patterns in the hybrid process

As shown in **Fig. 5.7(A)**, in the base current stage, a particle cluster can be seen on the top surface near the PA, and the distance from the PA center is 7.28 mm. In the peak current stage, as shown in **Fig. 5.7(B)**, two arcs connect. In the current decrease stage, it can be seen from **Fig. 5.7(C)** that the particle cluster flows away from the PA, and the distance from the PA center is 7.93 mm. As time goes on, as shown in **Fig. 5.7(D)**, **(E)**

and **(F)** that the distance between the particle cluster and PA center increases. In summary, the molten metals on the top surface near the PA flow backward in the hybrid KPAW-P-GMAW.

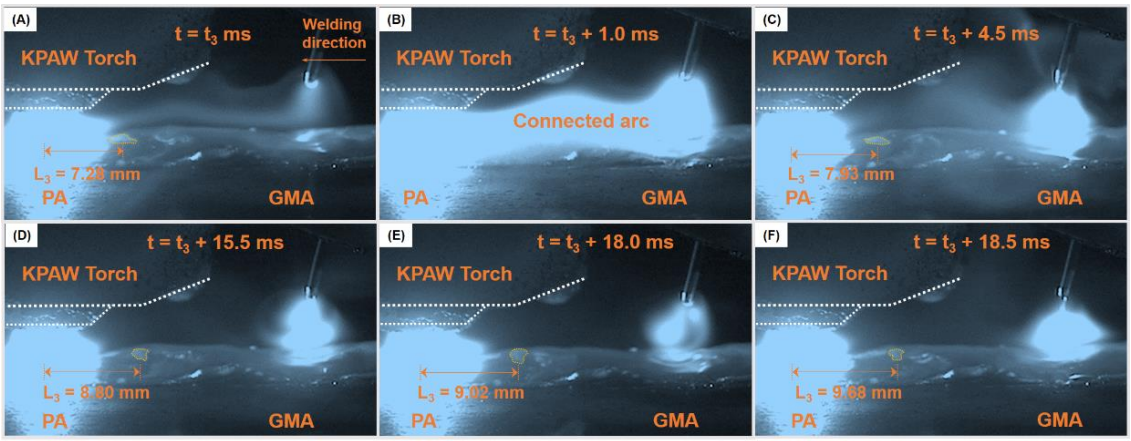

Fig. 5. 7 Convective patterns on the top surface near the PA

As shown in **Fig. 5.8(A)**, in the base current stage, a particle cluster can be seen on the top surface before the GMA, and the distance from the welding wire center is 5.38 mm. After the peak current stage (as shown in **Fig. 5.8(B)**), the particle cluster flows forward, and the distance from the welding wire center is 7.20 mm, as shown in **Fig. 5.8(C)**. In the base current stage, as shown in **Fig. 5.8(D)**, the particle cluster flows backward, and the distance from the welding wire center decreases. After next two periods, as shown in **Fig. 5.8(E)~(I)**, the particle cluster flows forward. At last, the particle cluster stops at the weld pool side.

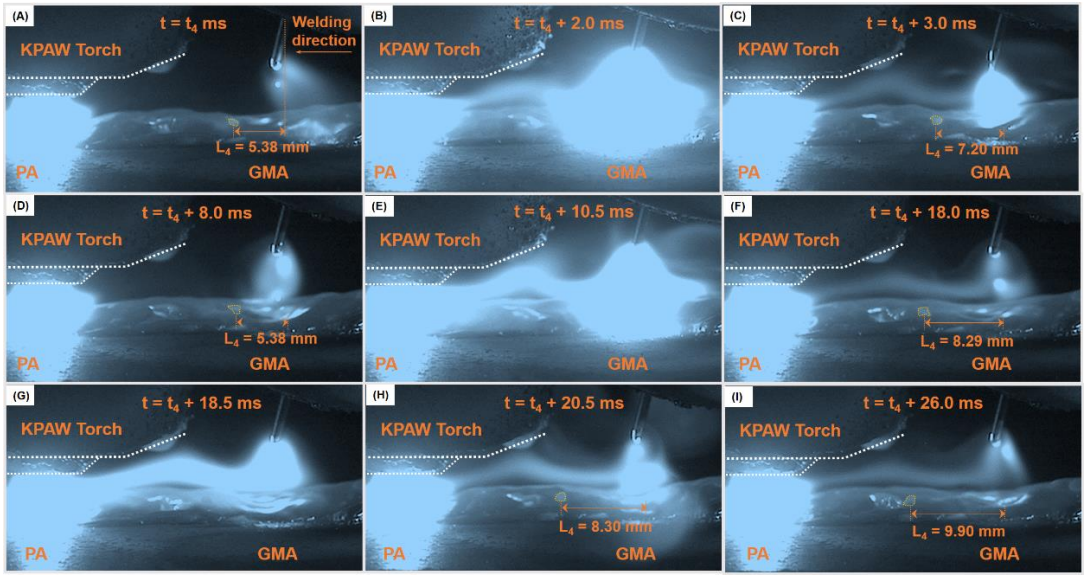

Fig. 5.8 Convective patterns on the top surface before the GMA

As shown in **Fig. 5.9(A)**, in the current decrease stage, three particles can be seen on the top surface after the GMA. In the base current stage, the distances between the particles and welding wire center increase, as shown in **Fig. 5.9(B)**. In next period, it can be seen from **Fig. 5.9(C)** and **(D)** that the particles flow backward, and then arrive at the rear part of weld pool. It can be concluded that the molten metals after the GMA mainly flow backward in the hybrid KPAW-P-GMAW.

The convective patterns in the P-GMAW and KPAW can be seen in previous studies. The convective patterns on the top surface in the P-GMAW are similar to these in **Fig. 5.9** [124], and the convective patterns on the top surface in the KPAW are similar to these in **Fig. 5.7** [10].

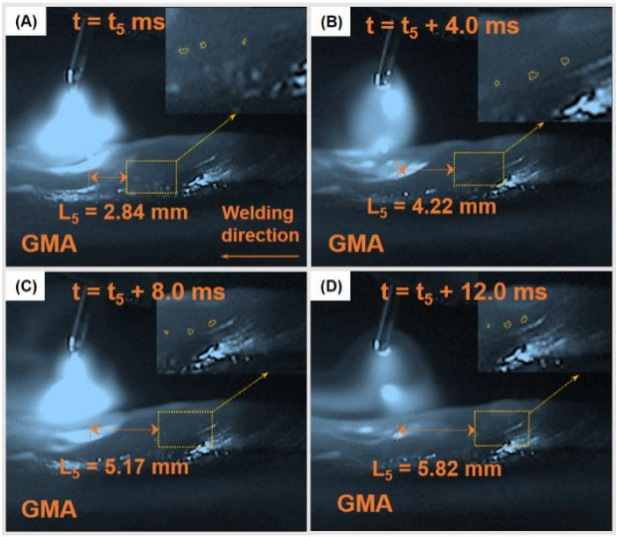

Fig. 5.9 Convective patterns on the top surface after the GMA

5.3.3 The temperature distribution and weld bead formation in the hybrid process

As shown in **Fig. 5.10**, in the hybrid KPAW-P-GMAW, a high temperature region can be seen near the GMA, and the maximum temperature is 2489 K. In the P-GMAW, the maximum temperature near the GMA is 2584 K, and high temperature regions can also be seen at the rear part of the weld pool. It can also be seen from **Fig. 5.10** that even though the welding current in the KPAW is very high, the maximum temperature of the weld pool is only 2259 K, which is much smaller than these in the hybrid KPAW-P-GMAW and P-GMAW.

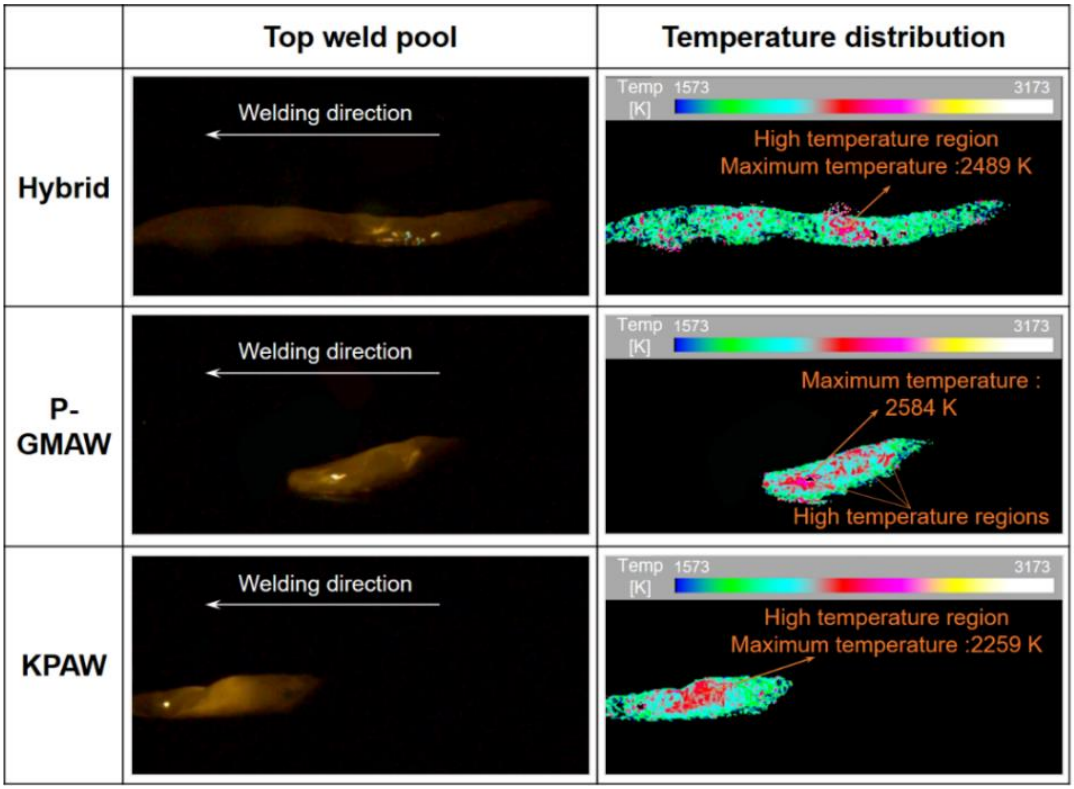

Fig. 5.10 The weld pool temperature distributions in the hybrid KPAW- P-GMAW, P-GMAW and KPAW

In the hybrid KPAW-P-GMAW, as shown in **Fig. 5.11(A)**, sound weld bead formation can be obtained. In the P-GMAW, the weld width is narrow, and the reinforcement is high. In the KPAW, undercut forms at the weld toe.

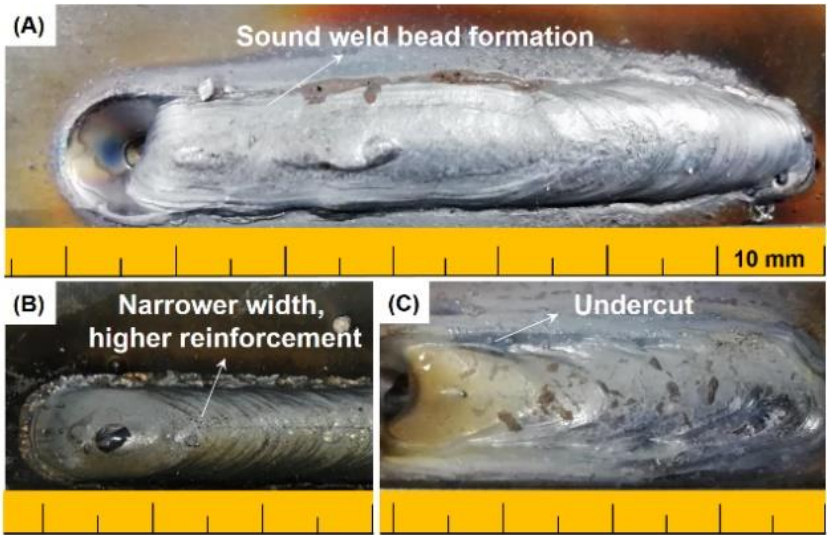

Fig. 5.11 The weld bead formation: (A) Hybrid KPAW-P-GMAW; (B) P-GMAW; (C) KPAW

5.4 Discussion

5.4.1 Influences of arc interference and keyhole behaviors on the droplet transfer

Even though both the hybrid Laser-P-GMAW and hybrid KPAW-P-GMAW are characterized by the complex interaction of the arc, droplet, keyhole and weld pool, the influences of arc interference and keyhole behaviors on the droplet transfer in these two welding processes are totally different. In the hybrid Laser-P-GMAW, the maximum weld pool temperature on the keyhole wall is higher than the boiling temperature of the material, and large amount of metal vapor is produced. As shown in **Fig. 5.12(A)**, the metal vapor ejected from the keyhole produces a resistant force on the droplet [72]. Besides, owing to the arc contraction caused by the strong laser plasma, the current at the droplet is converged. Based on Eq. (5.1) [125], the electromagnetic resistant force of the droplet transfer increases [73]. All of these reasons contribute to the suppression of the droplet transfer in the hybrid Laser-P-GMAW.

$$F_{emz} = -\frac{\mu_0 I^2}{4\pi}\left[\frac{1}{4} - ln\left(\frac{r_d sin\theta}{r_w}\right) + \frac{1}{1-cos\theta} - \frac{2}{(1-cos\theta)^2} ln\left(\frac{2}{1+cos\theta}\right)\right] \quad (5.1)$$

where I is the welding current, r_d is the droplet radius, r_w is the wire radius, θ is the arc hanging angle and μ_0 is the permeability of free space.

Detailed comparisons of arc, droplet and keyhole behaviors between the hybrid Laser-P-GMAW and hybrid KPAW-P-GMAW can be seen in Table. 5.2. In the hybrid KPAW-P-GMAW, the maximum weld pool temperature is only 2259 K, which is much lower than the boiling temperature of the material (2900 K), so the metal vapor ejected from the keyhole can be ignored, and the metal vapor jet force has a minor influence on the droplet transfer. Owing to the formation of a direct current path between the KPAW cathode (tungsten electrode) and GMAW anode (welding wire), the ionized PA is extended to the GMA side. Based on the minimum voltage principle, an arc has an automatic dropping tendency to drive the electric field intensity **E** to the minimum value [126]. As the GMA is heated by the PA, it will automatically expand, and the cross section area of the GMA increases. Therefore, the current density decreases, and the electric field intensity **E** has the maximum reduction. As shown in **Fig. 5.12(B)**, the current at the GMAW droplet is diverged, and the Lorenz force acts as a detachment force, so the droplet velocity and droplet transfer frequency increase, and the droplet diameter

decreases in the hybrid KPAW-P-GMAW in comparison with the P-GMAW. As a result, the wire extension length is shorter, and the arc length and width are larger in the hybrid KPAW-P-GMAW in comparison with the P-GMAW. In summary, the coupled arcs improve stability of the OPOD metal transfer mode in the hybrid KPAW-P-GMAW.

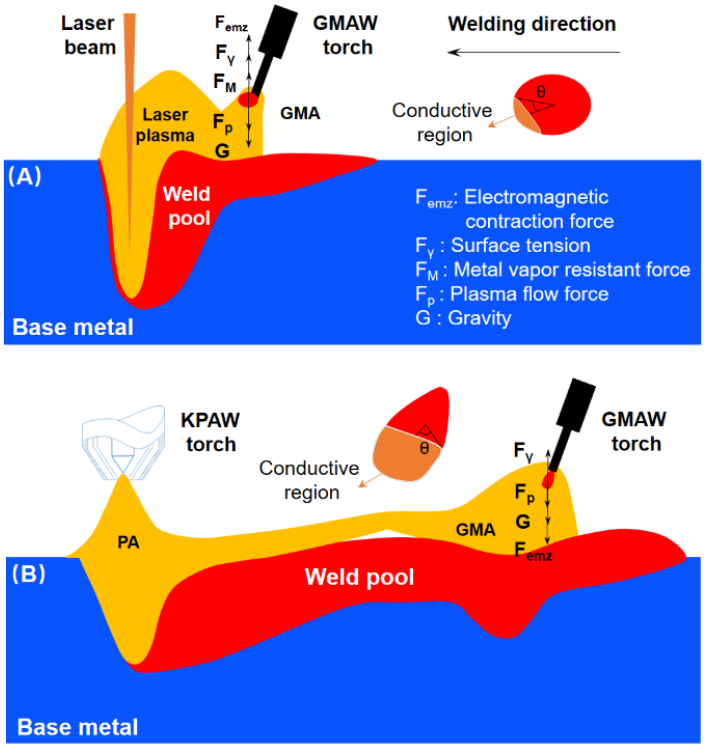

Fig. 5.12 Diagrams of the droplet transfer in the (A) Hybrid Laser-P-GMAW; (B) hybrid KPAW-P-GMAW

Table. 5.2 Comparisons of the arc, droplet and keyhole behaviors between the hybrid Laser-P-GMAW and hybrid KPAW-P-GMAW

	Keyhole temperature	Metal vapor	Metal vapor jet force effect	Arc behavior	GMAW current density	Lorenz force effect
Hybrid Laser-P-GMAW	High	Strong	Suppress droplet transfer	Arc contraction	Converged	Suppress droplet transfer
Hybrid KPAW-P-GMAW	Low	Weak	Minor influence	Arc expansion	Diverged	Promote droplet transfer

5.4.2 Interaction of the arc, droplet, keyhole and weld pool

Based on the convective patterns in the P-GMAW [124] and KPAW [10] in previous

studies, and our experimental results, the convective patterns on the weld pool surface and their driven forces in the hybrid KPAW-P-GMAW can be concluded in **Fig. 5.13**. The convective pattern 1 (backward flow) on the top surface near the PA is caused by the Marangoni force and PA shear stress. The convective pattern 2 (forward flow) on the top surface in the transition region is caused by the Marangoni force and GMA shear stress. The convective pattern 3 (inward flow) on the top surface near the GMA is caused by the arc pressure, Lorentz force and droplet impingement force. The convective pattern 4 (backward flow) on the top surface after the GMA is caused by the Marangoni force and GMA shear stress.

In the peak current stage, as shown in **Fig. 5.13(A)**, the GMA shear stress is large, so the convective pattern 2 (forward flow) on the top surface is strong, while the convective pattern 3 (inward flow) is relatively weak. If a particle P_1 locates at the action area of the convective pattern 2, it will flow forward, as shown in **Fig. 5.8(A)~(C)**. In the base current stage, as shown in **Fig. 5.13(B)**, the GMA shear stress, arc pressure and Lorentz force are all very small, so the convective pattern 2 becomes weaker. However, the strong droplet impingement will cause strong inward flow, so the convective pattern 3 becomes stronger. If a particle P_2 locates at the action area of the convective pattern 3, it will flow inward, as shown in **Fig. 5.8(C)~(D)**. If a particle P_3 locates at the action area of the convective pattern 2, it will also flow forward, as shown in **Fig. 5.8(H)~(I)**.

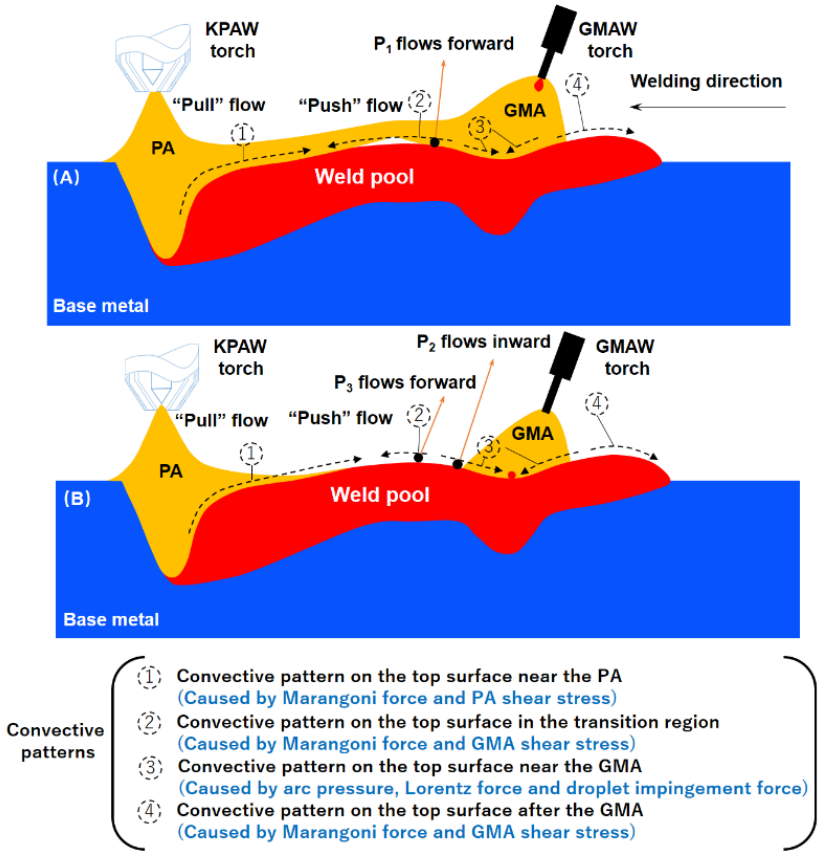

Fig. 5.13 Convective patterns on the top weld pool surface and their driven forces in the hybrid KPAW-P-GMAW: (A) Peak current stage; (B) Base current stage

Here, the convective pattern 1 (backward flow) is defined as "Pull" flow, and the convective pattern 2 (forward flow) is defined as "Push" flow. This "Pull-Push" flow pattern on the top weld pool surface between two arcs in the hybrid KPAW-P-GMAW is mainly caused by the Marangoni force and arc shear stress. This flow pattern was also found in the tandem P-GMAW [63], which prevented the irregular backward flow of molten metals, and facilitated sound weld bead formation. As revealed in the previous study, the strong backward flow was one of the most important factors for the undercut formation in the GTAW process [37]. Owing to the "Pull-Push" flow pattern in the hybrid KPAW-P-GMAW, the strong backward flow from the keyhole is suppressed, which is benefit for preventing the undercut formation, as shown in **Fig. 5.11**.

There is an interesting thermo-physical phenomenon that even though the heat inputs are much higher, the maximum weld pool temperatures in the hybrid KPAW-P-GMAW (2489 K) and KPAW (2259 K) are lower in comparison with the P-GMAW (2584 K). As revealed in our previous studies, in the KPAW, energy convection caused by the fluid flow

is the dominant mechanism for energy propagation in the weld pool. Owing to the much high plasma arc pressure and plasma arc shear stress, the fluid flow and energy propagation in the weld pool are strong. Energy is not accumulated on the keyhole, but transported to the whole weld pool together with the molten metal, causing the relatively low temperature distribution near the PA [35, 127]. As shown in **Fig. 5.14**, in the hybrid KPAW-P-GMAW, the weld pool temperature is lower in the region near the PA, and higher in the region near the GMA. Due to the "Pull-Push" flow pattern on the top weld pool surface between two arcs, the molten metals in the region near the GMA are transported to the region near the PA. As heat in the weld pool is transported from the high temperature region to low temperature region, the molten metal temperature near the GMA decreases. Besides, owing to the formation of the direct current path between the KPAW cathode (tungsten electrode) and GMAW anode (welding wire), the GMA expands, and the current density decreases. Therefore, GMA heat transported to the weld pool decreases. All of these mechanisms contribute to the lower maximum weld pool temperature in the hybrid KPAW-P-GMAW in comparison with P-GMAW, and the first mechanism is especially important, because the arc interference is strong only in the peak current stage.

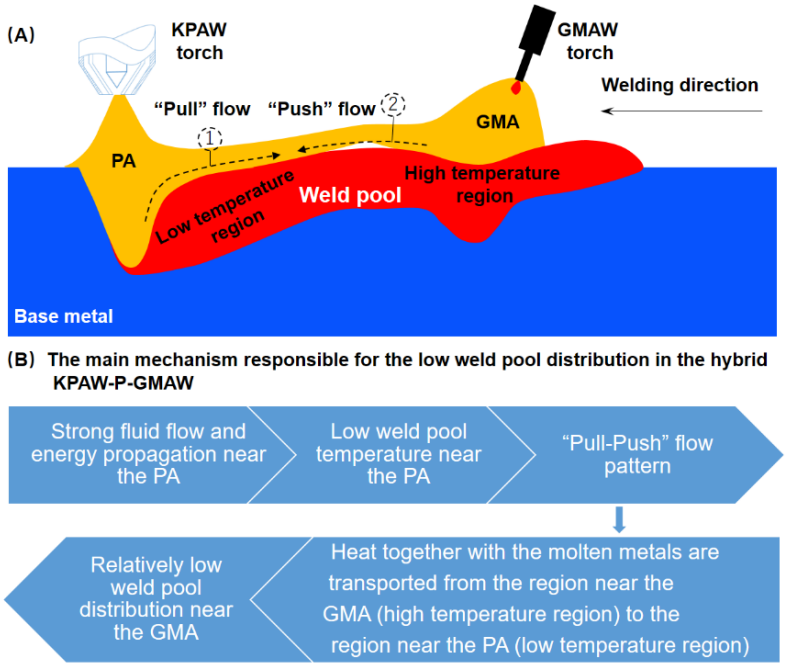

Fig. 5.14 (A) The diagram of the convective patterns and energy propagation on the top surface between two arcs; (B) The main mechanism responsible for the low weld pool distribution in the hybrid KPAW-P-GMAW

5.5 Conclusions

In this study, the complex interactive phenomena of arc, droplet, keyhole and weld pool in the hybrid KPAW-P-GMAW are analyzed with the help of a high speed video camera, Zirconia particles and a thermal camera. The conclusions can be summarized as follows:

(1) Owing to the formation of a direct current path between the KPAW cathode (tungsten electrode) and GMAW anode (welding wire) in the peak current stage, the ionized PA is extended to the GMA side. The wire extension length is shorter, and the arc length is larger in hybrid KPAW-P-GMAW in comparison with P-GMAW.

(2) The metal vapor from the keyhole has a minor influence on the droplet transfer, while the Lorenz force promotes the droplet transfer. The stable OPOD mode can be obtained in the hybrid KPAW-P-GMAW.

(3) The “Pull-Push” flow pattern caused by the Marangoni force and arc shear stress exists on the top weld pool surface between two arcs, which suppresses the strong backward flow from the keyhole.

(4) The interaction of the arc, droplet, keyhole and weld pool in the hybrid KPAW-P-GMAW promotes the fluid flow and heat transfer in the weld pool, which is benefit for decreasing the maximum weld pool temperature.

Chapter 6 Analysis of heat transfer and material flow in the hybrid KPAW-GMAW process based on a novel three dimensional CFD simulation

6.1 Introduction

Numerical simulation provides a scientific and effective way to analyze the heat transfer and material flow in the hybrid KPAW-GMAW process. Lots of studies had been carried out to investigate the weld pool convection in the KPAW process [35,127] and GMAW process [95,129,130], in which the heat source and arc pressure were introduced as the boundary conditions. It should be noted that in the hybrid KPAW-GMAW process, the interaction of the arc, keyhole and weld pool is very complex, and many interesting phenomena are observed. Nguyen et.al [11] measured the temperature distribution of the weld pool by the thermal camera, and found that the maximum temperature of the weld pool in the hybrid KPAW-GMAW process was higher than that in the conventional GMAW process. Han et.al [57] studied the arc coupling mechanism in the hybrid VPPAW-GMAW process, and suggested that the GMAW arc was compressed by the electromagnetic coupling characteristics. In order to accurately predict the heat transfer and material flow in the hybrid KPAW-GMAW process, the complicated interactive phenomena should be considered in the numerical model.

In this study, the hybrid KPAW-GMAW process is carried out: the KPAW arc is ignited firstly, then the GMAW arc is ignited. A high speed video camera (HSVC) is used to observe the arc, droplet, keyhole and weld pool. A thermal camera is used to measure the temperature of the droplet and weld pool. For the first time, a novel three dimensional numerical model considering the complicated interactive phenomena is developed for the hybrid KPAW-GMAW process. The heat transfer and material flow in the weld pool is analyzed in detail.

6.2 Experimental method

As shown in **Fig. 6.1**, a transfer-type plasma arc welding torch (100WH, Nippon Steel Welding & Engineering Co., Ltd.), and a welding power source (NW-300ASR, Nippon Steel Welding & Engineering Co., Ltd.) are used as the welding equipment. The

low carbon steel plates (SS400) with a thickness of 12 mm are used as the base metal. The diameter of the KPAW torch orifice is 4.0 mm. The diameter of the KPAW electrode is 4.8 mm, and the tip radius is 1.0 mm. The KPAW electrode setback is 3 mm. The distance between the KPAW nozzle and the base metal is 5 mm. The distance between the KPAW torch and GMAW torch is 22 mm. The GMAW torch angle is 70°. The diameter of the welding wire is 1.2 mm, and the contact–tip-to-work (CTWD) of the GMAW is 15 mm. The welding speed is 3 mm/s. The pure Ar is used as the main plasma gas and shielding gas. The main plasma gas flow rate is 2.5 l/min. The shielding gas flow rates of the KPAW and GMAW are 10 l/min and 15 l/min, respectively. The welding currents of the KPAW and GMAW are DC265 A and DC230 A, respectively. The welding voltages of the KPAW and GMAW are 25.2 V and 26.4V, respectively. The same welding parameters are used in the numerical simulation. During the welding, the KPAW arc is ignited firstly, then the GMAW arc is ignited.

The arc behaviors are observed by a HSVC, and the frame rate is 2000 fps. In order to clearly observe the droplet transfer, keyhole and weld pool behaviors, a band pass filter with the wavelength of 500 nm and bandwidth of 10 nm is attached in front of the HSVC, and the welding zone is illuminated by a diode laser.

The temperature of the droplet and weld pool are measured by a thermal camera (Miro Ex4 Phantom, Vision research Inc.) immediately after switching off the arc. The thermal camera includes three color sensors composed of Red (R), Green (G) and Blue (B), and the temperature is calculated from the ratio of the R sensor signal to the G sensor signal in the image based on the two color pyrometry method. The arc completely disappears within 1.0 ms after cutting the arc, so the decrease of the surface temperature can be ignored [20]. When the KPAW arc is ignited, the arc will be cut off, and the temperature of the weld pool will be measured. After several trials, the heat transfer of the weld pool at different time in the KPAW process can be obtained. During the hybrid KPAW-GMAW process, two arcs will be cut off, and the temperature of the weld pool will be measured. This “Sudden Stop Test” method [54] can provide in-depth knowledge of the heat transfer in the KPAW-GMAW process.

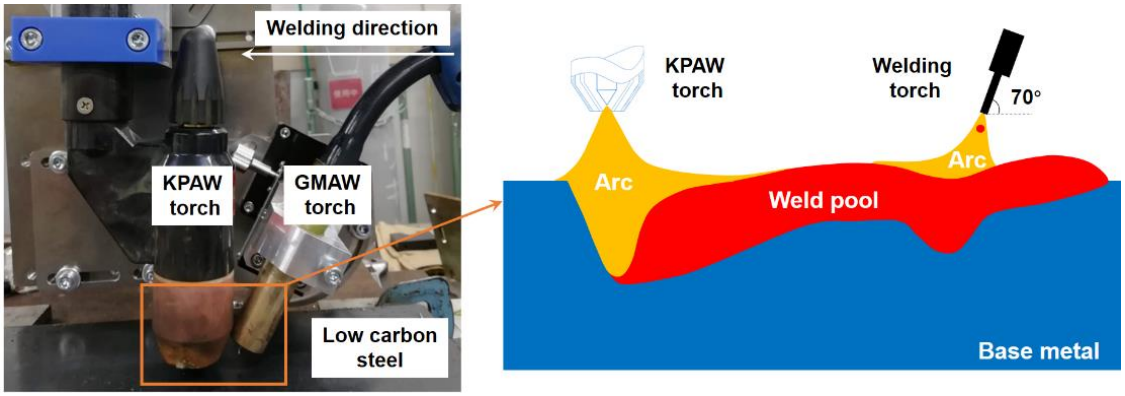

Fig. 6.1 The welding experiment setup

6.3 Mathematical model and numerical simulation

Fig. 6.2 shows the modelling process of the hybrid KPAW-GMAW process. The arc modelling is firstly carried out to obtain the important simulation parameters related to the heat source, arc pressure, arc shear stress and electromagnetic force. Then, based on the high speed photographs of the arcs, the heat source model, arc pressure model, arc shear stress model and electromagnetic force model considering the interaction of the arc, keyhole and weld pool are developed, which are adopted as boundary conditions and body force source term in the weld pool modelling.

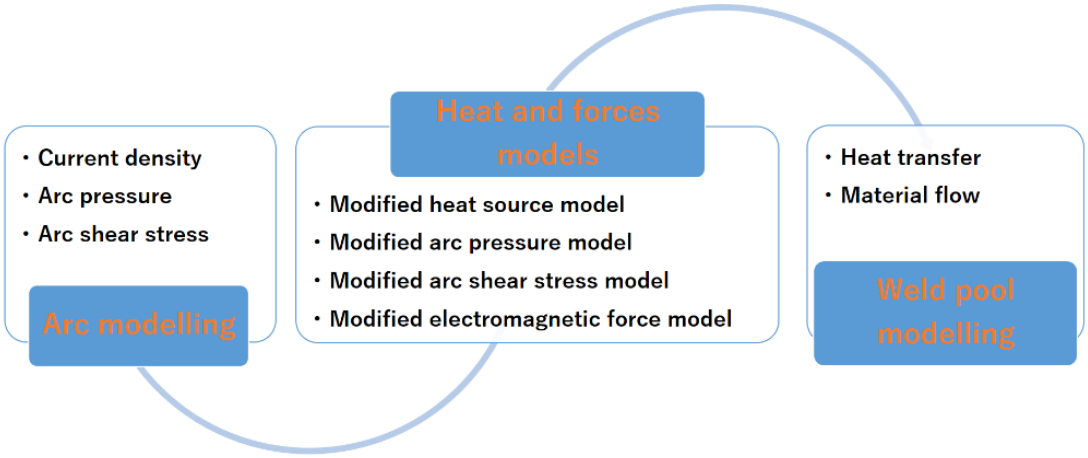

Fig. 6.2 The modelling process of the hybrid KPAW-GMAW process

In this one way coupled electrode-arc-droplet-weld pool model, the important simulation parameters related to the heat and forces are obtained from two dimensional steady-state arcs. **Fig. 6.3** shows the two dimensional axisymmetric computation domains of the KPAW arc and GMAW arc. The widths of the computation domains are 0.015 m. Outside the computational domains, the heat and forces are very small, and can be ignored. The droplet transfer is ignored, and the wire with radius 0.6 mm is used in the GMAW

arc model. The detail information of the KPAW and GMAW arc models can be seen in our previous works [25, 26].

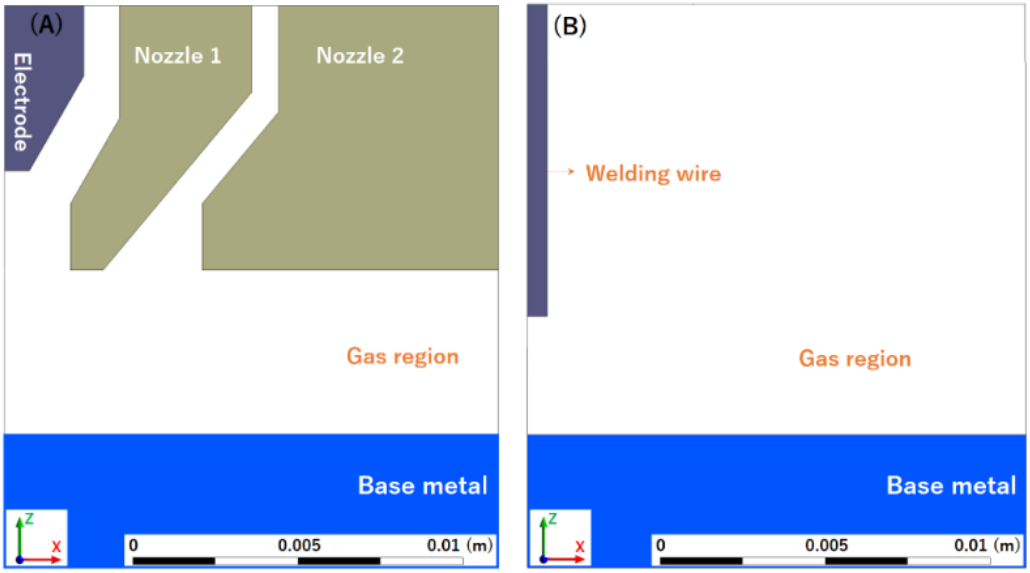

Fig. 6.3 The computation domains: (A) KPAW arc; (B) GMAW arc

As for the weld pool simulation, some assumptions are made in the numerical model: (1) The plasma gas and shielding gas are ignored, and the "void region" with uniform pressure and temperature is introduced to represent the region occupied by the gas. (2) The spherical shape droplets with constant radius, height, temperature, frequency and velocity are introduced to consider the droplet impingement. (3) The flow of the weld pool is laminar, and the molten metal is considered as an in-compressible Newtonian fluid. (4) The metal evaporation of the weld pool is omitted. In our previous study, the measured maximum temperature of the weld pool in the hybrid KPAW-GMAW process was about 2260 K [11], which was much lower than the boiling temperature of the carbon steel (2900 K).

The governing equations (mass, momentum, energy conservation equations, and VOF (Volume of Fluid) equation), boundary conditions and driven forces of the weld pool are discussed in the "Mathematic model". The detail information of the computation domain is discussed in the "Numerical simulation".

6.3.1 Mathematic model

6.3.1.1 Governing equations

Mass conservation equation:

$$\nabla \cdot \vec{V} = \frac{\dot{m}_s}{\rho} \tag{6.1}$$

where $\vec{V}$ is the velocity vector, $\dot{m}_s$ is the mass source term of the droplet, and ρ is the density.

Momentum conservation equation:

$$\frac{\partial \vec{V}}{\partial t} + \vec{V} \cdot \nabla \vec{V} = -\frac{\nabla P}{\rho} + \frac{v}{\rho}\nabla^2 \vec{V} - K\vec{V} + \frac{\dot{m}_s}{\rho}\left(\vec{V_s} - \vec{V}\right) + f_b \tag{6.2}$$

where t is the time, P is the pressure, v is the dynamic viscosity, K is the drag coefficient for a porosity media model [130], $\vec{V_s}$ is the velocity vector for the mass source, and f_b is the body force.

Energy conservation equation:

$$\frac{\partial h}{\partial t} + \vec{V} \cdot \nabla h = \frac{1}{\rho}\nabla \cdot (k\nabla T) + \dot{h_s} \tag{6.3}$$

where $h = \begin{cases} \rho_s C_s T & T < T_s \\ h(T_s) + h_{sl}\frac{T-T_s}{T_l-T_s} & T_s \leq T \leq T_l \\ h(T_l) + \rho_l C_l (T - T_l) & T > T_l \end{cases}$

where h is the enthalpy, k is the thermal conductivity, T is the temperature, $\dot{h_s}$ is the enthalpy source term owing to the mass source, ρ_s is the solid density, ρ_l is the liquid density, Cs is the specific heat of solid, C_l is the specific heat of liquid, T_s is the solidus temperature, T_l is the liquidus temperature, and h_{sl} is the latent heat of fusion.

VOF equation:

$$\frac{\partial F}{\partial t} + \nabla \cdot \left(\vec{V}F\right) = \dot{F_s} \tag{6.4}$$

where F is the volume fraction of fluid, and $\dot{F_s}$ is the volume fraction source term due to the mass source.

6.3.1.2 Boundary conditions

For the top free surface, the KPAW arc heat flux, GMAW arc heat flux, heat loss by convection and radiation are considered in the energy boundary condition, as shown in Eq. (6.5). The KPAW arc pressure, GMAW arc pressure and surface tension induced pressure are applied on the momentum boundary condition at the normal direction, as shown in Eq. (6.6). The KPAW arc shear stress, GMAW arc shear stress and Marangoni shear stress are applied on the momentum boundary condition at the tangential direction, as shown in Eq. (6.7).

$$k\frac{\partial T}{\partial \vec{n}} = q_{\mathrm{KPAW}} + q_{\mathrm{GMAW}} - h_{con}(T - T_0) - \varepsilon_r \alpha (T^4 - {T_0}^4) \quad (6.5)$$

$$-P + 2\mu\frac{\partial \overrightarrow{V_n}}{\partial \vec{n}} = -P_{\mathrm{KPAW}} - P_{\mathrm{GMAW}} + \frac{\gamma}{R_c} \quad (6.6)$$

$$-\mu\frac{\partial \overrightarrow{V_t}}{\partial \vec{n}} = \tau_{\mathrm{KPAW}} + \tau_{\mathrm{GMAW}} + \tau_m \quad (6.7)$$

where $\vec{n}$ is the normal vector of the top free surface, q_{KPAW} is the KPAW arc heat flux, q_{GMAW} is the GMAW arc heat flux, h_{con} is the convective heat transfer coefficient (20 W m^{-2} K^{-1}), T_0 is the ambient temperature, ε_r is the surface radiation emissivity, α is the Stefan-Boltzmann constant, μ is the fluid viscosity, $\overrightarrow{V_n}$ is the normal fluid velocity, P_{KPAW} is the KPAW arc pressure, P_{GMAW} is the GMAW arc pressure, γ is the surface tension, R_c is the surface curvature radius, $\overrightarrow{V_t}$ is the tangential fluid velocity, τ_{KPAW} is the KPAW arc shear stress, τ_{GMAW} is the GMAW arc shear stress, and τ_m *is* the Marangoni shear stress.

As for other external surfaces, the wall boundary conditions are used, and no heat flux and forces from the arc are implemented.

6.3.1.3 Droplet model

The spherical shape droplets are introduced in the simulation. **Fig. 6.4** shows the high speed photographs of droplet and weld pool. The average droplet radius 0.65 mm, average droplet height 3.0 mm, average droplet velocity 0.3 m/s are used in the simulation. As shown in **Fig. 6.5**, the average droplet temperature 2314 K is used. The average droplet frequency f_d, energy transfer by the droplet q_d and droplet energy efficiency η_d can be calculated [117]:

$$f_d = \frac{3r_w^2 WFR}{4r_d^3} \quad (6.8)$$

$$q_d = \frac{4}{3}\pi r_d^3 \rho[C_s(T_s - T_0) + C_l(T_d - T_l) + h_{sl}]f_d \quad (6.9)$$

$$\eta_d = \frac{q_d}{U_G I_G} \quad (6.10)$$

where r_w is the wire radius, *WFR* is the wire feed rate, r_d is the droplet radius, T_d is the droplet temperature, U_G is the voltage of the GMAW, and I_G is the current of the GMAW.

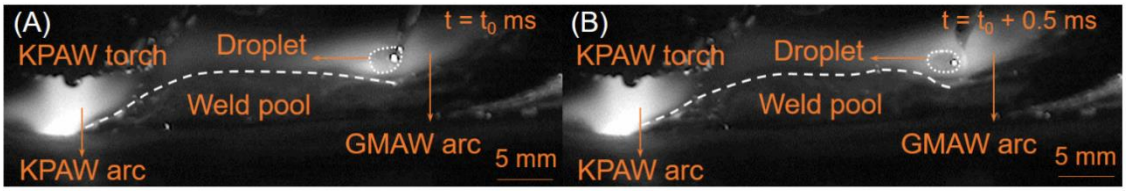

Fig. 4 The high speed photographs of droplet and weld pool in the hybrid KPAW-GMAW process

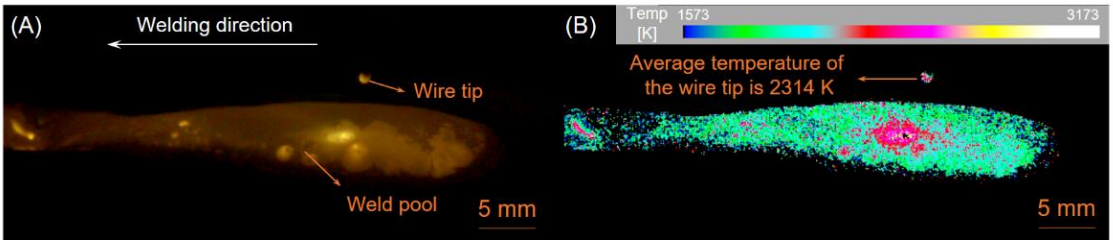

Fig. 6.5 (A) The high speed photograph of the hybrid KPAW-GMAW process; (B) The temperature distribution of the hybrid KPAW-GMAW process

6.3.1.4 Arc heat source model

Before the arcing of the GMAW, it can be seen from **Fig. 6.6 (A)** that the KPAW arc is almost symmetry along the torch axis, so the arc heat source of the KPAW is considered as Gaussian distributed. As shown in Eq. (6.11), a parameter L_K calculated by Eq. (6.12) is introduced to consider the decrease of the heat flux with the increase of the arc length. A global controlling parameter K_K calculated by Eq. (6.13) is introduced to conserve the total KPAW arc energy absorbed by the weld pool. The detail information of the KPAW arc heat source can be seen from our previous study [35].

$$q_{\mathrm{KPAW}} = K_K L_K \frac{3\eta_K U_K I_K}{\pi\sigma_K^2} \exp\left\{-\frac{3(x-x_K-v_w t)^2+3y^2}{\sigma_K^2}\right\} \tag{6.11}$$

$$L_K = (1-\frac{Z_K}{H_K+H_{KB}})^2 \tag{6.12}$$

$$\eta_K U_K I_K = \iint q_{\mathrm{KPAW}} \tag{6.13}$$

where η_K is the arc efficiency of the KPAW, U_K is the voltage of the KPAW, I_K is the current of the KPAW, σ_K is the effective radius of the Gaussian distributed heat source, x_K is the original location of the KPAW torch, v_w is the welding speed along the negative x direction, Z_K is the distance between the cell center and the top of the base metal. H_K is the thickness of the base metal. H_{KB} is the distance between the nozzle and the top of the base metal.

After the arcing of the GMAW, as shown in **Fig. 6 (B)**, **(C)** and **(D)**, the KPAW arc and GMAW arc deflect to each other. The KPAW arc is not symmetry, and the rear part

of the arc is much wider. Here, the double-ellipse heat source models are adopted to consider the deflection of the KPAW arc and GMAW arc.

$$q_{\mathrm{KPAW}} = K_K L_K \frac{6\eta_K U_K I_K}{\pi(\sigma_{Kf}+\sigma_{Kr})\sigma_{Ky}} \exp\left\{-\frac{3(x-x_K-v_w t)^2}{\sigma_{Kx}{}^2} - \frac{3y^2}{\sigma_{Ky}{}^2}\right\}$$
$$\sigma_{Kx} = \begin{cases}\sigma_{Kxf} & x \le x_K + v_w t \\ \sigma_{Kxr} & x > x_K + v_w t\end{cases} \quad (6.14)$$

where σ_{Kxf}, σ_{Kxr}, and σ_{Ky} are the distribution parameters of the double-ellipse heat source of the KPAW.

$$q_{\mathrm{GMAW}} = K_G \frac{6\eta_G U_G I_G}{\pi(\sigma_{Gf}+\sigma_{Gr})\sigma_{Gy}} \exp\left\{-\frac{3(x-x_G-v_w t)^2}{\sigma_{Gx}{}^2} - \frac{3y^2}{\sigma_{Gy}{}^2}\right\}$$
$$\sigma_{Gx} = \begin{cases}\sigma_{Gxf} & x \le x_G + v_w t \\ \sigma_{Gxr} & x > x_G + v_w t\end{cases} \quad (6.15)$$

$$\eta_G U_G I_G = \iint q_{\mathrm{GMAW}} \quad (6.16)$$

where η_G is the arc efficiency of the GMAW, x_G is the original location of the GMAW torch, σ_{Gxf}, σ_{Gxr}, and σ_{Gy} are the distribution parameters of the double-ellipse heat source of the GMAW. The global controlling parameter K_G calculated by Eq. (6.16) is adopted to conserve the total GMAW arc energy absorbed by the weld pool.

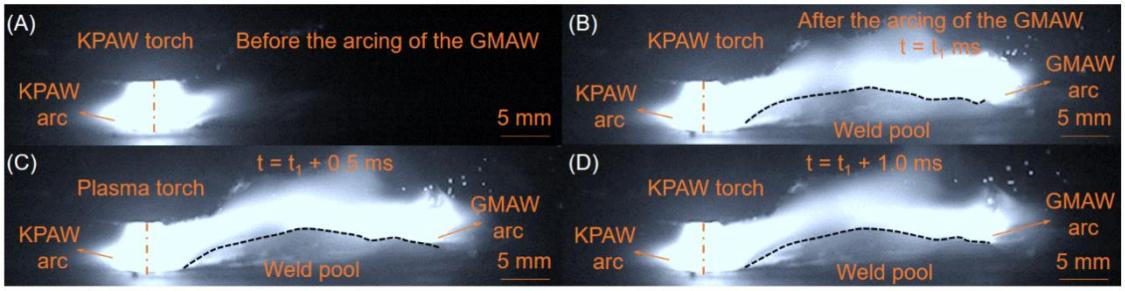

Fig. 6.6 The high speed photographs of arc and weld pool in the hybrid KPAW-GMAW process

With the help of a liquid nitrogen calorimetry, the total energy efficiency of the pulsed GMAW process was measured by Joseph et.al, and the value was 68%~72% [42]. Pépe et.al also measured the total energy efficiency of the bead on plate GMAW process by a liquid nitrogen calorimetry, and suggested the total energy efficiency was about 78% [42]. Haelsig et.al developed a novel calorimetric system to measure the spray model GMAW process, and suggested the total energy efficiency was about 70% [131]. In this study, the total energy efficiency 75% is adopted for the GMAW process.

$$\eta_d + \eta_G = 0.75 \quad (6.17)$$

6.3.1.5 Driven forces

(1) Arc pressure

Fig. 7(A) shows the distribution of the KPAW arc pressure calculated by the KPAW arc model. It should be noted that based on Xu's study, the additional constraint of the keyhole has great influences on the arc pressure [93]. From the top to the bottom of the base metal, the plasma arc pressure was decreased firstly, then increased.

Before the arcing of the GMAW, the Gaussian distributed KPAW arc pressure is adopted, and a parameter K_p is introduced to control the variation of the arc pressure.

$$P_{\mathrm{KPAW}} = (1 + K_P \cdot Z_K) P_{Kmax} \exp\left\{-\frac{3(x - x_K - v_w t)^2 + 3y^2}{{\sigma_p}^2}\right\} \tag{6.18}$$

where P_{Kmax} is the maximum KPAW arc pressure, σ_p is the effective radius of the Gaussian distributed KPAW arc pressure.

After the arcing of the GMAW, the double-ellipse KPAW arc pressure model is adopted to consider the interaction of arcs, in which the maximum KPAW arc pressure (3710.84 Pa), as shown in **Fig. 6.7(A)**, is assumed to be unchanged.

$$\begin{aligned} P_{\mathrm{KPAW}} &= (1 + K_P \cdot Z_K) P_{Kmax} \exp\left\{-\frac{3(x - x_K - v_w t)^2}{{\sigma_{Ka}}^2} - \frac{3y^2}{{\sigma_{Kb}}^2}\right\} \\ \sigma_{Ka} &= \begin{cases} \sigma_{Kaf} & x \le x_K + v_w t \\ \sigma_{Kar} & x > x_K + v_w t \end{cases} \end{aligned} \tag{6.19}$$

where σ_{Kaf}, σ_{Kar}, and σ_{Kb} are the distribution parameters of the double-ellipse KPAW arc pressure.

In previous studies, the double-ellipse arc pressure model was adopted for the tandem submerged arc welding process [132] and three wire submerged arc welding process [133] to consider the arc interaction and torch inclination, in which the maximum arc pressure was calculated by empirical equation. In this study, the double-ellipse GMAW arc pressure model is used, and the influence of arc interaction and torch inclination on the maximum arc pressure (455.28 Pa, as shown in **Fig. 6.7(B)**) is ignored.

$$\begin{aligned} P_{\mathrm{GMAW}} &= P_{Gmax} \exp\left\{-\frac{3(x - x_G - v_w t)^2}{{\sigma_{Ga}}^2} - \frac{3y^2}{{\sigma_{Gb}}^2}\right\} \\ \sigma_{Ga} &= \begin{cases} \sigma_{Gaf} & x \le x_G + v_w t \\ \sigma_{Gar} & x > x_G + v_w t \end{cases} \end{aligned} \tag{6.20}$$

where P_{Gmax} is the maximum GMAW arc pressure, σ_{Gaf}, σ_{Gar}, and σ_{Gb} are the distribution parameters of the double-ellipse GMAW arc pressure.

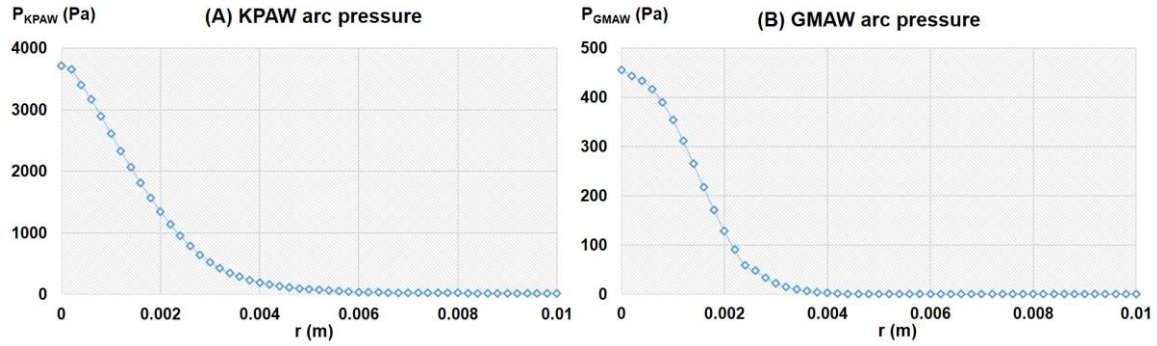

Fig. 6.7 (A) The KPAW arc pressure distribution; (B) The GMAW arc pressure distribution

(2) Arc shear stress

The arc shear stress was calculated by the Phares's model in previous simulations of GTAW process [134] and GMAW process [134]. The empirical arc shear stress was employed in the simulation of the KPAW additive manufacturing [135].

In this study, before the arcing of the GMAW, the KPAW arc shear stress $\tau_{KPAW}(r)$ is calculated by the KPAW arc model, as shown in **Fig. 6.8(A)**.

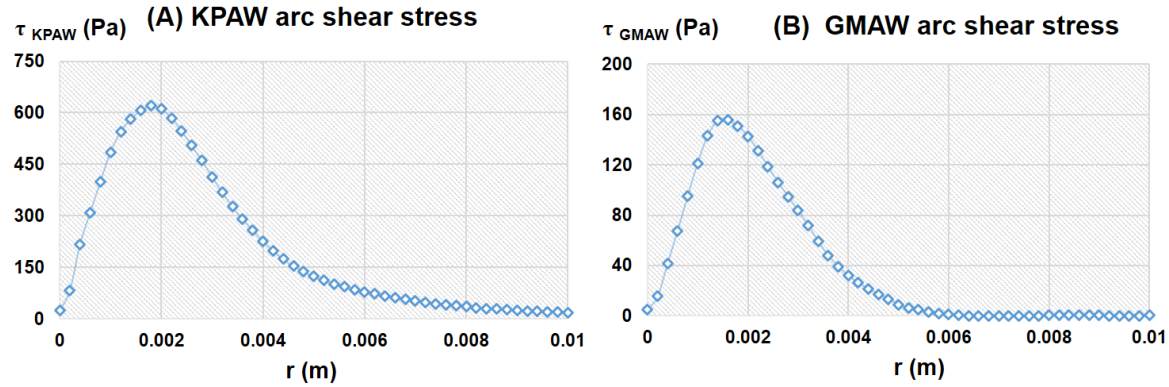

Fig. 6.8 (A) The KPAW arc shear stress distribution; (B) The GMAW arc shear stress distribution

After the arcing of the GMAW, due to the interaction of the arc, keyhole and weld pool, the KPAW arc shear stress is not axisymmetric. Here, a new KPAW arc shear stress model is proposed, as shown in **Fig. 6.9**. A stretching factor A_s is introduced.

$$A_s = \left(\frac{R}{d^2} - \frac{1}{d}\right) r + 1 \tag{6.21}$$

$$d = ab\sqrt{\frac{1+tan^2\theta}{b^2+a^2tan^2\theta}} = ab\sqrt{\frac{(x-x_K-v_wt)^2+y^2}{b^2(x-x_K-v_wt)^2+a^2y^2}} \quad , a = \begin{Bmatrix} a_f & , x \le x_K + v_wt \\ a_r & , x > x_K + v_wt \end{Bmatrix} \tag{6.22}$$

where R is the defined distribution radius of the arc shear stress, d is the distance between the KPAW torch center and the double-ellipse periphery, a_f, a_r, b are the distribution parameters of the double-ellipse KPAW arc shear stress.

Then the new KPAW arc shear stress $\tau_{KPAW}(x, y)$ can be defined.

$$\tau_{\mathrm{KPAW}}(x,y) = \tau_{\mathrm{KPAW}}(A_s r) \tag{6.23}$$

The GMAW arc shear stress $\tau_{\mathrm{GMAW}}(r)$ is also calculated by the GMAW arc model, as shown in **Fig. 6.8(B)**. The new GMAW arc shear stress $\tau_{\mathrm{GMAW}}(x,y)$ considering the influence of arc interaction and torch inclination is also obtained by introducing another stretching factor.

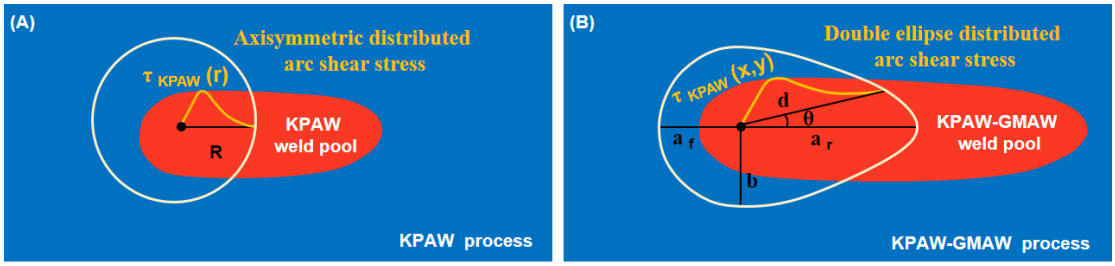

Fig. 6.9 The diagram of the arc shear stress model: (A) Axisymmetric distribution; (B) Double ellipse distribution

It should be noted that the arc shear stress is obtained from arc models with flat base-metal surface, and its direction is horizontal. However, the weld pool is largely deformed in the hybrid KPAW-GMAW process, and the arc shear stress is parallel to the weld pool surface. In this study, it is assumed that the horizontal vector $\vec{o}$, arc shear stress vector $\vec{\tau}$, and free surface normal vector $\vec{n}$ are coplanar, so the arc shear stress vector can be determined [104]:

$$\begin{cases} \vec{\tau}\cdot\vec{n} = 0 \\ |\vec{\tau}| = \tau(x,y) \\ \vec{\tau} = A\vec{o} + B\vec{n} \end{cases} \tag{6.24}$$

where A and B are real numbers.

(3) Marangoni shear stress

In this study, the temperature dependent surface tension is adopted.

$$\gamma = \gamma_0 + \frac{\partial \gamma}{\partial T}(T - T_l) \tag{6.25}$$

where γ_0 is the surface tension of pure metal at the melting point.

The Marangoni shear stress is calculated as follows:

$$\tau_m = \frac{\partial \gamma}{\partial T}\frac{\partial T}{\partial \vec{s}} \tag{6.26}$$

where $\vec{S}$ is the tangential vector.

(4) Buoyance force

The density variation of molten metals is considered for the buoyance force, and the Boussinesq's approximation is used to calculated the buoyance force.

$$F_b = g\beta(T - T_0) \tag{6.27}$$

where g is the gravitational acceleration, and β is the coefficient of thermal expansion.

(5) Electromagnetic force

Before the arcing of the GMAW, the KPAW electromagnetic force is calculated by Eq. (6.28) to Eq. (6.30) [134].

$$F_x = -J_z \times B_\theta \frac{x - x_K - v_w t}{r_e} \tag{6.28}$$

$$F_y = -J_z \times B_\theta \frac{y}{r_e} \tag{6.29}$$

$$F_z = -J_r \times B_\theta \tag{6.30}$$

where F_x, F_y, F_z are the components of the electromagnetic force in the x, y, z directions, J_z is the axial component of the current density, J_r is the radial component of the current density, B_θ is the angular component of the magnetic field, and r_e is the effective radius.

$$r_e = \sqrt{(x - x_K - v_w t)^2 + y^2} \tag{6.31}$$

$$J_z = \frac{I}{2\pi}\int_0^\infty \lambda J_0(\lambda r_e) exp\left(-\frac{\lambda^2\sigma_K^2}{2}\right)\frac{\sinh[\lambda(H_K - Z_K)]}{\sinh(\lambda H_K)}d\lambda \tag{6.32}$$

$$J_r = \frac{I}{2\pi}\int_0^\infty \lambda J_1(\lambda r_e) exp\left(-\frac{\lambda^2\sigma_K^2}{2}\right)\frac{\cosh[\lambda(H_K - Z_K)]}{\sinh(\lambda H_K)}d\lambda \tag{6.33}$$

$$B_\theta = \frac{\mu_m I}{2\pi}\int_0^\infty J_1(\lambda r_e) exp\left(-\frac{\lambda^2\sigma_K^2}{2}\right)\frac{\sinh[\lambda(H_K - Z_K)]}{\sinh(\lambda H_K)}d\lambda \tag{6.34}$$

where J_0 and J_1 are the zero order and one order Bessel functions, respectively.

After the arcing of the GMAW, the effective radius r_e is modified and the double-ellipse KPAW electromagnetic force is adopted [136].

$$r_e = \sqrt{(x - x_K - v_w t)^2 + \left(\frac{\sigma_{Kx}}{\sigma_{Ky}}\right)^2 y^2}\ , \sigma_{Kx} = \begin{Bmatrix}\sigma_{Kxf} & x \le x_K + v_w t\\ \sigma_{Kxr} & x > x_K + v_w t\end{Bmatrix} \tag{6.35}$$

As for the GMAW, the double-ellipse electromagnetic force is also applied.

6.3.2 Numerical simulation

Owing to the symmetry, only half of the computation domain is used in the weld pool simulation. As shown in **Fig. 6.10**, the x-axis is along the left direction, and the y-axis is along the front direction, and the z-axis is along the top direction. The size of the computation domain is 80 mm x 16 mm x 20 mm. The KPAW torch locates at x = -25 mm when the welding is started. At t = 4 s, the GMAW arc is ignited, and the GMAW

torch locates at x = -15 mm. The top part of the computation domain is "void region", and the bottom part is fluid with a thickness of 12 mm. A non-uniform grid system is used: 0.25 mm near the symmetrical plane and 0.3 mm far from the symmetrical plane. The governing equations and VOF equation with the required boundary conditions are solved using the commercial CFD (Computational Fluid Dynamics) software FLOW3D. The details of the iteration scheme are as follows:

(1) The new-time level velocities are computed using the explicit approximations based on variables of the previous time level.

(2) To satisfy the mass conservation, the pressure correction formula is solved by the successive over-relaxation (SOR) method, then the energy conservation equation is solved by the implicit method.

(3) The free surface is updated by the VOF equation.

The thermo-physical material properties of low carbon steel can be seen in Table 1, which are obtained from the fluid database of FLOW3D and our previous work [77]. In previous studies of weld pool simulation [95, 134, 136], only the temperature dependent surface tension was used, and the numerical results agreed well with the experimental results. In this study, only the influence of the temperature on the surface tension is considered.

Table 6.1. Thermo-physical material properties of low carbon steel

Nomenclature	Value	Nomenclature	Value
Density (kg m^{-3})	7800	Liquidus temperature (K)	1798
Viscosity (kg m^{-1} s^{-1})	0.006	Solidus temperature (K)	1768
Specific heat (l) (J kg^{-1} K^{-1})	866	Boiling temperature (K)	2900
Specific heat (s) (J kg^{-1} K^{-1})	686	Emissivity	0.4
Latent heat of fusion (J kg^{-1})	2.77×10^{5}	Coefficient of thermal expansion (K^{-1})	1.44×10^{-5}
Thermal conductivity (l) (W m^{-1} K^{-1})	26.9	Surface tension (N m^{-1})	1.2
Thermal conductivity (s) (W m^{-1} K^{-1})	32.3	Surface tension gradient (N m^{-1} K^{-1})	-0.0003

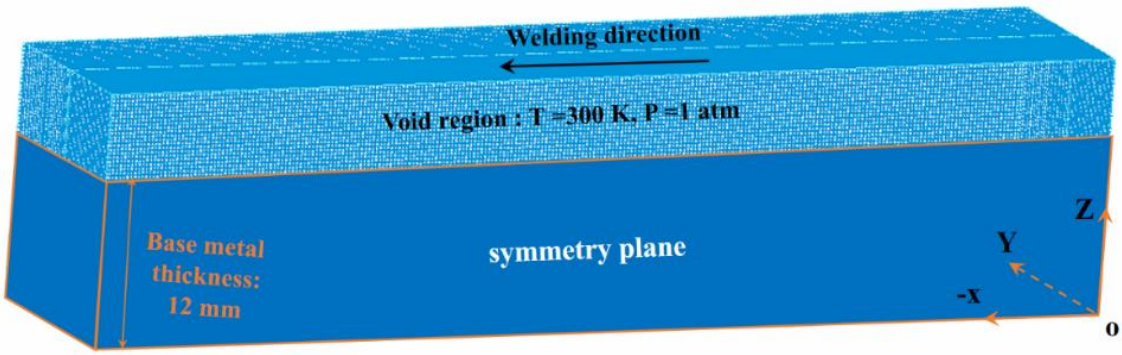

Fig. 6.10 The diagram of the mesh used in the simulation

6.4 Results and discussion

In this study, the heat transfer and material flow in the KPAW process and KPAW-GMAW process are discussed. The driven forces for the material flow are analyzed.

6.4.1 The heat transfer and material flow in the KPAW process

As shown in **Fig. 6.11(A)**, at the beginning of the welding, a small concave is formed. The molten metals are pushed out from the arc center to the rear part of the weld pool, and the maximum temperature is 2153K. At t = 0.5 s, more solid metals are melted. The weld pool size becomes large, and the maximum temperature is 2478 K. At t = 3.0 s, a large keyhole is formed. The molten metals flow backward to the weld pool rear, and two convective eddies exist inside the weld pool: an anti-clockwise eddy at the bottom part of the weld pool, and a clockwise eddy at the top part of the weld pool. The maximum temperature is 2114 K. At t = 4.0 s, the weld pool is very large, and the convective eddies inside the weld pool are unchanged. The maximum temperature is 2093 K.

In our previous studies [35], the small currents were used, so the maximum temperature of the weld pool was less than 2000 K. Here, the large current (265 A) is used, and the maximum temperature of the weld pool is increased.

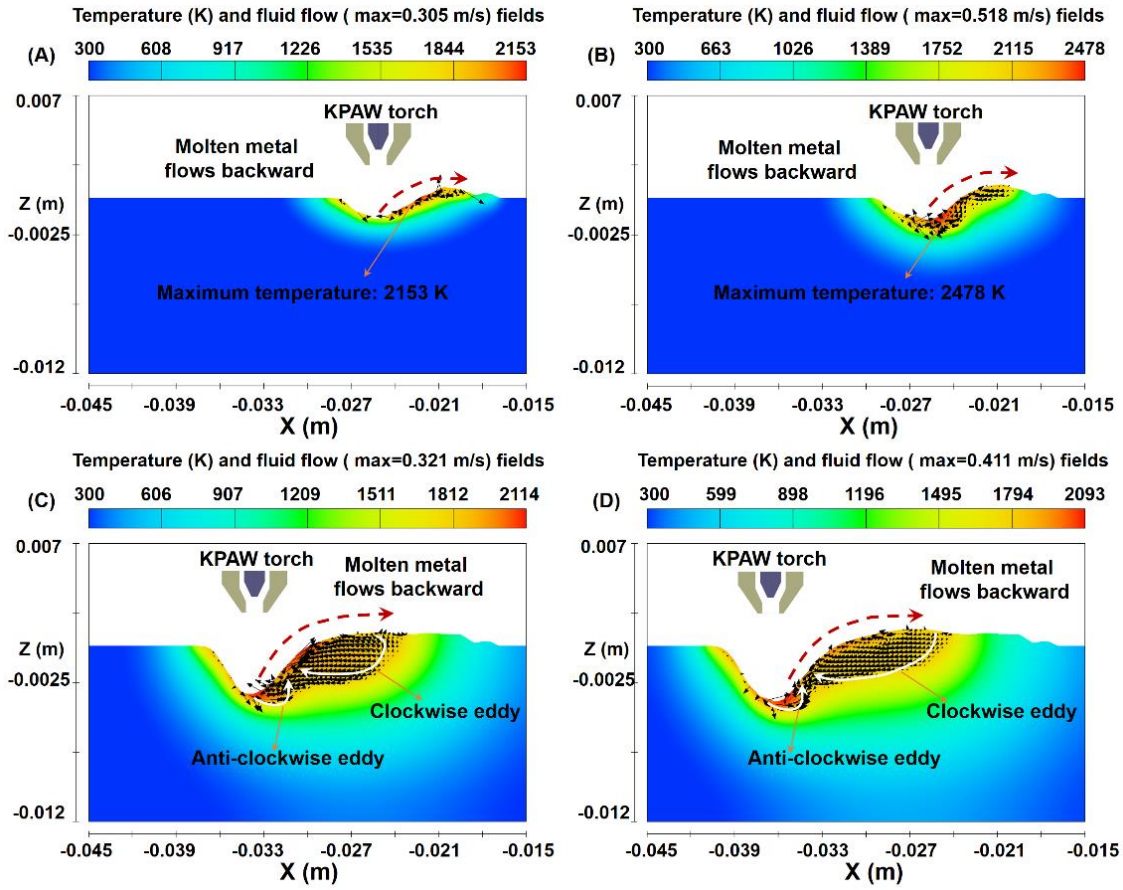

Fig. 6.11 Temperature (K) and fluid flow fields of y=0 cross sectional view in the KPAW process at: (A) t = 0.2s; (B) t = 0.5 s; (C) t = 3.0 s; (D) t = 4.0 s

The driven forces for the heat transfer and material flow in the KPAW process had already been discussed in our previous study [35]. Here an interesting thermo-physical phenomenon is found. As shown in **Fig. 6.12**, the maximum temperature of the weld pool is firstly increased (Increase stage), then is decreased (Decrease stage), and finally becomes stable (stable stage). This is because at the beginning of the welding, the molten metals accumulate at the rear part of the weld pool. Even though the action region of the arc shear stress is large, the weld pool is very small, so the convection in the weld pool is insufficient, resulting in an increase of the temperature. When the weld pool becomes large, under the influence of the arc shear stress and arc pressure, the energy can be easily transported in the horizontal and vertical directions, so the temperature gradient in the weld pool is decreased.

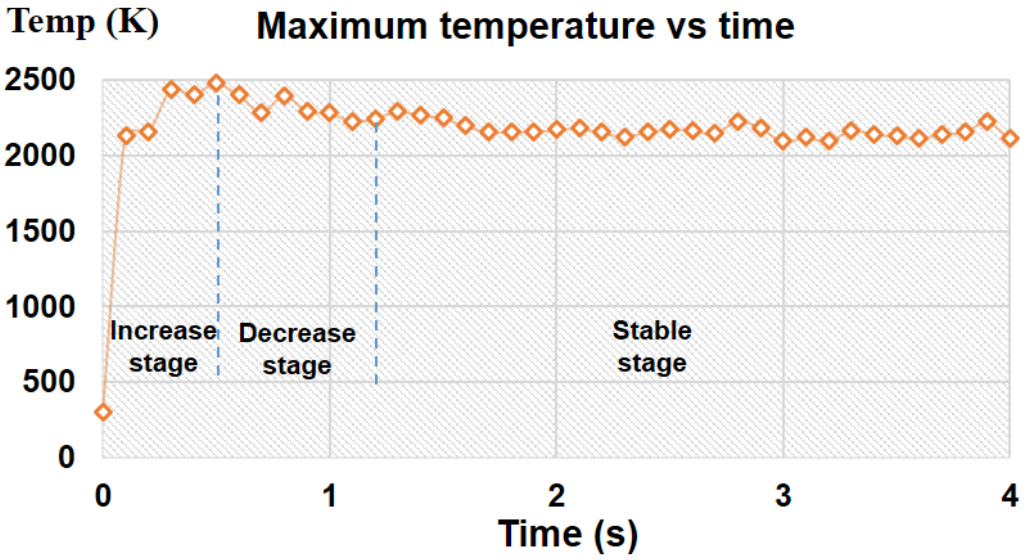

Fig. 6.12 The maximum weld pool temperature vs time

6.4.2 The heat transfer and material flow in the hybrid KPAW-GMAW process

The GMAW arc is ignited at t = 4.0 s. As shown in **Fig. 6.13**, at t= 4.3 s, a small weld pool is formed below the GMAW arc, and the maximum temperature of the weld pool (2770 K) locates at the region near the GMAW arc center. It can be seen that the convective patterns near the KPAW arc are almost unchanged. It should be noted that even though the heat input in the KPAW process (4006.8 W) is similar to that in the GMAW process (4554 W), the weld pool temperature is much lower in the KPAW process, which is caused by the stronger fluid flow and energy propagation due to much higher arc pressure and arc shear stress in the KPAW process [35].

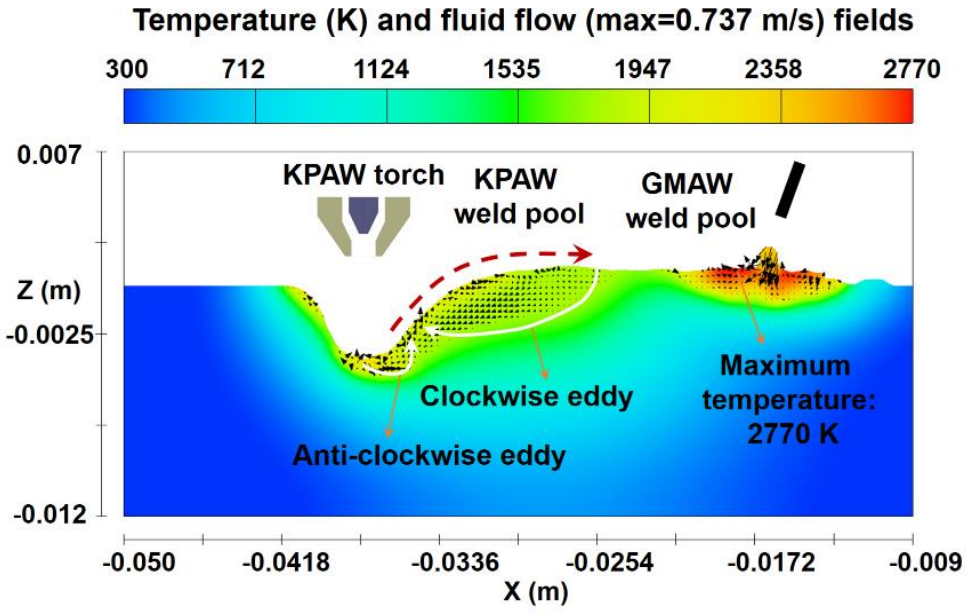

Fig. 6.13 Temperature (K) and fluid flow fields of y=0 cross sectional view in the hybrid KPAW-GMAW process at t = 4.3 s

As shown in **Fig. 6.14**, at t = 4.6 s, the KPAW weld pool and GMAW weld pool are connected, and a large weld pool is formed. The maximum temperature of the weld pool (2754 K) locates at the region near the GMAW arc. It can be obviously seen that at the top weld pool surface between two arcs, the molten metals flow backward in the front part, and flow forward in the rear part.

At t = 7.0 s, the molten metals are fully mixed. The "Pull-Push" flow pattern at the top weld pool surface between two arcs becomes more obvious. Due to the "Pull-Push" flow pattern, the molten metals under the KPAW arc can't easily flow to the weld pool rear, but accumulate at the region between two arcs. The molten metals flow inward near the GMAW arc, and flow outward after the GMAW arc. The maximum temperature of the weld pool (2623 K) locates at the region near the GMAW arc.

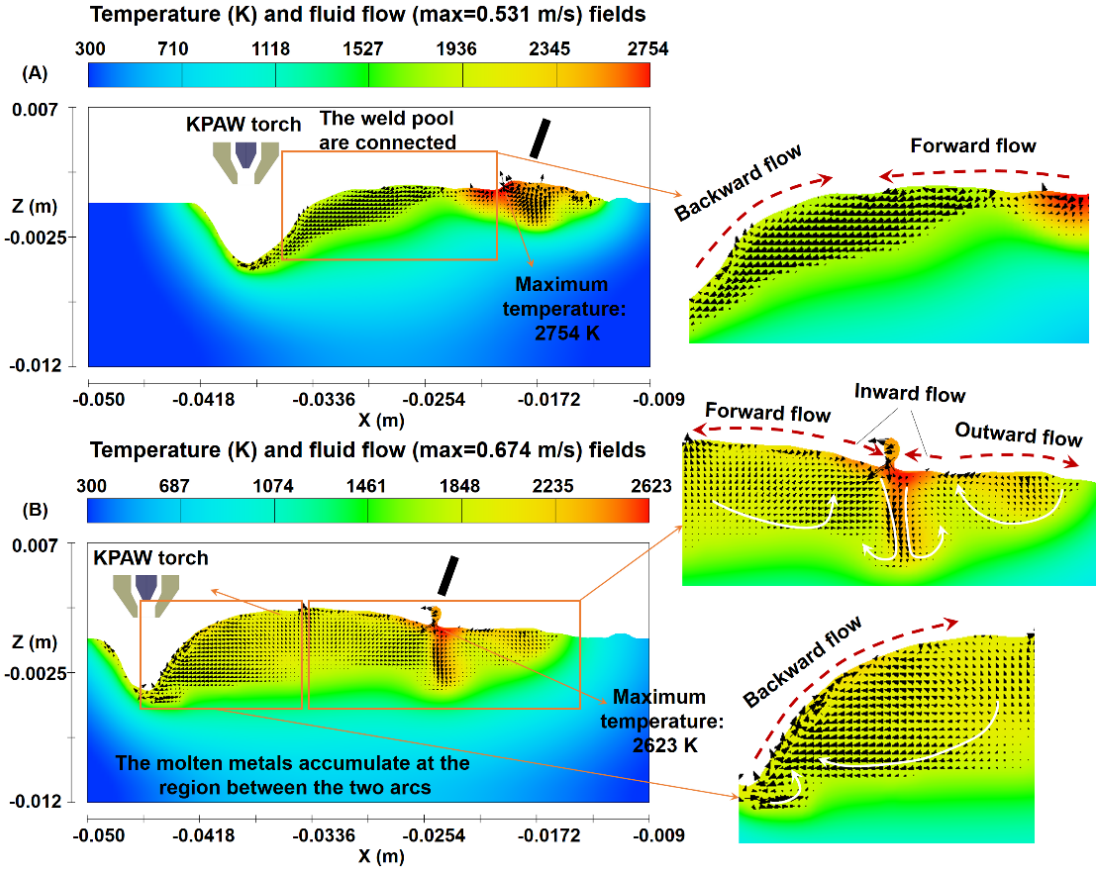

Fig. 6.14 Temperature (K) and fluid flow fields of y=0 cross sectional view in the hybrid KPAW-GMAW process at: (A) t = 4.6 s; (B) t = 7.0 s

As shown in **Fig. 6.15**, at t = 4.6 s, a high temperature region can be seen under the

KPAW arc, and the maximum temperature is 2161 K. At t = 7.0 s, a high temperature region can be seen after the KPAW arc (at the top surface of the rear keyhole), and the maximum temperature is 2211 K. Owing to the "Pull-Push" flow pattern, the molten metals and energy can be transported from the region near the GMAW arc to the region near the KPAW arc, causing the temperature increase of molten metals at the top surface of the rear keyhole.

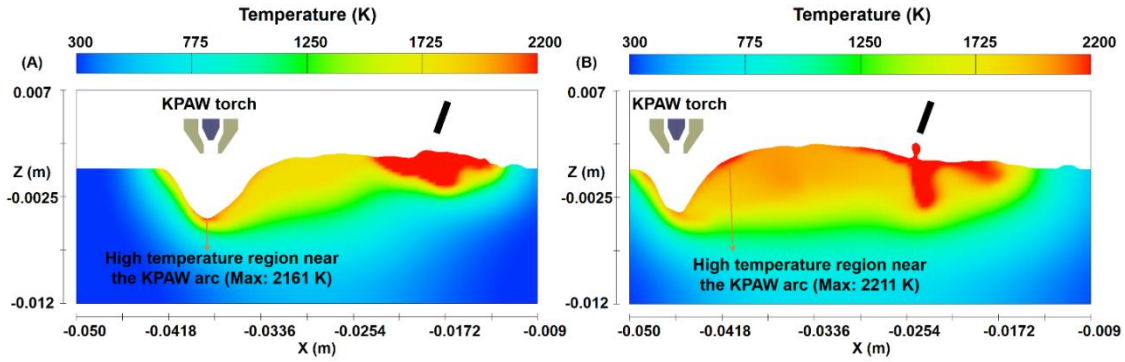

Fig. 6.15 Temperature field of y=0 cross sectional view in the hybrid KPAW-GMAW process at: (A) t = 4.6 s; (B) t = 7.0 s

6.4.3 The driven forces for the material flow in the hybrid KPAW-GMAW process

The convective patterns in the hybrid KPAW-GMAW process are rather complex. Here, the driven forces for the material flow in the hybrid weld pool are discussed.

Based on the numerical simulation and our previous study [35], the driven forces and convective patterns in the KPAW process can be concluded. As shown in **Fig. 6.16**, the molten metals at the bottom part of the weld pool flow downward under the influence of arc pressure and Lorentz force, so an anti-clockwise eddy is formed. The molten metals at the top part of the weld pool flow backward under the influence of Marangoni force and arc shear stress, so a clockwise eddy is formed.

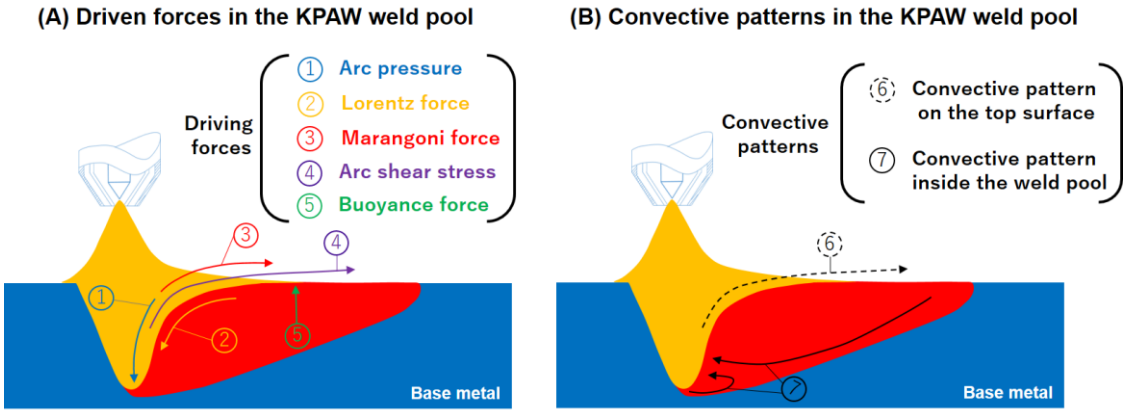

Fig. 6.16 (A) The driven forces in the KPAW weld pool; (B) The convective patterns in the KPAW weld pool

Based on the previous study [124], the convective patterns in the GMAW process can be concluded. As shown in **Fig. 6.17**, the molten metals near the arc center flow inward under the influence of the arc pressure, Lorentz force and droplet impingement force. The molten metals far from the arc center flow outward under the influence of the Marangoni force and arc shear stress.

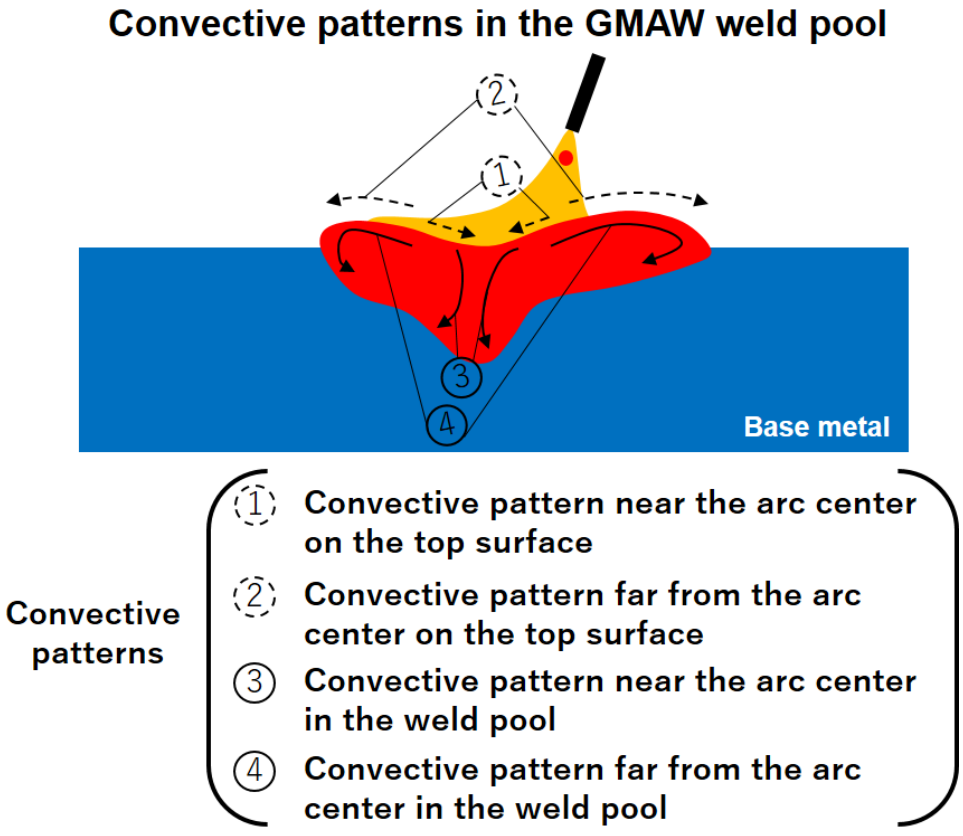

Fig. 6.17 The convective patterns in the GMAW weld pool

The simulation without the droplet impingement is restarted at t = 4. 0 s. It can be seen from **Fig. 6.18** that the convective patterns are similar to these in **Fig. 6.14**, and the "Pull-Push" is still very strong, which means that the droplet impingement has minor influence on the "Pull-Push" flow pattern on the top weld pool surface. However, without the droplet impingement, few molten metals are transported from the region near the GMAW arc to the region near the KPAW arc, so the molten metals at the rear keyhole are few.

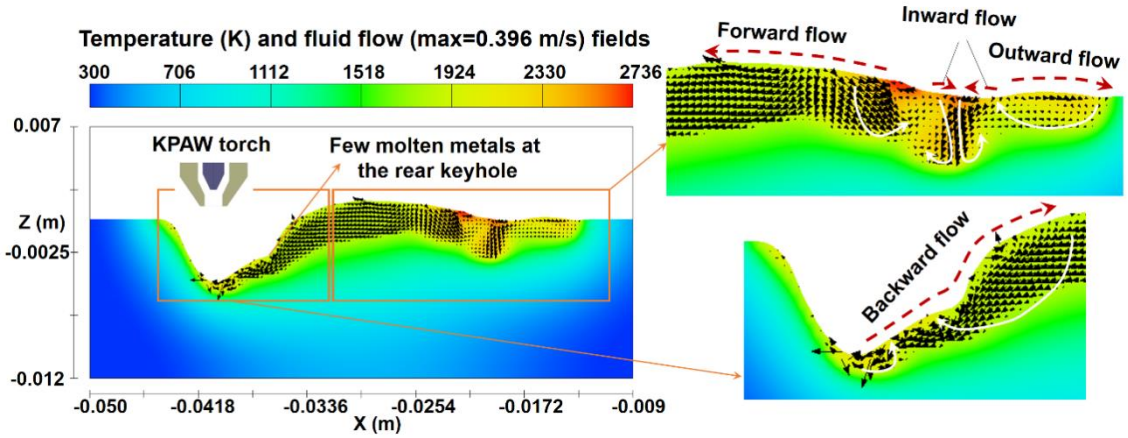

Fig. 6.18 The simulation of the hybrid KPAW-GMAW process without the droplet impingement at t = 5.5 s

The simulation without the Marangoni force is restarted at t = 4. 0 s. It should be noted that the arc pressure and plasma shear stress have major influences, while the Marangoni force has a minor influence on the fluid flow near the KPAW arc [35]. Without Marangoni force, the convective patterns and intensity are unchanged near the KPAW arc. As shown in **Fig. 6.19**, even though the convective patterns are similar to these in **Fig. 6.14**, the forward flow on the top weld pool surface becomes weak. The molten metals under the KPAW arc can easily flow to the weld pool rear, so the molten metals at the rear keyhole are few.

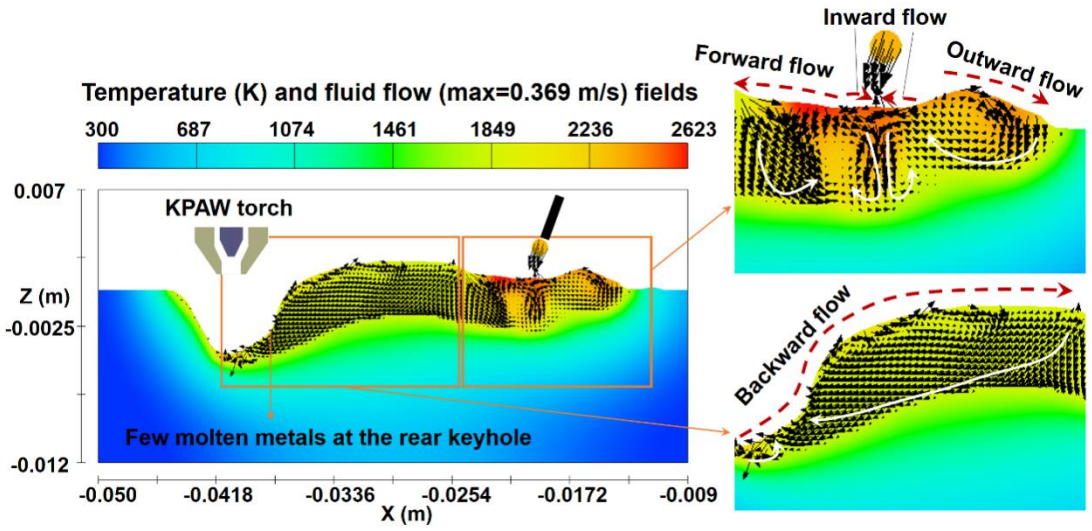

Fig. 6.19 The simulation of the hybrid KPAW-GMAW process without the Marangoni force at t = 5.5 s

The simulation without the GMAW arc shear stress is restarted at t = 4.0 s. As shown in **Fig. 6.20**, the convective patterns are also similar to these in **Fig. 6.14**, but the forward flow on the top weld pool surface is also very weak, which can't suppress the backward flow of molten metals under the KPAW arc, so the molten metals at the rear keyhole are also few.

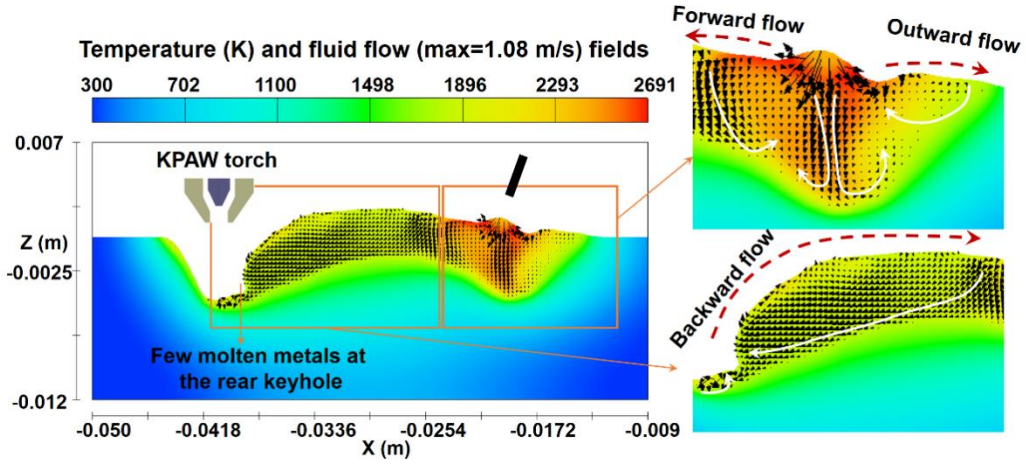

Fig. 6.20 The simulation of the hybrid KPAW-GMAW process without the GMAW arc shear stress at t = 5.5 s

Based on the above analysis and the numerical simulation, the weld pool convective patterns and their driven forces in the hybrid KPAW-GMAW process can be obtained. As shown in **Fig. 6.21**, the convective pattern 1 on the top surface near the KPAW arc is caused by Marangoni force and arc shear stress. The convective pattern 2 on the top

surface in the transition region is caused by the Marangoni force and arc shear stress. The convective pattern 3 on the top surface near the GMAW arc is caused by the arc pressure, Lorentz force and droplet impingement force. The convective pattern 4 on the top surface after the GMAW arc is caused by the Marangoni force and arc shear stress. The convective pattern 5 near the KPAW arc at the bottom part of the weld pool is caused by the arc pressure and Lorentz force. The convective pattern 6 near the KPAW arc at the top part of the weld pool is caused by the Marangoni force and arc shear stress. The convective pattern 7 in the weld pool of the transition region is caused by the Marangoni force and arc shear stress. The convective pattern 8 in the weld pool near the GMAW arc is caused by the arc pressure, Lorentz force and droplet impingement force. The convective pattern 9 in the weld pool after the GMAW arc is caused by the Marangoni force and arc shear stress.

It can be concluded that the Marangoni force and arc shear stress are the dominant driven forces for the “Pull-Push” flow pattern on the top weld pool surface between two arcs. In previous studies, the irregular backward flow of the molten metals was proposed to be dominant reason for the weld defects formation in the arc welding [37,137]. Owing to the “Push” flow pattern in the hybrid KPAW-GMAW process, the strong backward flow from the keyhole is suppressed, which is benefit for sound weld bead formation.

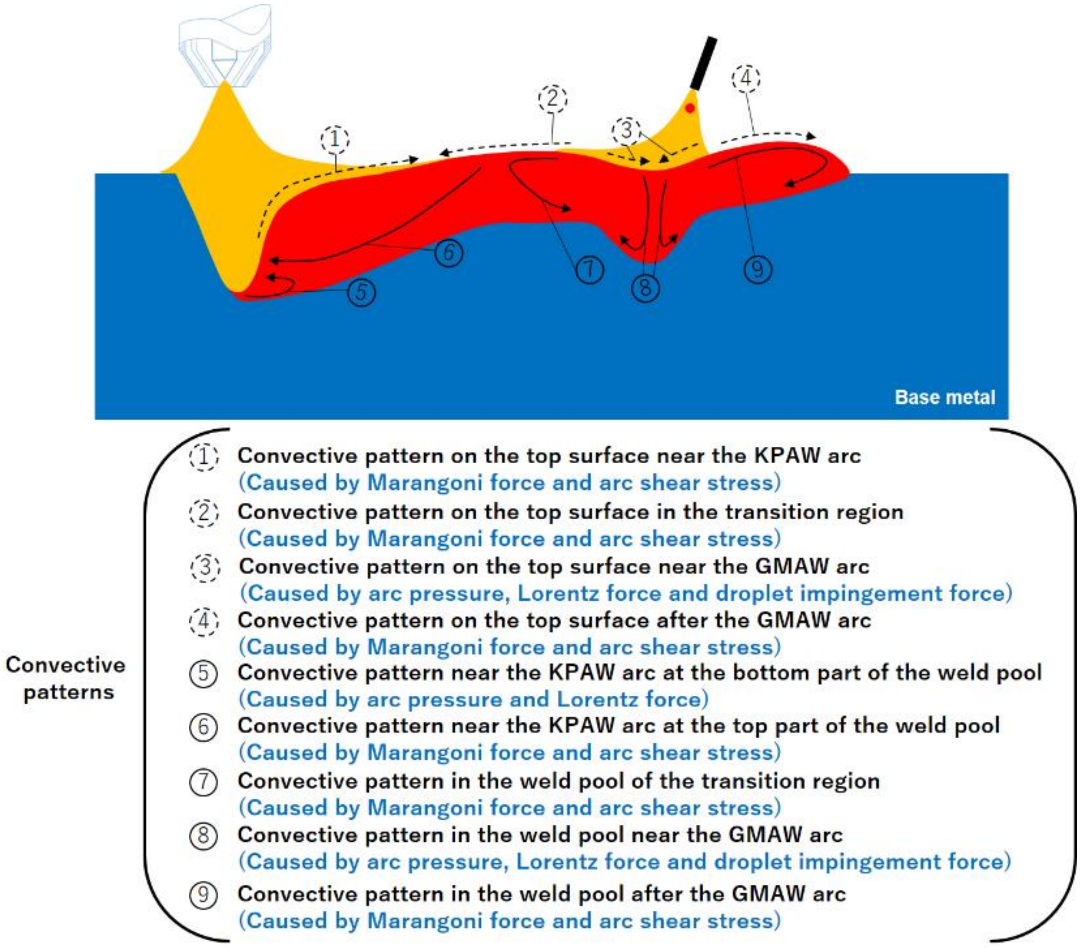

Fig. 6.21 The convective patterns in the hybrid KPAW-GMAW weld pool

6.4.4 Validation of the numerical simulation

The weld bead formation, high speed photographs of the weld pool and weld pool temperature in the KPAW process are showed in **Fig. 6.22** based on the "Sudden Stop Test" method. It can be seen from Case 1 and Case 2 that at the beginning of the welding, the molten metals accumulate at the rear part of the weld pool, and a small bulge is formed. From Case 1 to Case 2, the weld length is increased, and the maximum temperature of the weld pool is also increased (2216 K in Case 1, and 2375 K in Case 2). As the welding continues, the maximum temperature of the weld pool is decreased (2096 K in Case 3, and 2074 K in Case 4). The calculated maximum temperature and its variation tendency in the KPAW process are similar to the experimental results.

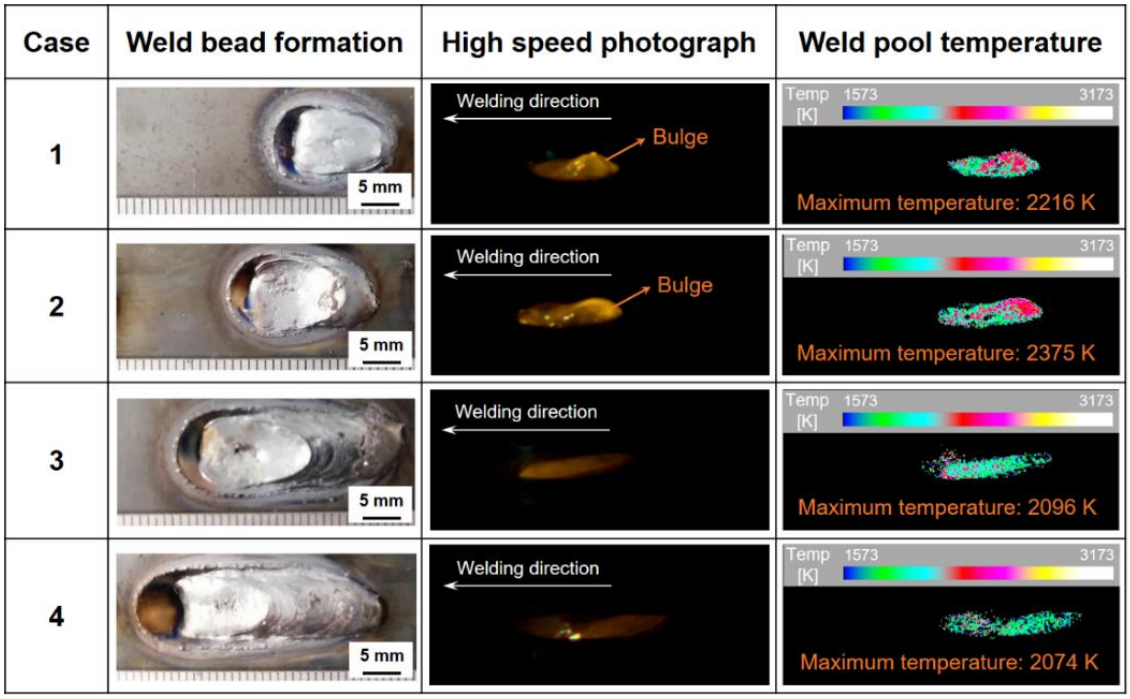

Fig. 6.22 The weld bead formation, high speed photographs of the weld pool and weld pool temperature in the KPAW process

The high speed photograph of the weld pool and weld pool temperature in the hybrid KPAW-GMAW process are showed in **Fig. 6.5**. It can be seen that a large high temperature region is formed below the GMAW arc, and the maximum temperature of the weld pool is 2656 K. In the numerical simulation, the maximum temperature of the weld pool is within [2600 K, 2800 K]. The calculated temperature distribution in the hybrid KPAW-GMAW process agrees well with the experimental result.

As shown in **Fig. 6.23**, the experimental and calculated weld widths on the top surface are 12.95 mm and 11.94 mm, respectively. The experimental and calculated weld depths are 5.43 mm and 5.43 mm, respectively. The experimental and calculated weld reinforcements are 1.47 mm and 2.55 mm, respectively. In summary, the calculated weld geometry agrees well with the experimental result. However, it should be noted that the porosity is formed in the weld. The porosity formation has been widely investigated in the keyhole laser welding, which is caused by the keyhole instability [37]. In the future, we will investigate the porosity formation mechanism in the KPAW process and hybrid KPAW- GMAW process, and adopt reasonable methods to suppress it.

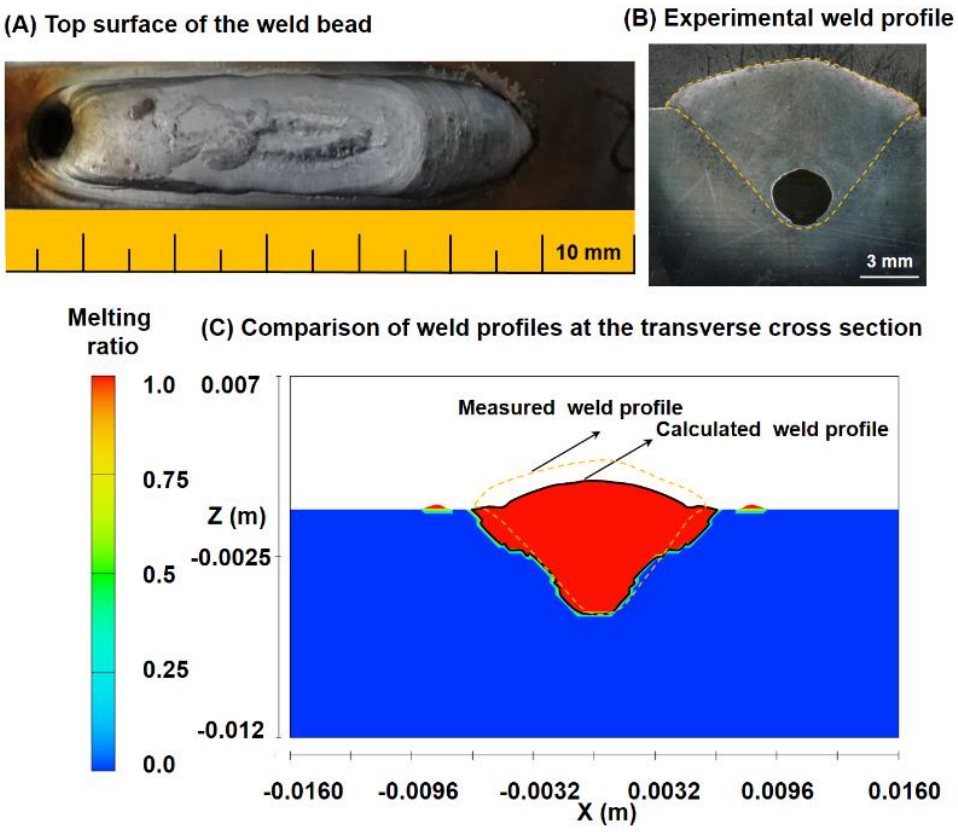

Fig. 6.23 (A) Top surface of the weld bead; (B) Experimental weld profile at the transverse cross section; (C) Comparison of weld profiles at the transverse cross section

6.5 Conclusions

In this study, a novel one way coupled electrode-arc-droplet-weld pool model considering the complicated interaction of the arc, keyhole and weld pool is developed to investigate the heat transfer and material flow in the hybrid KPAW-GMAW process. The conclusions can be summarized as follows:

(1) In the KPAW process, two convective eddies exist inside the weld pool: an anti-clockwise eddy is formed at the bottom part of the weld pool under the influence of the arc pressure and Lorentz force, and a clockwise eddy is formed at the top part of the weld pool under the influence of the Marangoni force and arc shear stress. The maximum temperature of the weld pool is firstly increased, then is decreased, and finally becomes stable.

(2) In the hybrid KPAW-GMAW process, owing to the “Pull-Push” flow pattern, the molten metals and energy can be transported from the region near the GMAW arc to the

region near the KPAW arc, causing the temperature increase of molten metals at the top surface of the rear keyhole.

(3) The detailed convective patterns and their driven forces in the hybrid KPAW-GMAW process are studied. The Marangoni force and arc shear stress contribute to the appearance of “Pull-Push” flow pattern on the top surface of the weld pool between two arcs.

(4) The droplet impingement has a minor influence on the “Pull-Push” flow pattern. However, without the droplet impingement, few molten metals are transported from the region near the GMAW arc to the region near the KPAW arc.

Chapter 7 Conclusions

In this study, the hybrid KPAW-GMAW process is proposed to improve the weld bead formation. Some fundamental phenomena related to the weld pool convection, keyhole behaviors and energy propagation in the KPAW process are firstly investigated, then the interactive phenomena of the arc, droplet, keyhole and weld pool in the hybrid KPAW-GMAW process are analyzed. The following conclusions can be obtained:

(1) The interesting phenomenon that the weld pool temperature is relatively low in the KPAW process is explained. The much high arc pressure and plasma shear stress promote the fluid flow and energy transportation, thus a large weld pool is formed, leading to a low weld pool temperature distribution in the KPAW process.

(2) The keyhole formation mechanisms in the KPAW process are revealed. The arc pressure is more dominant for the keyhole formation, and the plasma shear stress facilitates the fluid flow along the rear keyhole wall and decreases the curvature of the keyhole. Both the pressure balance and mass conservation mechanisms contribute to the blasting penetration. The material properties have great influences on the blasting penetration. Low melting temperature, low surface tension and bottom surface deformation facilitate the blasting penetration, while high thermal conductivity inhibits it.

(3) The interesting phenomenon that the energy efficiency is relatively low in the KPAW process is explained. In the KPAW process, the arc size is large, and the arc temperature is high, so the conduction energy loss and radiation loss of the plasma arc are high. The keyhole formation can’t increase the energy absorption, and 11.5% of the arc energy are lost by the efflux arc. As a result, the energy efficiency for heating the anode is decreased.

(4) The interactive phenomena of the arc and droplet in the hybrid KPAW-GMAW process are analyzed. Owing to the formation of a direct current path between the KPAW cathode (tungsten electrode) and GMAW anode (welding wire) in the peak current stage, the ionized PA is extended to the GMA side. The wire extension length is shorter, and the

arc length is larger in hybrid KPAW-P-GMAW in comparison with P-GMAW. The metal vapor from the keyhole has a minor influence on the droplet transfer, while the Lorenz force promotes the droplet transfer. The stable OPOD mode can be obtained in the hybrid KPAW-P-GMAW.

(5) The interactive phenomena of the droplet, keyhole and weld pool in the hybrid KPAW-GMAW process are analyzed. In the hybrid KPAW-GMAW process, the Marangoni force and arc shear stress contribute to the appearance of “Pull-Push” flow pattern on the top surface of the weld pool between the two arcs. The droplet impingement has minor influence on the “Pull-Push” flow pattern. However, without the droplet impingement, few molten metals are transported from the region near the GMAW arc to the region near the KPAW arc.

Reference

[1] Vilkas, E. P. (1991). Plasma arc welding of exhaust pipe system components. Welding journal, 70(4), 49-52.

[2] Irving, B. (1997). Why aren't airplanes welded? Welding Journal, 76(1), 31-41.

[3] Irving, B. (1992). Plasma arc welding takes on the advanced solid rocket motor. Welding journal, 71(12), 49-52.

[4] Martikainen, J. K., & Moisio, T. J. I. (1993). Investigation of the effect of welding parameters on weld quality of plasma arc keyhole welding of structural steels. Welding journal, 72, 329s–340s.

[5] Wu, C. S., Jia, C. B., & Chen, M. A. (2010). A control system for keyhole plasma arc welding of stainless steel plates with medium thickness. Welding journal, 89(11), 225-231.

[6] Zhang, Y. M., & Zhang, S. B. (1999). Observation of the keyhole during plasma arc welding. Welding journal, 78, 53S-58S.

[7] Xu, B., Chen, S., Tashiro, S., Jiang, F., & Tanaka, M. (2020). Material flow analyses of high-efficiency joint process in VPPA keyhole flat welding by X-ray transmission system. Journal of Cleaner Production, 250, 119450.

[8] Wu, C. S., & Liu, Z. M. (2015). Dynamic variation of keyhole exit and its inclination in plasma arc welding. Welding in the World, 59(3), 365-371.

[9] Liu, Z. M., Wu, C. S., Liu, Y. K., & Luo, Z. (2015). Keyhole behaviors influence weld defects in plasma arc welding process. Welding journal, 94, 281-290.

[10] Nguyen, A. V., Wu, D., Tashiro, S., & Tanaka, M. (2019). Undercut formation mechanism in the keyhole plasma arc welding. Welding Journal, 98,204s-212s.

[11] Van Anh, N., Shinichi, T., Van, H. B., & Manabu, T. (2017). Development of Plasma-MIG hybrid welding process. Quarterly journal of JWS, 35(2), 132s-136s.

[12] Guo, Y., Pan, H., Ren, L., & Quan, G. (2018). An investigation on plasma-MIG hybrid welding of 5083 aluminum alloy. The International Journal of Advanced Manufacturing Technology, 98(5-8), 1433-1440.

[13] Skowrónska, B., Chmielewski, T., Golański, D., & Szulc, J. (2020). Weldability of S700MC steel welded with the hybrid plasma+ MAG method. Manufacturing Review, 7, 4.

[14] Wu, D., Tashiro, S., Wu, Z., Nomura, K., Hua, X., & Tanaka, M. (2020). Interactive Phenomena in Hybrid KPAW GMAW-P. Welding Journal, 99(5), S146-S155.
[15] Aithal, S. M., Subramaniam, V. V., Pagan, J., & Richardson, R. W. (1998). Numerical model of a transferred plasma arc. Journal of applied physics, 84(7), 3506-3517.
[16] Pan, J., Hu, S., Yang, L., & Chen, S. (2016). Numerical analysis of the heat transfer and material flow during keyhole plasma arc welding using a fully coupled tungsten–plasma–anode model. Acta materialia, 118, 221-229.
[17] Tanaka, M., & Lowke, J. J. (2006). Predictions of weld pool profiles using plasma physics. Journal of Physics D: Applied Physics, 40(1), R1.
[18] Van Anh, N., Tashiro, S., Van Hanh, B., & Tanaka, M. (2017). Experimental investigation on the weld pool formation process in plasma keyhole arc welding. Journal of Physics D: Applied Physics, 51(1), 015204.
[19] Sato, T. , Okubo, A. , Oji, T. , & Hirata, Y. (1998). Measurement of molten pool temperature distribution by uv thermal radiation. Welding International, 12(8), 627-634.
[20] Yamazaki, K. , Yamamoto, E. , Suzuki, K. , Koshiishi, F. , Tashiro, S. , & Tanaka, M. , et al. (2013). Measurement of surface temperature of weld pools by infrared two colour pyrometry. ence & Technology of Welding & Joining, 15(1), 40-47.
[21] Chen, X. , Pang, S. , Shao, X. , Wang, C. , Zhang, X. , & Jiang, P. , et al. (2017). Sub-microsecond vapor plume dynamics under different keyhole penetration regimes in deep penetration laser welding. Journal of Physics D Applied Physics, 50(20), 205601.
[22] Zou, J. L. , Wu, S. K. , Yang, W. X. , He, Y. , & Xiao, R. S. . (2016). A novel method for observing the micro-morphology of keyhole wall during high-power fiber laser welding. Materials & Design, 89(JAN.), 785-790.
[23] Zou, J., Ha, N., Xiao, R., Wu, Q., & Zhang, Q. (2017). Interaction between the laser beam and keyhole wall during high power fiber laser keyhole welding. Optics express, 25(15), 17650-17656.
[24] Huang, L., Hua, X., Wu, D., & Li, F. (2018). Numerical study of keyhole instability and porosity formation mechanism in laser welding of aluminum alloy and steel. Journal of Materials Processing Technology, 252, 421-431.
[25] Miyagi, M., Kawahito, Y., Kawakami, H., & Shoubu, T. (2017). Dynamics of solid-liquid interface and porosity formation determined through x-ray phase-contrast in laser welding of pure Al. Journal of Materials Processing Technology, 250, 9-15.

[26] Fabbro, R., Slimani, S., Doudet, I., Coste, F., & Briand, F. (2006). Experimental study of the dynamical coupling between the induced vapour plume and the melt pool for Nd–Yag CW laser welding. Journal of physics D: Applied physics, 39(2), 394.

[27] Zhang, M., Zhang, Z., Tang, K., Mao, C., Hu, Y., & Chen, G. (2018). Analysis of mechanisms of underfill in full penetration laser welding of thick stainless steel with a 10 kW fiber laser. Optics & Laser Technology, 98, 97-105.

[28] Chen, S., Xu, B., & Jiang, F. (2018). Blasting type penetrating characteristic in variable polarity plasma arc welding of aluminum alloy of type 5A06. International Journal of Heat and Mass Transfer, 118, 1293-1306.

[29] Wu, C. S., Zhao, C. Y., Zhang, C., & Li, Y. F. (2017). Ultrasonic vibration assisted keyholing plasma arc welding. Welding Journal, 96(8), 279-286.

[30] Wang, L., Zhang, C., & Wu, C. (2020). Experimental study on controlled pulse keyholing plasma arc welding assisted by ultrasonic vibration. The International Journal of Advanced Manufacturing Technology, 107(11-12), 4995-5009.

[31] Zhang, C., Wu, C., & Tian, S. (2020). Effect of ultrasonic vibration on current density and keyholing capability of plasma arc. Science and Technology of Welding and Joining, 25(5), 422-430.

[32] Mendez, P. F., & Eagar, T. W. (2003). Penetration and defect formation in high-current arc welding. Welding Journal, 82(10), 296.

[33] Oh, D. S., Kim, Y. S., & Cho, S. M. (2005). Derivation of current density distribution by arc pressure measurement in GTA welding. Science and Technology of Welding and Joining, 10(4), 442-446.

[34] Cheon, J., Kiran, D. V., & Na, S. J. (2016). Thermal metallurgical analysis of GMA welded AH36 steel using CFD–FEM framework. Materials & Design, 91, 230-241.

[35] Wu, D., Van Nguyen, A., Tashiro, S., Hua, X., & Tanaka, M. (2019). Elucidation of the weld pool convection and keyhole formation mechanism in the keyhole plasma arc welding. International Journal of Heat and Mass Transfer, 131, 920-931.

[36] Meng, X., Qin, G., Bai, X., & Zou, Z. (2016). Numerical analysis of undercut defect mechanism in high speed gas tungsten arc welding. Journal of Materials Processing Technology, 236, 225-234.

[37] Meng, X., Qin, G., & Zou, Z. (2016). Investigation of humping defect in high speed gas tungsten arc welding by numerical modelling. Materials & Design, 94, 69-78.

[38] Meng, X., Qin, G., & Zou, Z. (2017). Sensitivity of driving forces on molten pool behavior and defect formation in high-speed gas tungsten arc welding. International Journal of Heat and Mass Transfer, 107, 1119-1128.
[39] Jin, X., Berger, P., & Graf, T. (2006). Multiple reflections and fresnel absorption in an actual 3d keyhole during deep penetration laser welding. Journal of Physics D Applied Physics, 39(21), 4703.
[40] Kawahito, Y., Matsumoto, N., Abe, Y., & Katayama, S. (2011). Relationship of laser absorption to keyhole behavior in high power fiber laser welding of stainless steel and aluminum alloy. Journal of Materials Processing Technology, 211(10), 1563-1568.
[41] Stenbacka, N. (2013). On arc efficiency in gas tungsten arc welding. Soldagem & Inspeção, 18(4), 380-390.
[42] Joseph, A., Harwig, D., Farson, D. F., & Richardson, R. (2003). Measurement and calculation of arc power and heat transfer efficiency in pulsed gas metal arc welding. Science and Technology of Welding & Joining, 8(6), 400-406.
[43] Metcalfe, J. C., & Quigley, M. B. C. (1975). Heat transfer in plasma-arc welding. Welding journal, 54(3), 99-103.
[44] DuPont, J. N., & Marder, A. R. (1995). Thermal efficiency of arc welding processes. Welding Journal-Including Welding Research Supplement, 74(12), 406s.
[45] Jiang, F., Li, C., & Chen, S. (2019). Experimental investigation on heat transfer of different phase in variable polarity plasma arc welding. Welding in the World, 63(4), 1153-1162.
[46] Mills, K. C., & Keene, B. J. (1990). Factors affecting variable weld penetration. International Materials Reviews, 35(1), 185-216.
[47] Nishi, T., Fujita, H., Haseba, S., and Ohara, M. 1982. Study on high speed submerged arc welding report 1. Japan Welding Society 30(8): 68–74.
[48] Ohara, M., Fujita, H., Haseba, S., and Nishi, T. 1983. Study on high speed submerged arc welding report 2. Japan Welding Society 31(2): 45–48.
[49] Nguyen, T. C., Weckman, D. C., & Johnson, D. A. (2007). Predicting onset of high speed gas metal arc weld bead defects using dimensional analysis techniques. Science and Technology of welding and Joining, 12(7), 634-648.
[50] Zong, R., Chen, J., Wu, C. S., & Padhy, G. K. (2017). Influence of molten metal flow on undercutting formation in GMAW. Science and Technology of Welding and Joining,

22(3), 198-207.
[51] Zong, R., Chen, J., Wu, C. S., & Chen, M. A. (2016). Undercutting formation mechanism in gas metal arc welding. Welding Journal, 95(5), 174-184.
[52] Powell, J., Ilar, T., Frostevarg, J., Torkamany, M. J., Na, S. J., Petring, D., Kaplan, A. F. (2015). Weld root instabilities in fiber laser welding. Journal of laser applications 27(S2): S29008.
[53] Zhang, M., Zhang, Z., Tang, K., Mao, C., Hu, Y., & Chen, G. (2018). Analysis of mechanisms of underfill in full penetration laser welding of thick stainless steel with a 10 kW fiber laser. Optics & Laser Technology, 98, 97-105.
[54] Liu, Z. M., Wu, C. S., & Chen, J. (2013). Sensing dynamic keyhole behaviors in controlled-pulse keyholing plasma arc welding. Welding Journal, 92(12), 381s-389s.
[55] Grinyuk, A. A., Korzhik, V. N., Shevchenko, V. E., Babich, A. A., & Peleshenko, S. I. (2016). Hybrid technologies of welding aluminium alloys based on consumable electrode arc and constricted arc. The Paton Welding Journal, 5(6), 98-103.
[56] Pilat, Z. , & Szulc, J. . (2014). Concept of the model robotized cell for plasma-gmaw hybrid welding. Applied Mechanics & Materials, 613, 43-52.
[57] Han, Y., Tong, J., Hong, H., & Sun, Z. (2019). The influence of hybrid arc coupling mechanism on GMAW arc in VPPA-GMAW hybrid welding of aluminum alloys. The International Journal of Advanced Manufacturing Technology, 101(1-4), 989-994.
[58] Sun, Z., Han, Y., Du, M., Tong, J., & Hong, H. (2019). An improved simulation of temperature field in VPPA–GMAW of Al–Cu–Mg alloy. Journal of Materials Processing Technology, 263, 366-373.
[59] Suder, W., Ganguly, S., Williams, S., & Yudodibroto, B. (2017). Root stability in hybrid laser welding. Journal of Laser Applications, 29(2), 022410.
[60] Churiaque, C., Chludzinski, M., Porrua-Lara, M., Dominguez-Abecia, A., Abad-Fraga, F., & Sánchez-Amaya, J. M. (2019). Laser hybrid butt welding of large thickness naval steel. Metals, 9(1), 100.
[61] Nomura, K., Shirai, K., Kishi, T., & Hirata, Y. (2015). Study on temperature measurement of two-electrode TIG arc plasma. Welding International, 29(7), 493-501.
[62] Qin, G., Meng, X., & Fu, B. (2015). High speed tandem gas tungsten arc welding process of thin stainless steel plate. Journal of Materials Processing Technology, 220, 58-64.

[63] Ueyama, T., Ohnawa, T., Tanaka, M., & Nakata, K. (2005). Effects of torch configuration and welding current on weld bead formation in high speed tandem pulsed gas metal arc welding of steel sheets. Science and Technology of Welding and Joining, 10(6), 750-759.
[64] Ueyama, T., Ohnawa, T., Tanaka, M., & Nakata, K. (2007). Occurrence of arc interaction in tandem pulsed gas metal arc welding. Science and Technology of Welding and Joining, 12(6), 523-529.
[65] Chen, J., Zong, R., Wu, C., Padhy, G. K., & Hu, Q. (2017). Influence of low current auxiliary TIG arc on high speed TIG-MIG hybrid welding. Journal of Materials Processing Technology, 243, 131-142.
[66] Zong, R., Chen, J., & Wu, C. (2019). A comparison of TIG-MIG hybrid welding with conventional MIG welding in the behaviors of arc, droplet and weld pool. Journal of Materials Processing Technology.
[67] Kanemaru, S., Sasaki, T., Sato, T., Era, T., & Tanaka, M. (2015). Study for the mechanism of TIG-MIG hybrid welding process. Welding in the World, 59(2), 261-268.
[68] Kanemaru, S., Sasaki, T., Sato, T., Mishima, H., Tashiro, S., & Tanaka, M. (2014). Study for TIG–MIG hybrid welding process. Welding in the World, 58(1), 11-18.
[69] Shinn, B. W., Farson, D. F., and Denney, P. E. (2005). Laser stabilization of arc cathode spots in titanium welding. Science and Technology of welding and Joining 10(4), 475-481.
[70] Zhou, J., & Tsai, H. L. (2008). Modeling of transport phenomena in hybrid laser-MIG keyhole welding. International Journal of Heat and Mass Transfer, 51(17-18), 4353-4366.
[71] Cho, J. H., & Na, S. J. (2009). Three-dimensional analysis of molten pool in GMA-laser hybrid welding. Welding Journal, 88(2), 35s-43s.
[72] Zhang, W., Hua, X. M., Liao, W., Li, F., and Wang, M. (2014). Behavior of the plasma characteristic and droplet transfer in CO2 laser–GMAW-P hybrid welding. The International Journal of Advanced Manufacturing Technology 72(5-8), 935-942.
[73] Liu, S. Y., Zhang, F. L., Dong, S. N., Zhang, H., and Liu, F. D. (2018). Characteristics analysis of droplet transfer in laser-MAG hybrid welding process. International Journal of Heat and Mass Transfer 121, 805-811.
[74] Mu, Z., Chen, X., Zheng, Z., Huang, A., & Pang, S. (2019). Laser cooling arc plasma

effect in laser-arc hybrid welding of 316L stainless steel. International Journal of Heat and Mass Transfer, 132, 861-870.
[75] Mu, Z., Chen, X., Hu, R., Lin, S., & Pang, S. (2019). Laser induced arc dynamics destabilization in laser-arc hybrid welding. Journal of Physics D: Applied Physics, 53(7), 075202.
[76] Wu, D., Huang, J., Kong, L., Hua, X., & Wang, M. (2020). Coupled mechanisms of arc, weld pool and weld microstructures in high speed tandem TIG welding. International Journal of Heat and Mass Transfer, 154, 119641.
[77] Wu, D., Hua, X., Ye, D., & Li, F. (2017). Understanding of humping formation and suppression mechanisms using the numerical simulation. International Journal of Heat and Mass Transfer, 104, 634-643.
[78] Gao, Z., & Ojo, O. A. (2012). Modeling analysis of hybrid laser-arc welding of single-crystal nickel-base superalloys. Acta materialia, 60(6-7), 3153-3167.
[79] Zhao, L., Sugino, T., Arakane, G., & Tsukamoto, S. (2009). Influence of welding parameters on distribution of wire feeding elements in CO2 laser GMA hybrid welding. Science and Technology of Welding and Joining, 14(5), 457-467.
[80] Zhang, Y. M., Zhang, S. B., & Liu, Y. C. (2001). A plasma cloud charge sensor for pulse keyhole process control. Measurement Science & Technology, 12(8), 1365.
[81] Wu, C. S., & Liu, Z. M. (2015). Dynamic variation of keyhole exit and its inclination in plasma arc welding. Welding in the World, 59(3), 365-371.
[82] Fan, H. G. , & Kovacevic, R. (1999). Keyhole formation and collapse in plasma arc welding. Journal of Physics D Applied Physics, 32(22), 2902.
[83] Zhang, T., Wu, C. S., & Feng, Y. (2011). Numerical analysis of heat transfer and fluid flow in keyhole plasma arc welding. Numerical Heat Transfer, 60(8), 685-698.
[84] Wu, C. S., Zheng, W., & Chen, M. A. (2014). Improving the prediction accuracy of keyhole establishment time in plasma arc welding. Numerical Heat Transfer Applications, 66(4), 420-432.
[85] Li, Y., Feng, Y. , Zhang, X. , & Wu, C. . (2014). Energy propagation in plasma arc welding with keyhole tracking. Energy, 64, 1044-1056.
[86] Li, T. Q., Wu, C. S., & Chen, J. (2016). Transient variation of arc heat flux and pressure distribution on keyhole wall in PAW. Welding in the World, 60(2), 363-371.
[87] Jian, X., & Wu, C. S. (2015). Numerical analysis of the coupled arc–weld pool–

keyhole behaviors in stationary plasma arc welding. International journal of heat and mass transfer, 84, 839-847.
[88] Jian, X., Wu, C., Zhang, G., & Chen, J. (2015). A unified 3D model for an interaction mechanism of the plasma arc, weld pool and keyhole in plasma arc welding. Journal of Physics D: Applied Physics, 48(46), 465504.
[89] Tashiro, S., Miyata, M., Tanaka, M., Shin, K., & Takahashi, K. (2010). Numerical analysis of keyhole welding of mild steel plate with the plasma arc. Transactions of JWRI, 39(1), 27-31.
[90] Wu, D., Hua, X., Ye, D., Ma, X., & Li, F. (2017). Understanding of the weld pool convection in twin-wire GMAW process. The International Journal of Advanced Manufacturing Technology, 88(1-4), 219-227.
[91] Wu, D., Hua, X., Ye, Y., Huang, L., Li, F., & Huang, Y. (2018). Experimental and numerical study of spatter formation and composition change in fiber laser welding of aluminum alloy. Journal of Physics D: Applied Physics, 51(18), 185604.
[92] Wu, D., Hua, X., Li, F., & Huang, L. (2017). Understanding of spatter formation in fiber laser welding of 5083 aluminum alloy. International Journal of Heat and Mass Transfer, 113, 730-740.
[93] Xu, B., Jiang, F., Chen, S., Tanaka, M., Tashiro, S., & Van Anh, N. (2018). Numerical analysis of plasma arc physical characteristics under additional constraint of keyhole. Chinese Physics B, 27(3), 034701.
[94] Cho, D. W., Na, S. J., Cho, M. H., & Lee, J. S. (2013). Simulations of weld pool dynamics in V-groove GTA and GMA welding. Welding in the World, 57(2), 223-233.
[95] Cheon, J., Kiran, D. V., & Na, S. J. (2016). CFD based visualization of the finger shaped evolution in the gas metal arc welding process. International Journal of Heat and Mass Transfer, 97, 1-14.
[96] Phares, D. J., Smedley, G. T., & Flagan, R. C. (2000). The wall shear stress produced by the normal impingement of a jet on a flat surface. Journal of Fluid Mechanics, 418, 351-375.
[97] Cho, W. I., Na, S. J., Thomy, C., & Vollertsen, F. (2012). Numerical simulation of molten pool dynamics in high power disk laser welding. Journal of Materials Processing Technology, 212(1), 262-275.
[98] Zhang, Y. X., Han, S. W., Cheon, J., Na, S. J., & Gao, X. D. (2017). Effect of joint

gap on bead formation in laser butt welding of stainless steel. Journal of Materials Processing Technology, 249, 274-284.
[99] Cho, D. W., Cho, W. I., & Na, S. J. (2014). Modeling and simulation of arc: laser and hybrid welding process. Journal of Manufacturing Processes, 16(1), 26-55.
[100] Wang, X., Fan, D., Huang, J., & Huang, Y. (2015). Numerical simulation of arc plasma and weld pool in double electrodes tungsten inert gas welding. International Journal of Heat and Mass Transfer, 85, 924-934.
[101] Zhang X, Wu C. (2015). Thermal process model of plasma arc welding with considering the backside keyhole deviation[J]. Journal of Mechanical Engineering, 51(14), 66-71.
[102] Li, T. Q., & Wu, C. S. (2015). Numerical simulation of plasma arc welding with keyhole-dependent heat source and arc pressure distribution. The International Journal of Advanced Manufacturing Technology, 78(1-4), 593-602.
[103] Jian X, Wu C. (2016). Influence of Fe vapor on weld pool behavior of plasma arc welding [J]. Acta Metallurgica Sinica, 52(11), 1467-1476.
[104] Wu, D., Hua, X., Huang, L., Li, F., & Cai, Y. (2018). Elucidation of keyhole induced bubble formation mechanism in fiber laser welding of low carbon steel. International Journal of Heat and Mass Transfer, 127, 1077-1086.
[105] Tanaka, M., Terasaki, H., Ushio, M., & Lowke, J. J. (2003). Numerical study of a free-burning argon arc with anode melting. Plasma Chemistry and Plasma Processing, 23(3), 585-606.
[106] Tashiro, S., Tanaka, M., Ueyama, T., & Era, T. (2012). Numerical simulation of keyhole welding of aluminium thick plate with plasma arc. Welding International, 26(6), 441-447.
[107] Lu, F., Wang, H. P., Murphy, A. B., & Carlson, B. E. (2014). Analysis of energy flow in gas metal arc welding processes through self-consistent three-dimensional process simulation. International Journal of Heat and Mass Transfer, 68, 215-223.
[108] Scott, D. A., Kovitya, P., & Haddad, G. N. (1989). Temperatures in the plume of a dc plasma torch. Journal of Applied Physics, 66(11), 5232-5239.
[109] Hong, Y. C., Shin, D. H., Lee, S. J., Kim, Y. J., Lee, B. J., & Uhm, H. S. (2012). Syngas production from gasification of brown coal in a microwave torch plasma. Energy, 47(1), 36-40.

[110] Schnick, M., FÜssel, U., & Spille-Kohoff, A. (2010). Numerical investigations of the influence of design parameters, gas composition and electric current in plasma arc welding (PAW). Welding in the World, 54(3-4), R87-R96.
[111] Li, Y., Feng, Y., Li, Y., Zhang, X., & Wu, C. (2016). Plasma arc and weld pool coupled modeling of transport phenomena in keyhole welding. International Journal of Heat and Mass Transfer, 92, 628-638.
[112] Li, Y., Wang, L., & Wu, C. (2018). Simulation of keyhole plasma arc welding with electro-magneto-thermo-hydrodynamic interactions. The International Journal of Advanced Manufacturing Technology, 1-11.
[113] Tashiro, S., Murphy, A. B., & Tanaka, M. (2018). Numerical simulation of fume formation process in GMA welding. Welding in the World, 62(6), 1331-1339.
[114] Goodarzi, M., Choo, R., & Toguri, J. M. (1997). The effect of the cathode tip angle on the GTAW arc and weld pool: I. Mathematical model of the arc. Journal of Physics D: Applied Physics, 30(19), 2744.
[115] Tanaka, M., Yamamoto, K., Tashiro, S., Nakata, K., Yamamoto, E., Yamazaki, K., Lowke, J. J. (2010). Time-dependent calculations of molten pool formation and thermal plasma with metal vapour in gas tungsten arc welding. Journal of Physics D: Applied Physics, 43(43), 434009.
[116] Tanaka, M., Ushio, M., & Lowke, J. J. (2004). Numerical study of gas tungsten arc plasma with anode melting. Vacuum, 73(3), 381-389.
[117] Cheon, J., & Na, S. J. (2016). Influence of simulation methods of temperature distribution on thermal and metallurgical characteristics in gma welding. Materials & Design, 108, 183-194.
[118] Behzad, F., Wayne, S. F., Gladius, L., & Ebrahim, A. (2018). A review on melt-pool characteristics in laser welding of metals. Advances in Materials Science and Engineering, 2018, 1-18.
[119] Liu, Z. M., Wu, C. S., Cui, S. L., & Luo, Z. (2017). Correlation of keyhole exit deviation distance and weld pool thermo-state in plasma arc welding process. International Journal of Heat & Mass Transfer, 104, 310-317.
[120] Evans, D. M., Huang, D., McClure, J. C., & Nunes, A. C. (1998). Arc efficiency of plasma arc welding. Welding journal, 77(2), 53-58.
[121] Wu, C. S., Chen, M. A., and Lu, Y. F. (2005). Effect of current waveforms on metal

transfer in pulsed gas metal arc welding. Measurement Science and Technology, 16(12), 2459.
[122] Ueguri, S., Hara, K., & Komura, H. (1985). Study of metal transfer in pulsed GMA welding. Welding journal 64(8), 242-250.
[123] Ghosh, P. K., Dorn, L., Kulkarni, S., and Hofmann, F. (2009). Arc characteristics and behaviour of metal transfer in pulsed current GMA welding of stainless steel. Journal of Materials Processing Technology 209(3), 1262-1274.
[124] Cho, M. H., Lim, Y. C., and Farson, D. F. (2006). Simulation of weld pool dynamics in the stationary pulsed gas metal arc welding process and final weld shape. Welding Journal, 85(12), 271s-283s.
[125] Liu, S. Y., Liu, F. D., Zhang, H., and Shi, Y. (2012). Analysis of droplet transfer mode and forming process of weld bead in CO2 laser–MAG hybrid welding process. Optics & Laser Technology, 44(4), 1019-1025.
[126] Lancaster, J. F. (1987). The physics of fusion welding. Part 1: The electric arc in welding. IEE Proceedings B (Electric Power Applications), 134(5), 233-254.
[127] Wu, D. S., Tashiro, S., Hua, X. M., and Tanaka, M. (2019). A novel electrode-arc-weld pool model for studying the keyhole formation in the keyhole plasma arc welding process. Journal of Physics D: Applied Physics. 52(16), 165203.
[128] Jiang, Z., Hua, X. M., Huang, L. J., Wu, D. S., and Li, F. (2017). Effect of multiple thermal cycles on metallurgical and mechanical properties during multi-pass gas metal arc welding of Al 5083 alloy. The International Journal of Advanced Manufacturing Technology, 93(9-12), 3799-3811.
[129] Cho, D. W., Na, S. J., Cho, M. H., & Lee, J. S. (2013). Simulations of weld pool dynamics in V-groove GTA and GMA welding. Welding in the World, 57(2), 223-233.
[130] Wu, L., Cheon, J., Kiran, D. V., & Na, S. J. (2016). CFD simulations of GMA welding of horizontal fillet joints based on coordinate rotation of arc models. Journal of Materials Processing Technology, 231, 221-238.
[131] Haelsig, A., & Mayr, P. (2013). Energy balance study of gas-shielded arc welding processes. Welding in the World, 57(5), 727-734.
[132] Cho, D. W., Kiran, D. V. , Song, W. H. , & Na, S. J. . (2014). Molten pool behavior in the tandem submerged arc welding process. Journal of Materials Processing Technology, 214(11), 2233-2247.

[133] Kiran, D. V., Cho, D. W. , Song, W. H. , & Na, S. J. . (2015). Arc interaction and molten pool behavior in the three wire submerged arc welding process. International Journal of Heat and Mass Transfer, 87, 327-340.
[134] Cho, D. W., Na, S. J., Cho, M. H., & Lee, J. S. (2013). A study on V-groove GMAW for various welding positions. Journal of Materials Processing Technology, 213(9), 1640-1652.
[135] Bai, X., Colegrove, P., Ding, J., Zhou, X., Diao, C., Bridgeman, P., ... & Williams, S. (2018). Numerical analysis of heat transfer and fluid flow in multilayer deposition of PAW-based wire and arc additive manufacturing. International Journal of Heat and Mass Transfer, 124, 504-516.
[136] Cho, D. W., Song, W. H., Cho, M. H., & Na, S. J. (2013). Analysis of submerged arc welding process by three-dimensional computational fluid dynamics simulations. Journal of Materials Processing Technology, 213(12), 2278-2291.
[137] Nguyen, T. C., Weckman, D. C., Johnson, D. A., & Kerr, H. W. (2005). The humping phenomenon during high speed gas metal arc welding. Science and Technology of Welding and Joining, 10(4), 447-459.

List of publications

1. **Wu, D.**, Van N, A., Tashiro, S., Hua, X., & Tanaka, M. (2019). Elucidation of the weld pool convection and keyhole formation mechanism in the keyhole plasma arc welding. **International Journal of Heat and Mass Transfer**, 131, 920-931. **(Chapter 2)**

2. **Wu, D.**, Tashiro, S., Hua, X., & Tanaka, M. (2019). A novel electrode-arc-weld pool model for studying the keyhole formation in the keyhole plasma arc welding process. **Journal of Physics D: Applied Physics**, 52(16), 165203. **(Chapter 3)**

3. Nguyen, A. V., **Wu, D.***, Tashiro, S., & Tanaka, M. (2019). Undercut formation mechanism in the keyhole plasma arc welding. **Welding Journal**, 98, 204s-212s **(Corresponding author, Chapter 1)**

4. **Wu, D.**, Tashiro, S., Hua, X., & Tanaka, M. (2019). Analysis of the energy propagation in the keyhole plasma arc welding using a novel fully coupled plasma arc-keyhole-weld pool model. **International Journal of Heat and Mass Transfer**, 141, 604-614. **(Chapter 4)**

5. **Wu, D.**, Tashiro, S., Wu, Z., Nomura, K., & Tanaka, M. (2019). Interactive phenomena in hybrid kpaw-pgmaw. **Welding Journal**, 99, 146s-155s. **(Chapter 5)**

6. **Wu, D.**, Tashiro, S., Wu, Z., Nomura, K., Hua, X., & Tanaka, M. (2020). Analysis of heat transfer and material flow in hybrid KPAW-GMAW process based on the novel three dimensional CFD simulation. **International Journal of Heat and Mass Transfer**, 147, 118921. **(Chapter 6)**

7. **Wu, D.**, Tashiro, S., Hua, X., & Tanaka, M. Coupled mechanisms of the keyhole, energy transfer and compositional change associated with the variable polarity plasma arc process, **Journal of Physics D: Applied Physics**. **(Accepted)**

List of awards

1. The Award of Association of Chinese Alumni in Japan, Association of Chinese Alumni in Japan, 2019.
2. William Spraragen Memorial Award, American Welding Society (AWS), 2020.
3. Excellent award for the "Chunhui Cup" Innovation and Entrepreneurship Competition, the Ministry of Education and the Ministry of Science and Technology, 2020.

賞　状

中国留日同学会賞

吴　東昇　殿

あなたの下記論文は「第17回留日中国人優秀研究成果表彰会」において優秀な成績を収められましたのでこれを賞します

記

'Elucidation of the weld pool convection and key-hole formation mechanism in the keyhole plasma arc welding', *International Journal of Heat and Mass Transfer*, 131, 920-931, 2019

令和元年11月16日

中国留日同学会 会長　江

The
William Spraragen
Memorial Certificate Award

Presented to

Dongsheng Wu

By the American Welding Society
For the best research paper printed in the Supplement of the Welding Journal during the twelve-month period Ending with the November 2019 issue.

"Undercut Formation Mechanism in Keyhole Plasma Arc Welding"

Given this 19th day of November 2020

AWS PRESIDENT

AWS EXECUTIVE DIRECTOR & CEO

项目编号：202000200

获奖证书

吴东升 获得第十五届“春晖杯”中国留学人员创新创业大赛 先进制造与自动化组 优胜奖。获奖项目为：《钛管高品质双枪 TIG 焊智能装备与虚拟制造系统》。

团队成员：郑碧美、石烨婧、张旺、张跃龙、华学明

特颁此证。

“春晖杯”中国留学人员创新创业大赛组委会
教育部国际合作与交流司（代章）
2020年12月

Acknowledgements

How time flies!

At 2017, Prof. Wu and Prof. Hua from Shanghai Jiao Tong University recommended me to Prof. Tanaka, then I left my job and came to Japan to start my doctoral study. During the doctoral study, I did research based on my interests, and learned arc simulation under the guidance of Assist. Prof. Shinichi Tashiro. I also traveled to many Japanese famous sights with lab members and my girl friend.

I would like to express my sincere appreciation to Prof. Tanaka for accepting me as his doctoral student, and providing a nice research environment for me. Sometimes, Prof. Tanaka invited us to drink and eat delicious food in his professor room. I will remember all these good memories in all my life. I would like to express the deepest thankfulness to Assist. Prof. Shinichi Tashiro. He taught me how to do arc simulation. We discussed how to write and revise papers together. Without his kind helps, I can't get many good achievements.

I would also like to thank Prof. Tomokazu Sano (Graduate School of Engineering) and Prof. Hiroshige Inoue (JWRI) for being my co-supervisor and reviewing my doctoral thesis.

I would like to thank Prof. Wu and Prof. Hua from Shanghai Jiao Tong University for recommending me to Prof. Tanaka. Prof. Hua also gave many good opinions to my doctoral study, and provided his help to my life in Japan. He also allowed me to use my previous research achievements, and attend many commercial competitions.

I would like to give the thanks to A/Prof. Masaya Shigeta and lab members. From their studies, I changed some of my views. Previously, I thought I can carry out researches only by commercial software. Now I decide to learn open access software in my free time.

I would also like to thank the China Scholarship Council for supporting my life and study in Japan.

Finally, I would especially like to thank my girl friend, Bimei Zheng. She accompanies me in Japan and asks me to concentrate on my research. With her accompany, my life in Japan has become better

Dongsheng WU

January 2021